Final Scientific/Technical Report
Computational Design and Prototype Evaluation of Aluminide-Strengthened Ferritic Superalloys for Power-Generating Turbine Applications up to 1,033 K

Submitted to: The Department of Energy, Office of Fossil Energy
Grant Number: DE-FG26-06NT42732
Performance Period: 04/01/2006-04/30/2010
Report Issued Date: 06/25/2010

Names and Addresses of Submitting Organizations:

1. **Prof. Peter K. Liaw (Principal Investigator)**
   The University of Tennessee, 427-B Dougherty Engineering Building, Department of Materials Science and Engineering, The University of Tennessee, Knoxville, TN 37996-2200.
   Phone: (865) 974-6356, Fax: (865) 974-4115, E-mail: pliaw@utk.edu
2. **Prof. Gautam Ghosh (Co-Principal Investigator)**
   Northwestern University, 2220 Campus Drive, Department of Materials Science and Engineering, Northwestern University, Evanston, IL 60208-3108.
   Phone: (847) 467-2595, Fax: (847) 491-7820, E-mail: g-ghosh@northwestern.edu
3. **Prof. Mark D. Asta (Co-Principal Investigator)**
   Department of Materials Science and Engineering, University of California, Berkeley, CA 94720.
   Phone: (510) 643-9631, Fax: (510) 643-5792, E-mail: mdasta@berkeley.edu
4. **Prof. Morris E. Fine (Co-Principal Investigator)**
   Northwestern University, 2220 Campus Drive, Department of Materials Science and Engineering, Northwestern University, Evanston, IL 60208-3108.
   Phone: (847) 491-3537, Fax: (847) 491-7820, E-mail: m-fine412@northwestern.edu
5. **Prof. Chain T. Liu (Co-Principal Investigator)**
   Oak Ridge National Laboratory, Oak Ridge, TN 37831.
   Department of Materials Engineering, Auburn University, Auburn, AL 36849.
   Department of Mechanical Engineering, Hong Kong Polytechnic University, Hong Kong, China.
   Phone: 86-(852) 2766-6644, Fax: (852) 2364-7183, E-mail: liuct@ornl.gov

ABSTRACT

The objective of the proposed research is to utilize modern computational tools, integrated with focused experiments, to design innovative ferritic NiAl-strengthened superalloys for fossil-energy applications at temperatures up to 1,033 K. Specifically, the computational alloy design aims toward (1) a steady-state creep rate of approximately 3 x 10^{-11} s^{-1} at a temperature of 1,033 K and a stress level of 35 MPa, (2) a ductility of 10% at room temperature, and (3) good oxidation and corrosion resistance at 1,033 K.

The research yielded many outstanding research results, including (1) impurity-diffusion coefficients in α Fe have been calculated by first principles for a variety of solute species; (2) the precipitates were characterized by the transmission-electron microscopy (TEM) and analytical-electron microscopy (AEM), and the elemental partitioning has been determined; (3) a bending ductility of more than 5% has been achieved in the unrolled materials; and (4) optimal compositions with minimal secondary creep rates at 973 K have been determined.

Impurity diffusivities in α Fe have been calculated within the formalisms of a harmonic transition-state theory and Le Claire nine-frequency model for vacancy-mediated diffusion. Calculated diffusion coefficients for Mo and W impurities are comparable to or larger than that for Fe self-diffusion. Calculated activation energies for Ta and Hf impurities suggest that these solutes should display impurity-diffusion coefficients larger than that for self-diffusion in the body-centered cubic Fe. Preliminary mechanical-property studies identified the alloy Fe-6.5Al-10Ni-10Cr-3.4Mo-0.25Zr-0.005B (FBB-8) in weight percent (wt.%) for detailed investigations. This alloy shows precipitation of NiAl particles with an average diameter of 130 nm.

In conjunction with the computational alloy design, selected experiments are performed to investigate the effect of the Al content on the ductility and creep of prototype Fe-Ni-Cr-Al-Mo alloys. Three-point-bending experiments show that alloys containing more than 5 wt.% Al exhibit poor ductility (< 2%) at room temperature, and their fracture mode is predominantly of a cleavage type. Two major factors governing the poor ductility are (1) the volume fraction of NiAl-type precipitates, and (2) the Al content in the α-Fe matrix. A bend ductility of more than 5% can be achieved by lowering the Al concentration to 3 wt.% in the alloy.

The alloy containing about 6.5 wt.% Al is found to have an optimal combination of hardness, ductility, and minimal creep rate at 973 K. A high volume fraction of precipitates is responsible for the good creep resistance by effectively resisting the dislocation motion through Orowan-bowing and dislocation-climb mechanisms. The effects of stress on the creep rate have been studied. With the threshold-stress compensation, the stress exponent is determined to be 4, indicating power-law dislocation creep. The threshold stress is in the range of 40 ~ 53 MPa. The addition of W can significantly reduce the secondary creep rates. Compared to other candidates for steam-turbine applications, FBB-8 does not show superior creep resistance at high stresses (> 100 MPa), but exhibit superior creep resistance at low stresses (< 60 MPa).

TABLE OF CONTENTS

A. EXECUTIVE SUMMARY

Currently, ferritic steels are used at temperatures below 894 K for fossil-energy-conversion systems due to their limited creep resistance and poor steam-corrosion resistance at higher temperatures. In order to improve the thermal efficiency of steam turbines, the Ultra-Supercritical Steam Turbines Program sponsored by the Department of Energy (DOE) Fossil Energy Program requires an increase of the steam temperature from 866 to 950 K by the year 2010 and to 1,033 K by 2020.

The objective of the proposed research is to utilize modern computational tools, integrated with focused experiments, to design innovative ferritic NiAl-strengthened superalloys for fossil-energy applications at temperatures up to 1,033 K. Specifically, the computational alloy design aims toward (1) a steady-state creep rate of approximately 3×10^{-11} s^{-1} at a temperature of 1,033 K and a stress level of 35 MPa, (2) a ductility of 10% at room temperature, and (3) good oxidation and corrosion resistance at 1,033 K.

During the four-year joint-university project, efforts have been devoted to achieving these objectives by a variety of computational and experimental methods. The resulting outstanding research outcomes are listed as follows: (1) impurity-diffusion coefficients in α Fe have been calculated by first principles for a variety of solute species; (2) a bending ductility of more than 5% has been achieved in the unrolled materials; (3) optimal compositions [Fe-6.5Al-10Ni-10Cr-3.4Mo-0.25Zr-0.005B in weight percent (wt.%) and similar compositions containing additional W] with minimal secondary creep rates at 973 K (~ 10^{-9} s^{-1} for compressive creep at 140 MPa and 10^{-10} ~ 10^{-8} s^{-1} for tensile creep at 60 MPa) have been determined; and (4) the precipitates have been characterized by the transmission-electron microscopy (TEM) and analytical-electron microscopy (AEM), and the elemental partitioning has been determined, which facilitates the understanding of the relationships between the microstructure and mechanical behavior.

The impacts that have resulted from this project include: (1) the further development of a new high-temperature, creep-resistant class of ferritic “superalloy” steels for applications in advanced steam-turbine systems; (2) the improvement of room-temperature ductility and high-temperature creep resistance by alloying optimizations; (3) the demonstration of a computational approach using first-principles calculations for accurately predicting the impurity diffusivities in Fe; (4) the augmentation of a diffusion-kinetic database by first-principles calculations; (5) the training of two Ph.D. students (Zhenke Teng and Shenyan Huang), one research associate (Dr. Gongyao Wang), and one undergraduate student (Daniel Worthington) in the integration of state-of-the-art computational and experimental methods that will form the framework for a modern approach to alloy design; (6) research work published in three high-level journal papers, prepared in a number of papers for future publications, and presented at several academic conferences; and (7) recognized student and faculty awards related to the research work.

B. REPORT DETAILS

Self and impurity diffusivities in the body-centered-cubic (bcc) iron have been calculated within the formalisms of a harmonic transition-state theory, and the Le Claire nine-frequency model for vacancy-mediated diffusion. The approach combines first-principles calculations of the vacancy formation, migration, and solute-binding enthalpies and entropies in the ferromagnetic phase, with an empirical relationship for the effect of magnetic disorder on diffusion-activation energies. Calculated Fe self-diffusion and Mo and W impurity-diffusion coefficients are shown to agree within a factor of five with the most recent experimental measurements in both the ferromagnetic and paramagnetic phases. Calculated diffusion coefficients for Mo and W impurities are comparable to or larger than that for Fe self-diffusion at all temperatures below the α-γ phase transition. Calculated activation energies for Ta and Hf impurities suggest that these solutes should also display impurity-diffusion coefficients larger than that for self-diffusion in the bcc Fe.

Two major problems for the development of ferritic steels strengthened by NiAl-type (B2) precipitates are their poor ductility at room temperature and inferior creep and coarsening resistance at high temperatures. In conjunction with the computational alloy design, selected experiments are performed to investigate the effect of elements (e.g., Al, W, and Zr) on the ductility and creep property of prototype Fe-Ni-Cr-Al alloys. The microstructures and compositions of the matrix (a α-Fe type) and precipitate phases were characterized by the transmission-electron microscopy (TEM) and analytical-electron microscopy (AEM). The phase transformation was studied by the differential-scanning calorimetry (DSC). Three-point-bending experiments show that alloys containing more than 5 weight percent (wt.%) Al exhibit poor ductility (< 2%) at room temperature, and their fracture mode is predominantly

of a cleavage type. Two major factors governing the poor ductility are (1) the volume fraction of NiAl-type precipitates, and (2) the Al content in the α-Fe matrix. A bend ductility of more than 5% can be achieved by lowering the Al concentration to 3 wt.% in the alloy. The alloy containing about 6.5 wt.% Al is found to have an optimal combination of both creep resistance and ductility. Orowan bowing and dislocation climb were identified to be dislocation-particle interaction mechanisms. Steady-state compressive creep rates declined in the alloys with 3 ~ 6.5 wt.% Al and increased with 6.5 ~ 10 wt.% Al. Tensile-creep experiments by stepwise loading have been performed, and the stress exponent and threshold stress have been determined. The addition of W can significantly reduces the secondary creep rates. Compared to other candidates for steam-turbine applications, the ferritic alloys exhibit superior creep resistance at low stresses (< 60 MPa) and at 973 K.

B.1 First-Principles Calculations of Impurity Diffusivities in Bcc Fe

B.1.1 Introduction

In recent years, first-principles computational methods, based on an electronic density-functional theory (DFT), have found widespread applications in the modeling of alloy thermodynamic properties and phase stability. First-principles methods have been applied extensively in calculations of alloy-formation energies, entropies, and phase boundaries, for a wide variety of binary and some ternary systems [1-6]. The results of such calculations are also increasingly incorporated within the CALculation of Alloy PHAse Diagrams (CALPHAD) formalism [e.g., 6-7] for modeling complex multicomponent phase equilibria [e.g., 1,3,6,9,10]. In the context of alloy design, an equally important area of applications for DFT methods is the calculation of alloy diffusivities. In comparison to the extensive amount of work devoted to thermodynamic properties, far fewer diffusion calculations for alloys have been undertaken to

date [11-24]. While the number of applications is currently limited, impressive agreement with experimental measurements has been demonstrated in recent calculations for a variety of solute species in Al- and Ni- based alloys [13,16,20]. For expanded applications of DFT techniques in modeling alloy-diffusion kinetics, further diffusivity calculations would be useful to assess the accuracy of these methods for other technologically-important systems.

In the present work, DFT methods are applied in calculations of impurity-diffusion constants for substitutional transition-metal (TM) solute species in the bcc ferritic Fe. This work is motivated by an effort aimed at the development of high-temperature, creep-resistant Fe-Ni-Al-Cr-based ferritic alloys, containing fine dispersions of coherent, nanoscale (B2-NiAl based) precipitates in a bcc Fe matrix [26-29]. To optimize the properties of ferritic alloys for such high-temperature applications, it is desirable to identify slow-diffusing solute additions that can act to reduce precipitate-coarsening kinetics, and help optimize creep strengths [25,29].

Figure 1 presents a compilation of the available experimental data for impurity diffusivities [30-66] in the bcc Fe. The data are exhibited at a representative temperature of 1,050 K, and are plotted as relative values, i.e., as ratios of the solute-impurity diffusivities to the self-diffusivity of Fe at the same temperature. The results are represented as a function of the electron to atom ratio for available TM species, as well as a few non-TM elements. In cases where more than one data point is plotted for a given species, different measured values are reported in the literature [30-66]. In the context of the present work, three points related to Fig. 1 are noteworthy. First, there is significant discrepancy between the values derived from independent measurements for several of the elements – an example is Mo where the reported values vary by more than an order of magnitude. Second, published results for most 5d TM elements are absent in the current database. Third, there are no clearly apparent slow-diffusing

species, with diffusivities that are several orders of magnitude lower than that of pure Fe. The goal of the present work is to pursue the application of DFT methods as a framework for augmenting the database of impurity-diffusion constants in the bcc Fe, and to help guide the search for candidate slow-diffusing solutes in this material.

To this end, we present here a framework for calculating impurity-diffusion coefficients in the bcc Fe, and assess its accuracy through calculations of self-diffusion, and impurity-diffusion coefficients for W and Mo solutes. These two TM solute species are chosen due to the availability of recent measurements of impurity diffusivities over a wide temperature range [52,53]. The computational approach employed here is based on the nine-frequency formalism of Le Claire [67], which accounts for all of the distinct jump frequencies, when the solute and vacancy display appreciable interactions at both first and second neighbor distances in the bcc lattice. Within this formalism, the computational approach combines first-principles calculations of saddle-point, vacancy-formation and solute-vacancy binding energies and entropies in the ordered ferromagnetic state, with a semi-empirical model for the effects of magnetic disorder on the activation energy [68,69,70] at temperatures up to and above the Curie temperature. Calculations of the relevant hopping frequencies are performed within the framework of a harmonic transition-state theory [71,72], following an approach similar to that employed in recent calculations of impurity diffusivities in the face-centered-cubic (fcc) Al [20]. The overall computational approach shares features in common with the methods employed in recent first-principles calculations of Cu, P, Ni, and Cr diffusion in the bcc Fe [14,22-24] – the current work extends these previous studies by including direct calculations of the vibrational frequencies required to compute diffusivity prefactors.

B.1.2 Computational Methodology

Measured self- and impurity-diffusion constants in the bcc Fe are often observed to display appreciably non-Arrhenius temperature dependencies in the ferromagnetic phase (e.g., [69] and references therein). This effect is generally attributed to the dependence of the diffusion-activation energy (Q) on the bulk magnetization (M), which is often modeled to have the following form [69]:

$$Q^F(T) = Q^P[1 + \alpha s(T)^2] \quad (1)$$

In Eq. (1), Q^P denotes the activation energy in the paramagnetic state (i.e., where $M = 0$), and $s = M(T)/M(T = 0\ K)$ is the reduced magnetization at a temperature, T, which varies continuously in the ferromagnetic phase between one at zero temperature, and zero at 1,043 K, the Curie temperature [$s(T) = 0$ for all T in the paramagnetic phase]. α is a species-dependent parameter that quantifies the dependence of Q on magnetization. Equation (1) is derived from a mean-field analysis of the effects of magnetic disorder on diffusion-acitivation energies in ferromagnetic materials [68,70]. In this analysis, the leading order correction to Q is quadratic in $s(T)$. In terms of the parameter, α, the activation energy in the fully-ordered ferromagnetic state, $Q_0^F = Q^F(T = 0\ K)$, is related to that in the paramagnetic phase through the relation, $Q_0^F = Q^P(1 + \alpha)$.

In the present work, Eq. (1) is used to extend the zero-temperature DFT calculations to account for the effects of magnetic disorder at a finite T. Specifically, all of the first-principles calculations are performed in the fully-ordered ferromagnetic state, where both the diffusion prefactor (D_0) and activation energy (Q_0^F) are computed within the framework of a harmonic-transition-state theory. To account for the effects of magnetic disorder, Eq. (1) is used along with the published temperature-dependent values of $s(T)$ [73,74], and the measured values

of α for Fe self-diffusion (α = 0.156), W-impurity diffusion (α = 0.086), and Mo-impurity diffusion (α = 0.074) reported in Refs. [52,69]. As discussed in Refs. [24,69], for the impurity species where the parameter, α, has not been measured, its value can be estimated from first-principles calculations employing a semi-empirical linear relationship between α and the induced changes in the local moments of the first and second-neighbor Fe atoms surrounding a solute impurity.

B.1.2.1 Self Diffusion

In all of the diffusivity calculations discussed in this paper, we assume that diffusion is governed by a mono-vacancy mechanism mediated by nearest-neighbor vacancy hops. For the self-diffusion governed by such a mono-vacancy mechanism on a bcc lattice, the diffusion coefficient can be expressed as (e.g., [75]):

$$D = a^2 f_0 C_v \Gamma \tag{2}$$

where a is the bcc lattice parameter, $f_0 = 0.727$ is the correlation factor for the bcc lattice, C_v denotes the equilibrium vacancy concentration, and Γ is the vacancy-hopping frequency.

The equilibrium vacancy concentration can be expressed as:

$$C_v = \exp\left(\frac{\Delta S_v^f}{k_B}\right) \times \exp\left(-\frac{\Delta H_v^f}{k_B T}\right) \tag{3}$$

where ΔH_v^f and ΔS_v^f denote the vacancy-formation enthalpy and entropy, respectively, and k_B is Boltzmann's constant. Considering only vibrational (phonon) contributions to the free energy, and employing the high-temperature limit of the harmonic approximation for the lattice dynamics, ΔH_v^f and ΔS_v^f are constants, independent of temperature. In this limit, the vacancy-formation enthalpy at zero pressure can be calculated from first principles as $\Delta H_v^f = E(N-1) - [(N-1)/N]E(N)$, where *E(N-1)* denotes the energy of a supercell containing

N lattice sites with *N-1* atoms and one vacancy, while *E(N)* represents the energy for the same supercell containing *N* atoms. Similarly, ΔS_v^f can be calculated as the difference in the high-temperature values of the vibrational entropy for a defected and non-defected supercell, yielding:

$$\Delta S_v^f = k_B\left[\sum_{i=1}^{3[N-1]} \ln\left(k_B T / h\nu_i^{vac}\right) - \frac{N-1}{N}\sum_{i=1}^{3N} \ln\left(k_B T / h\nu_i^{Bulk}\right)\right] \quad (4)$$

where ν_i^{vac} denotes the vibrational frequencies in a supercell containing *N-1* atoms and a vacancy, while ν_i^{bulk} corresponds to the frequencies in a non-defected supercell containing *N* atoms. In this work, the vibrational frequencies entering Eq. (4) are computed from first principles employing a frozen-phonon methodology described below.

On the basis of the Vineyard's harmonic transition-state theory [71,72], the hopping frequency, Γ, can be written as:

$$\Gamma = \left[\prod_{i=1}^{3N-3} \nu_i^{vac} \Big/ \prod_{i=1}^{3N-4} \nu_i^{sad}\right] \times \exp\left(-\Delta H_v^{mig} / k_B T\right) \quad (5)$$

where ΔH_v^{mig} is the migration enthalpy, computed as the difference in energies between an *N-1* atom supercell with the hopping atom in its saddle-point configuration, and in its normal (stable) configuration. Similarly, ν_i^{vac} and ν_i^{sad} are the phonon frequencies in the normal and saddle-point configurations, and the product in the denominator excludes the unstable mode for the transition state.

By combining Eqs. (1) - (5), the Fe self-diffusion coefficient is written as follows:

$$D = D_0 \exp\left\{-Q_0^F\left[\left(1+\alpha s(T)^2\right)/(1+\alpha)\right]/k_B T\right\} \quad (6)$$

where the activation energy, Q_0^F, is given as the sum of the vacancy formation and migration energies in the fully-ordered ferromagnetic state:

$$Q_0^F = \Delta H_v^f + \Delta H_v^{mig} \tag{7}$$

The pre-factor, D_0, is expressed as:

$$D_0 = a^2 f_{bcc} \exp\left(\Delta S_v^f / k_B\right) \times \left[\prod_{i=1}^{3N-3} \nu_i^{vac} \Big/ \prod_{i=1}^{3N-4} \nu_i^{sad} \right] \tag{8}$$

where as in Eq. (7), the vacancy-formation entropy and vibrational frequencies are evaluated in the fully-ordered ferromagnetic state.

B.1.2.2 Impurity Diffusion

For the impurity diffusion governed by a mono-vacancy mechanism on a bcc lattice, the diffusion coefficient can be expressed as (e.g., [67,75]):

$$D = a^2 f_2 C_v \exp\left(-\Delta G_b / k_B T\right) \Gamma_2 \tag{9}$$

In Eq. (9), the correlation factor, f_2, depends on the relative jump rates for a vacancy to different sites neighboring the solute atom [see Eqs. (11) - (12) below]. G_b denotes the binding free energy between a solute atom and a nearest-neighbor vacancy, with the sign convention that negative (positive) values correspond to attractive (repulsive) interactions. In this work, Γ_2, which denotes the frequency for a solute impurity to exchange with a nearest-neighbor vacancy, is calculated within the framework of a harmonic transition-state theory. This hopping frequency can thus be expressed analogously to Eq. (5) in terms of the migration energy for the vacancy-solute exchange, and the vibrational frequencies in the binding and saddle-point configurations.

The solute-vacancy binding free energy can be written as $\Delta G_b = \Delta H_b - T\Delta S_b$ in terms of a binding enthalpy (ΔH_b) and entropy (ΔS_b). Considering only phonon contributions to the binding entropy, and employing the high-temperature limit of the harmonic approximation for the lattice dynamics, ΔH_b and ΔS_b are again temperature-independent constants. The binding enthalpy is thus computed from first-principles calculations employing N-site supercells as ΔH_b

= *E(N-2,1,1) - E(N-1,1,0) - E(N-1,0,1) + E(N,0,0)*, where *E(N-i,j,k)* denotes the total energy of a supercell containing *N-(j+k)* Fe atoms, *j*(= 0 or 1) solute atoms, and *k*(= 0 or 1) vacancies [with the vacancy and solute atom being nearest-neighbors for *E(N-2,1,1)*]. Similarly, the binding entropy can be written analogously to Eq. (4) as:

$$\Delta S_b = k_B \left[\sum_{i=1}^{3(N-1)} \ln\left(\nu_i^{vac} / \nu_i^{vac,sol}\right) + \sum_{i=1}^{3N} \ln\left(\nu_i^{sol} / \nu_i^{bulk}\right) \right] \tag{10}$$

where ν_i^{sol} denotes one of the *3N* phonon frequencies of a supercell containing *N-1* Fe atoms and one solute atom, and $\nu_i^{vac,sol}$ represents one of the *3N-3* frequencies of a supercell containing *N-2* Fe atoms and one nearest-neighbor solute-vacancy pair.

To compute values for the correlation factor (f_2) in Eq. (9), we employ the nine-frequency model of Le Claire [67]. The approach is based on the consideration of the relative rates of the eight different vacancy hops around the solute impurity, illustrated in Fig. 2, plus the hop rate (Γ_0) for the bulk bcc lattice, far from the impurity. The nine frequencies labeled in Fig. 2 correspond to all of the distinct hop rates, under the assumption that the vacancy-solute interaction is appreciable only for the first and second neighbors, and negligible beyond. The results of first-principles calculations performed in this work indicate that the neglect of vacancy-solute interactions beyond the second neighbor is a reasonable assumption for both Mo and W solutes.

In the formalism of Le Claire [67], the correlation factor is written as follows:

$$f_2 = \frac{1 + t_1}{1 - t_1} \tag{11}$$

where t_1 is expressed in terms of the jump frequencies labeled in Fig. 2 as:

$$t_1 = \frac{\Gamma_2}{\Gamma_2 + 3\Gamma_3 + 3\Gamma_3^{'} + \Gamma_3^{''} - \dfrac{\Gamma_3\Gamma_4}{\Gamma_4 + F\Gamma_5} - \dfrac{2\Gamma_3^{'}\Gamma_4^{'}}{\Gamma_4^{'} + 3F\Gamma_0} - \dfrac{\Gamma_3^{''}\Gamma_4^{''}}{\Gamma_4^{''} + 7F\Gamma_0}} \tag{12}$$

with $F = 0.512$. The jump frequencies in Eq. (12) can be expressed as:

$$\Gamma_i = \nu \exp\left(-\Delta H_i^{mig} / k_B T\right) \tag{13}$$

where ν and ΔH_i^{mig} are the attempt frequency and associated migration energy for jump, i, respectively. In the present work, the migration energies, for each of the hops in Eq. (12), are derived from first-principles supercell calculations, as described below. The attempt frequencies are assumed constant for all of the jumps and thus drop out of the expression for t_1. Since the correlation factors for the W and Mo solutes considered here were found to be relatively insensitive to small variations in the Γ values, no attempt was made to refine the calculations of f_2 through direct calculations of the different attempt frequencies.

Over the temperature range of interest, the calculated values of f_2 for W and Mo solutes were found to display relatively weak dependencies on T. To a good approximation, the correlation factor for these solutes can thus be considered as a constant over the relevant temperature range, and the impurity-diffusion coefficient can then be written using Eqs. (3) - (5) and (9) - (10) in the same form as Eq. (6), with the activation energy for the fully-ordered ferromagnetic state given as:

$$Q_0^F = \Delta H_v^f + \Delta H_v^{mig} + \Delta H_b \tag{14}$$

and a prefactor given as follows:

$$D_0 = a^2 f_2 \exp\left[\left(\Delta S_v^f + \Delta S_b\right)/ k_B\right] \times \left[\prod_{i=1}^{3N-3} \nu_i^{vac,sol} \Big/ \prod_{i=1}^{3N-4} \nu_i^{sad}\right] \tag{15}$$

In Eq. (14), the migration energy corresponds to the energy barrier for the exchange of the solute impurity with a nearest-neighbor vacancy.

B.1.2.3 Electronic Contributions

Equations (2) - (5), (10), and (13) account only for vibrational contributions to the vacancy formation, binding, and migration free energies. In earlier first-principles studies of vacancies in bcc transition metals [76,77], it was demonstrated that the additional contributions to these free energies associated with electronic excitations can be significant in some cases. In the present study, electronic contributions to the vacancy-formation, binding, and migration free energies (for Γ and Γ_2) were computed using standard expressions formulated in terms of the calculated electronic densities of states (e.g., [77]). These electronic contributions were found to be relatively small, giving rise to increases in the calculated diffusion constants not larger than a factor of three over the temperature range investigated. These contributions are nevertheless included in the results presented in Section B.1.3 below.

B.1.2.4 First-Principles Calculations

The vacancy-formation, migration, and binding energies, as well as the associated vibrational frequencies defined above, were computed within the framework of DFT as follows. All calculations made use of the projector augmented wave (PAW) method [78,79] and the Perdew-Burke-Ernzerhof (PBE) generalized-gradient approximation (GGA) [80], as implemented in the Vienna Ab initio Simulation Package (VASP) code [81-83]. A cutoff of 300 eV was used for the plane-wave expansion of the electronic wave functions. The PAW potentials used in this work are those labeled Fe, Mo, W, Hf, and Ta in the VASP library. These potentials treat $4s^2 4p^0 3d^6$ electrons as valence for Fe, $5s^2 5p^0 4d^4$ as valence for Mo, and $6s^2 6p^0 5d^n$ (with n = 2,3, and 4) as valence for Hf, Ta, and W, respectively. For each of the supercells considered in this work, the electronic states were sampled using a k-point density equivalent to a 12 x 12 x 12 mesh for a conventional bcc unit cell, and employing the Methfessel-Paxton [84] scheme with a

broadening of 0.1 eV. All calculations were performed spin polarized, with a ferromagnetic ordering of the Fe moments. In all calculations, the positions of the ions within the supercell were fully relaxed at a constant volume and cell shape.

For the calculations of the vacancy-formation, migration, and solute-binding energies, use was made of periodic supercell geometries containing 128 lattice sites (4 x 4 x 4 conventional bcc unit cells). For the representative cases of vacancy formation and migration energies in pure Fe, and W solute-binding and migration energies, several tests were performed to estimate the convergence of the calculated results with respect to the supercell size, plane-wave cutoff, and k-point density. On the basis of these tests, the vacancy-formation, migration, and binding energies are each estimated to be converged to within a precision of approximately 0.05 eV.

Vibrational frequencies were computed using the frozen-phonon approach [85] described in Ref. [86]. Use was made of supercells containing 54 lattice sites (3 x 3 x 3 conventional bcc unit cells), for which all of the **q** = 0 (q is the wave vector) phonon states were computed from the dynamical matrix, constructed as follows. For each cell, all symmetry-inequivalent rows of the **q** = 0 dynamical matrix were determined, with the remaining rows given via symmetry-group transformations [87]. Elements, D_{lm}^{ij}, of the dynamical matrix are proportional to F_l^i, the force acting on the atom, *i*, along the Cartesian direction, *l*, if the atom, *j*, is displaced by a small amount along the direction, *m*, $F_l^i = -\sqrt{M_i M_j} D_{lm}^{ij} u_m^j$, where M_i and M_j are the mass of atoms, *i* and *j*. For each symmetry-inequivalent choice of the displacement, μ_m^i, the forces, F_l^i, were obtained for a set of five evenly distributed displacements around the equilibrium positions, from μ_m^i = - 0.1 to 0.1 Å. The calculated forces

were fit using a third-order polynomial, and the linear terms were used to extract D_{lm}^{ij}. As in the energy calculations, the forces required for the dynamical matrix calculations were computed using a plane-wave cutoff of 300 eV and k-point sampling equivalent to a 12 x 12 x 12 mesh for a conventional bcc unit cell. Convergence tests were performed, examining the effects of the system size, k-point density, and plane-wave cutoff on the vibrational entropy (computed from the **q** = 0 phonon states) for the pure Fe, yielding an estimated precision of 0.05 k_B/atom. The effect of system size was also explored for the vacancy-formation entropy in the pure Fe, through a comparison of results obtained from supercells containing 54 and 128 lattice sites. The effect of the supercell size on the vacancy-formation entropy was a change of approximately 20 percent.

For the calculation of migration energies and associated vibrational frequencies, an important issue concerns the location of the saddle-point position for the diffusing atom. As illustrated in Fig. 2, nearest-neighbor vacancy hops involve the displacement of a neighboring atom along the <111> direction in the bcc lattice. In recent work involving the development of classical interatomic potentials models for Fe [88], the energy as a function of position for an Fe atom exchanging with a vacancy on the bcc lattice was performed with three different potentials. One potential gave rise to an energy versus displacement plot containing a single maximum (saddle point) at the high-symmetry location, a[1/4,1/4,1/4]. In contrast, the other two potentials produced two maxima along this path, separated by a local minimum at the same high-symmetry point - these potentials thus predicted saddle-point positions away from the a[1/4,1/4,1/4] position.

To determine the location of the saddle point predicted by DFT, for the Fe self-diffusion as well as for the impurity diffusion of representative solute atoms, calculations were undertaken in the present work employing the nudged-elastic band (NEB) method [89,90]. Such calculations

were performed for the nearest-neighbor exchange of Fe, W, and Hf ions with vacancies in the bcc Fe. In all cases, the energy was found to display a single maximum, corresponding to a saddle point at the high-symmetry position located half way between neighboring sites. For Fe self-diffusion, the results are in good agreement with those obtained by Fu *et al*. [91]. For nearest-neighbor vacancy exchanges with Mo and Ta ions, and for all of the other migration-energy calculations required in the calculation of the correlation factor [c.f., Eq. (12) above], the saddle-point configurations were determined as follows. The diffusing atom was initially placed at the position half way between neighboring sites, and the structure of the supercell was subsequently relaxed using a quasi-Newton algorithm based on the calculated forces. In all cases where frozen-phonon calculations were performed using the resulting relaxed structures, the saddle-point nature of the solution was verified by the fact that the vibrational spectra contained a single imaginary frequency with an associated eigenvector corresponding to a displacement of the diffusing ion along the transition path.

B.1.3 Results and Discussions

Table I lists the vacancy formation, migration, and binding energies computed in the present study, as well as the associated activation energies for self- and impurity-diffusion in the paramagnetic and fully-ordered ferromagnetic states. Results are presented for the pure bcc Fe as well as for W, Mo, Ta, and Hf impurities.

The binding energies reported in Table I refer to nearest-neighbor solute-vacancy pairs, and all are found to be negative (attractive) and appreciable in magnitude. These binding energies can be compared to those derived from first-principles calculations for Cr [17,23,24], Ni [24], Cu [11], and P [14] substitutional impurities in Fe. For all of these elements, the vacancy-solute binding energy is calculated to be attractive, as found here for W, Mo, Ta, and Hf.

The magnitudes of the binding energies published for Cr (0.05 - 0.06 eV) and Ni (~ 0.07 eV) are somewhat smaller than those for the solute species considered here, while the values for Cu (0.16 eV) and P (0.32 eV) are comparable to those computed for W, Mo, and Ta, respectively. Relative to the other substitutional impurities considered in this and previous studies, the Hf impurity is found to display anomalously large binding to a neighboring vacancy.

For the pure Fe, the vacancy formation and migration energies obtained here are consistent with the range of values of ΔH_v^f = 1.93 - 2.18 eV and ΔH_v^{mig} = 0.64 - 0.71 eV published previously from GGA-based DFT calculations [11,17,23,24,92,93]. The migration energies for the solutes in Table I correspond to a nearest-neighbor exchange with a vacancy. Of the solutes considered here, only W shows a larger value of ΔH_v^{mig} than that for the Fe self-diffusion, while Hf exhibits the lowest value. When the vacancy formation, binding, and migration energies are combined to compute the ferromagnetic activation energies (Q_0^F) from Eqs. (7) and (14), it is seen that all solutes have a smaller calculated value than that for the Fe self-diffusion in the ordered ferromagnetic state.

For the high-temperature paramagnetic phase, the estimated values of the activation energy (Q^P) are derived from the first-principles-calculated value of Q_0^F through the relation $Q^P = Q_0^F/(1+a)$, expressed in terms of the parameter, α, defined above. For Fe, Mo, and W, the value of this parameter has been obtained with the published measurements [52,69] given above, while for Ta and Hf, the values quoted in Table I are estimated, based on an empirical linear correlation between α and $\Delta M_{1\text{-}2}$, the induced change in the local magnetic moments for the first and second neighbor Fe atoms surrounding the solute impurity [24,69]. Specifically, the values of $\Delta M_{1\text{-}2}$ were computed for Nb, W, Mo, Cr, Fe, and Co from first-principles calculations employing the methods described in Section B.1.2.4; a linear relation was then fit between the

measured values of α for these solutes, and the first-principles calculated values of $M_{1\text{-}2}$. The resulting fit reproduced the measured values of α to better than 20 percent. Using the resulting fit, the values of α given in Table I for Ta and Hf were estimated from calculated values of $\Delta M_{1\text{-}2}$. Comparing the predicted values of Q^P, it is seen that only W is predicted to have a slightly larger value of the activation energy in the paramagnetic phase than that for the Fe self-diffusion, while Hf is again seen to display the lowest value.

We focus for the remainder of this section on W- and Mo- impurity diffusion. For both species, the vibrational frequencies, and all of the migration energies required to compute the correlation factor (f_2) have been calculated. We are thus able to compute the diffusion prefactors as well as activation energies for these solutes, allowing a direct comparison of the first-principles results for temperature-dependent diffusion constants with the experimental measurements.

Table II lists the calculated values of f_2 for W and Mo at representative temperatures of 800, 1,000, and 1,200 K. While for W, the values are very similar to the correlation factor for the pure Fe ($f_0 = 0.727$), for Mo, the values are roughly a factor of 2 to 3 smaller. As mentioned above, the temperature dependencies of the calculated values of f_2 are relatively weak in comparison to the Arrhenius terms in the associated diffusion constants. For Mo, the calculated results for f_2 in Table II are noted to be significantly smaller than the range of values of 0.87 - 0.90, for temperatures between 823 and 1,173 K, obtained in a recent analysis by Nitta *et al.* [95]. In their analysis, Nitta *et al.* made use of measurements of the concentration dependencies of the intrinsic diffusivities of Fe and Mo in bcc Fe-Mo solid solutions. The data were analyzed in the framework of the nine-frequency model described in Section B.1.2.2, but with some simplifying assumptions, including: $\Gamma_3' = \Gamma_3''$, $\Gamma_4' = \Gamma_4'' = \Gamma_0$, and $\Gamma_3 / \Gamma_3' = \Gamma_4 / \Gamma_5$. The discrepancy between

the estimated values for f_2 obtained by Nitta *et al*. and those derived in the present study is attributed to the fact that the relations between the hopping frequencies assumed in Ref. [95] are not found to hold in the first-principles calculations. For example, Γ_4 is calculated to be more than twice larger than Γ_4'' at 1,200 K.

Tables III - V list the calculated diffusion prefactors (D_0) and activation energies (Q^P and Q_0^F) for the Fe self-diffusion and W- and Mo-impurity diffusion. Each is compared to available published values, based on analyses of the experimental data. For the Fe self-diffusion, the calculated value of Q_0^F is roughly in the middle of the range of published values, while the present calculated value for Q^P is on the lower end of the range reported from the experimental measurements. The magnitude of the prefactor of the Fe self-diffusion calculated here is on the order of 10^{-4} m^2/s and is comparable to a number of published values in this same range, while being inconsistent with the higher values of around 10^{-2} m^2/s derived in some analyses.

For the W-impurity diffusion, both Q_0^F and Q^P are on the lower end of the range of the measured values. For the Mo-impurity diffusion, the calculated activation energies in the ferromagnetic and paramagnetic states display values in the middle of the range of the experimentally-derived estimates. The magnitudes of the prefactors for W and Mo impurity diffusion obtained from the first-principles calculations are similar to those derived for the Fe self-diffusion, on the order of 10^{-4} to 10^{-5} m^2/s, which is consistent with some of the published values with the same order of magnitude, while being much smaller than the values in the range of 10^{-2} to 10^{-1} m^2/s reported in others.

Figures 3 - 5 present a direct comparison between the calculated and measured temperature-dependent diffusion coefficients for the Fe self-diffusion (Fig. 3), and W and Mo impurity diffusion (Figs. 4 and 5, respectively). The diffusivities are calculated from 0 K to 1,184

K, the α-γ transition temperature. For the Fe self-diffusion, the agreement between calculations and measurements in the ferromagnetic phase is excellent, while the calculated values underestimate slightly (by a factor of 2 - 4) the measured values in the paramagnetic phase at the highest temperatures due to an apparent slight underestimation of the slope on the Arrhenius plot (i.e., the activation energy).

We focus next on a comparison of the calculated and experimentally-measured impurity-diffusion coefficients for Mo and W. The most recent measurements have been undertaken by the Iijima et al's group [52,53], and should be used as the basis for quantitative comparisons with the calculations. Considering first the W-impurity diffusion, the measurements in Ref. [52] made use of the high-purity Fe, and impurity diffusivities were measured by tracer analyses over the temperature range of 833 to 1,173 K, employing magnetron sputter-microsectioning, radio-frequency sputter-microsectioning, and ion-beam sputter-microsectioning techniques. At 1,053 K, the reported experimental value of the W-impurity diffusivity is 8.94×10^{-17} m^2/s, which is in very good agreement with our calculated value of 6.23×10^{-17} m^2/s at the same temperature. The measured results in the paramagnetic phase due to Takemoto *et al.* [52], Kucera *et al.* [63], and Alberry and Haworth [64] agree fairly well, but those due to Gruzin [47] and Kieszniewski [62] are higher by a factor of up to 5. Possible reasons for these discrepancies could include differences in the impurity and grain sizes of the starting materials, instrumental accuracy in the older measurements and/or surface-stress effects. The calculated diffusion coefficients show good overall agreement with the measured values in the ferromagnetic phase obtained by Takemoto *et al.* [52], although the calculated values are seen to be larger than these measurements at the lowest temperatures. The calculations are similarly in good agreement with the measurements of Refs. [52,63,64] in the

paramagnetic phase, leading to at most a factor of 2 - 5 underestimation of the measured data at the highest temperatures.

For the Mo-impurity diffusion, the measurements of Nitta *et al.* [53] made use of the same starting materials and similar experimental techniques as those listed above for the W measurements of Ref. [52]. At 1,050 K, the measured values of the Mo-impurity diffusivity is 1.26×10^{-16} m^2/s [53], which is in very good agreement with our calculated value of 1.44×10^{-16} m^2/s. Borisov *et al.* [65], Kucera *et al.* [63], and Alberry and Haworth [64] reported measurements of the Mo-impurity diffusivity in the paramagnetic phase over a small temperature range, and their values are higher (by as much as an order of magnitude) than those reported by Nitta *et al.* [53]. Possible reasons for this large discrepancy include the factors listed above. Nohara and Hirano [66] also determined the tracer diffusivity or Mo impurities in both the ferro- and paramagnetic phases, but their values are lower by a factor of 2 - 3 than those due to Nitta *et al.* [53]. There is a slight discrepancy between the presently-computed and measured data of Nitta *et al.* [53] in the ferromagnetic phase and, as with W, this discrepancy increases at lower temperatures. Nevertheless, for Mo, our predictions overestimate by no more than a factor of 2 - 5 the measured values in the ferromagnetic state, while the predicted values show even better agreement with the published experimental data in the paramagnetic phase.

It is noteworthy that while the diffusion coefficients are well predicted by the calculations for Fe at both low and high temperatures, the calculated solute-impurity diffusivities show relatively better agreement with measurements at high T, and larger discrepancies at low T. Given that the DFT results should be most accurate for the low-temperature ordered ferromagnetic phase, for which all of the calculations were performed directly, further studies would be of interest to understand whether the larger discrepancy with the experimental

measurements at the lowest temperatures is due to systematic errors in the calculations, or inherent difficulties associated with the measurements at low *T*. Overall, considering that the calculations do not involve any adjustable parameters, the agreement between the computed and measured results over the relevant temperature range is viewed to be highly encouraging, and suggests that the computational methodology presented in this paper provides sufficient accuracy to be useful in the context of designing coarsening-resistant microstructures.

As mentioned in Section B.1, the motivation for this work is the development of a computational framework to assist in identifying slow-diffusing elements in a bcc Fe matrix, for the design of coarsening-resistant nanoscale-precipitate microstructures in Fe-Ni-Al-Cr-based alloys. This goal is motivated through the analogy with two-phase Ni-based superalloys. In Ni, many 4d and 5d TM solutes display impurity-diffusion coefficients, which are orders of magnitude smaller than the self-diffusivity in the pure Ni [13,15]. The addition of these TM elements correlates with substantial improvements in the coarsening resistance and high-temperature creep properties of modern commercial Ni-based superalloys. Thus, it is desirable from the standpoint of the design of analogous two-phase ferritic alloys to see whether such slow-diffusing solutes can be identified. We consider this question in light of the computed data in Table I and the results of the current calculations (Tables III, IV, and V).

Figure 6 shows that for the two 4d and 5d TM solutes considered in the present work, namely Mo and W, the calculated impurity-diffusion coefficients are equal to or larger than the diffusivity for the Fe self-diffusion. The main effects underlying this result are shown in Tables III - V to be the slightly lower values of the activation energies of W- and Mo-impurity diffusion, compared to the Fe self-diffusion - the diffusion prefactors are computed to have comparable magnitudes. The lower values of the activation energies for Mo- and W- impurity diffusion can

be seen in Table I to be due to both the appreciable and negative values for the vacancy-solute binding energies, and a slightly reduced value of the migration energy in the case of Mo. If we assume that the diffusion prefactor is roughly constant, as the calculated results in Tables III - V seem to suggest, the first-principles data in Table I indicate that the comparable or higher values of the impurity-diffusion coefficients relative to self-diffusion in the bcc Fe may be more general for other 5d TM alloying elements, for which the measured data in the pure bcc Fe is lacking. Specifically, both Ta and Hf impurities are computed to have substantially lower values of the activation energies than that for the Fe self-diffusion in Table I. The trend towards higher values of impurity-diffusion constants relative to self-diffusion is also consistent with the measured data for 4d elements compiled in Fig. 1.

The calculated and measured results compiled in this work stand in sharp contrast to the Ni-based alloys, where activation energies vary by more than a factor of two for 4d and 5d solutes, with the associated diffusion constants at relevant temperatures varying by more than four orders of magnitude at 1,173 K [13]. The current results and the measured data plotted in Fig. 1 suggest an absence of comparable slow diffusers amongst the common solute additions to the bcc Fe. An outstanding question that deserves further attention is whether the apparently smaller variations in the impurity-diffusion coefficients for TM solutes in the bcc Fe, relative to the fcc Ni, is due to the differences in bonding (an electronic structure) in these systems, or the geometrical differences of the more open bcc lattice, relative to the close-packed fcc structure. To address this question, it would be interesting to extend the computational framework described here more generally to other bcc elements, to further investigate the general trend of the variations of the TM impurity-diffusion coefficients in other bcc hosts.

An important observation that can be made from the results presented in this paper is

the absence of the often-assumed correlation between the magnitude of the impurity diffusivity and the atomic size of the solute. While such a correlation is often assumed as a useful "rule of thumb," it clearly breaks down in the case of the impurity diffusion in the bcc Fe. This point is apparent when considering the measured impurity-diffusion coefficients for the four oversized TM solutes Ti, Mo, W, and Ta, in comparison to that for the undersized Co solute. The atomic volumes ($Å^3$) in the stable room-temperature structure [94] for these solutes and pure Fe are: Fe (11.78), Co (11.07), Ti (17.64), Mo (15.58), W (15.85), and Ta (18.01). In Fig. 1, the lowest and highest impurity diffusivities occur for the smallest (Co) and largest (Ti) of these solutes, respectively. Further, while Mo, W, and Ta have atomic volumes roughly 30 - 50 % larger than Co, their impurity diffusivities are comparable to or even slightly larger in magnitude. The lack of a correlation between the atomic size and the magnitudes of impurity-diffusion coefficients in Ni [13] and Al [20] has also been discussed previously. Collectively, these previous studies and the present work demonstrate that the search for slow-diffusing elements should be based on more detailed considerations of the chemical (electronic-structure) factors underlying the magnitudes of the migration and solute-vacancy binding energies and entropies, rather than a simple size effect.

It should be emphasized that the present calculations and the compiled experimental data in Fig. 1 are associated with the impurity-diffusion coefficients for highly dilute solute concentrations in the pure bcc Fe. From the standpoint of developing coarsening-resistant bcc-based microstructures, at the higher solute compositions employed in real alloys, it may be important to consider the concentration dependencies of the relevant diffusivities. For example, Nitta *et al.* [95] recently reported results of measurements for the concentration dependence of both Fe and Mo tracer-diffusion coefficients in binary bcc Fe-Mo alloys. In this system, the

diffusion coefficient of Fe is measured to increase with increasing the Mo content, whereas that for Mo decreases. For concentrations greater than 1.5 atomic percent (at. %) Mo concentration, the solute tracer-diffusion coefficient becomes slower than that for Fe at high temperatures. It is also interesting to consider the published results indicating that in dilute Fe(V) alloys, Hf impurities display a diffusion coefficient, which is as much as 3 orders of magnitude lower than that for Fe [96]. The current calculated results for activation energies presented in Table I suggest that in the pure bcc Fe, Hf impurities should display very high relative diffusion constants (assuming that the diffusion prefactor is not anomalously low). To reconcile the measurements and calculations in the case of Hf, it would be interesting to investigate the effects of V solutes on Hf-impurity diffusion in the bcc Fe. Overall, it would be of interest to extend the formalism presented in this paper to the study of the concentration dependencies of relevant diffusion coefficients for non-dilute Fe alloy compositions. While such studies lie beyond the scope of the current work, they should be possible by generalizing the first-principles formalism presented in Ref. [21] to magnetic bcc Fe-based systems.

B.1.4 Conclusions

A framework involving the combination of first-principles DFT calculations and a semi-empirical correction for magnetic effects has been outlined to predict temperature-dependent self- and substitutional-impurity-diffusion coefficients in the ferromagnetic and paramagnetic phases of the bcc Fe. The activation energies are determined from the DFT-calculated vacancy formation, migration, and nearest-neighbor solute-vacancy binding energies in the ordered ferromagnetic state. The diffusion prefactors are derived from the DFT calculations of longer-ranged solute-vacancy binding and migration energies, and the relevant vibrational and electronic entropies, employing the Vineyard's harmonic transition-state

theory and the Le Claire nine-frequency formalism.

The computational approach has been applied to calculations of Fe self-diffusion, and impurity-diffusion coefficients for W and Mo solutes in the bcc Fe. The computational results are compared with available experimental measurements in the temperature range of 800 to 1,184 K. Calculated and measured self- and impurity-diffusion coefficients are found to agree within a factor of five over this temperature range, with the level of agreement between experiments and theory being comparable to the scatter of the experimental data in the high-temperature paramagnetic phase. The calculated impurity-diffusion coefficient for Mo is larger than the self-diffusivity of the bcc Fe over the entire temperature range below the α-γ phase transition. The calculated activation energies for Ta and Hf impurities suggest that these solutes should also display impurity-diffusion coefficients larger than that for the Fe self-diffusion. For W, the calculated impurity-diffusion coefficient is comparable to and larger than the Fe self-diffusivity in the paramagnetic and ferromagnetic phases, respectively.

The current computational study is motivated in the context of the design of nanoscale-precipitate-strengthened ferritic alloys, where the identification of slow diffusing solutes in the bcc matrix is desirable for the optimization of coarsening and creep resistance. The accuracy of the results obtained in this study suggests that the proposed computational approach should provide a useful tool to aid in the development of kinetic databases for such alloy-design efforts.

B.2 Alloy Design and Fabrication

Based on the previous work on the thermodynamic calculations at Northwestern University (NU) and alloy-design efforts at NU and Oak Ridge National Laboratory (ORNL), a total of fourteen alloys have been prepared by arc melting. Their compositions are shown in

Table VI. Here the alloy designation “FBB” means Fe-based alloys containing mainly the Beta-phase (a disordered bcc A2 phase) matrix and Beta prime phase (an ordered bcc B2 phase) precipitates. Alloying beyond the ternary regime is needed to meet various property objectives, such as the coarsening resistance, oxidation resistance, misfit between the matrix and precipitate, grain growth, and grain-boundary sliding.

The alloy FBB-1 is the base composition, which contains ~ 20 volume percent (vol.%) of the B2 phase at 973 K. FBB-2 is a modification of FBB-1 with additions of 3.4 weight percent (wt.%) Mo for solid-solution strengthening of the A2 matrix, 0.25 wt.% Hf for the slow diffusion in the matrix, and 0.005 wt.% B for enhancing the grain-boundary cohesion. FBB-3 is a modification of FBB-2 with additional 0.25 wt.% Zr instead of Hf mainly for possible slow diffusion in the matrix and grain-boundary strengthening. In addition, the material cost of Zr is substantially lower than that of Hf. Recent studies indicate that stable carbides based on MC (metal carbides) compositions are very effective in strengthening ferritic steels at elevated temperatures. Small additions of Nb, V, and C were, thus, added to FBB-4 for possibly MC-carbide hardening. Alloys FBB-3, -7, -8, -9, -12, -13, and -17 were designed with various amounts of Al ranging from 3 ~ 10 wt.%, with the same composition of other elements on the basis of FBB-3. Mo is added to dilate the matrix. Hence, it will reduce the lattice mismatch. Based on FBB-8, the addition of 6.3 wt.% W in FBB-8W1 is to replace all the Mo for further solid-solution strengthening of the A2 matrix. Similarly, half atomic percent of Mo was replaced with W in FBB-8W2. FBB-14 and -15 alloys were designed with additions of 0.5 wt.% and 1 wt.% Zr in order to examine the effects of Zr on the creep properties.

The alloys were fabricated by vacuum arc-melting, then drop cast into a Cu mold with dimensions 12.7 x 12.7 x 76.2 mm. A rod 20 mm long was, subsequently, cut from the ingot.

They were solution-treated at 1,473 K for 30 min. in evacuated and sealed quartz tubes, followed by air-cooling, and then aged at 973 K for 100 hrs. The cooling rate was roughly estimated to be 60 K min^{-1}.

B.3 Microstructural Characterizations

B.3.1 Introduction

Similarly to the γ/γ′ Ni-based superalloys, the creep resistance and room-temperature ductility of the NiAl-strengthened ferritic steels are expected to be a strong function of the microstructural characteristics of the β′ precipitates, such as the volume fraction, average size, lattice parameter, and chemistry. Further improvement in the creep and ductility properties and understanding of the room-temperature and high-temperature mechanical behaviors require systematic microstructural characterizations of these strengthening precipitates. Specifically, the phase-transformation processes and resulting microstructures, the composition of the β′ precipitates, and the partitioning behavior of the alloying elements in relation to the alloy chemistry, have not been thoroughly investigated in the literature.

B.3.2 Experimental Methods

B.3.2.1 Phase Transformation

A differential-scanning calorimeter (DSC), NETZSCH 404C, was used to study the phase transformation in alloys FBB-3, -7, -8, and -12. A small piece of sample with a mass of about 50 mg was measured in Al_2O_3 crucible under an argon atmosphere at a constant heating rate of 40 K/min. from 293 to 1,773 K.

B.3.2.2 Transmission-Electron Microscopy (TEM)

Three-millimeter-diameter cylindrical rods, both as-quenched (from 1,473 K) and heat-treated (973 K for 100 hrs) conditions, are obtained from the Oak Ridge National

Laboratory (ORNL). Slices are cut using a Struers Accutom-5, and are ground to less than 100 μm in thickness. Thin foils for TEM are prepared by a Fischione dual jet polisher. An electrolyte containing the 20 vol.% perchloric acid in methanol is maintained at 233 to 238 K, and the thin folis are prepared by applying a voltage of 40 V and current of 40 - 50 mA. Conventional TEM is carried out in a Hitachi 8100 microscope operating at 200 kV. Bright-field (BF) and dark-field (DF) imaging, and selected-area diffraction (SAD) are performed as a part of the microstructure characterization. All DF micrographs are taken using the (100)-type superlattice reflection only.

B.3.2.3 Analytical-Electron Microscopy (AEM)

Thin-foil preparation is the same as that described in the above TEM experimental methods. Analytical characterization was performed in a cold-field emission-gun high-resolution AEM (Hitachi HF-2000) equipped with an ultrathin window (ATW) Link energy-dispersive X-ray (EDX) detector and data processor (QX2000). The AEM was operated at 200 kV. The take-off angle for the X-ray detector was 68°. The X-ray collection time was between 200 and 300 s, and the electron probe size was about 10 nm. Care was taken to avoid a two-beam condition in order to minimize electron-channeling effects [97]. The X-ray spectra were deconvoluted, to separate the overlapping peaks, and the background-subtracted integrated intensities were obtained, using the Desktop Spectrum Analyzer (DTSA 2.5.1) software [98].

The background-subtracted integrated intensities of EDX spectra may be converted to compositions [97]. In the case of the Fe-based matrix, the following equations may be used

$$\frac{w_j}{w_{Fe}} = k_{j/Fe}\frac{I_j}{I_{Fe}}[ACF]\frac{1}{\left(1+\frac{I^j}{I_j}\right)} \tag{16}$$

$$\sum_{j=1} w_j = 1 \tag{17}$$

where w_j is the weight fraction of element, j (Al, Cr, Fe, Ni, Mo…etc.), and $k_{j/Fe}$ is the proportionality constant or the Cliff-Lorimer factor [99], I_j is the X-ray intensity of element, j, and I^j/I_j is the ratio of the fluorescence intensity to primary intensity. Although there are several ways to define I_j, we have taken I_j as the background-subtracted integrated intensity of the K_α peak of element, j. Equations analogous to Eq. (16) and Eq. (17) may be written for NiAl-type precipitates. The absorption correction [100], the fluorescence correction [101], and the relevant material parameters [102] are described elesewhere.

To quantify the Fe-matrix composition, it is necessary to know the $k_{j/Fe}$ factors, where the concentration of Fe is taken as the dependent quantity, for a given microscope, and its operating conditions. Similarly, to quantify the precipitate composition, it is necessary to know $k_{j/Ni}$ factors where the concentration of Ni is taken as the dependent quantity. Due to the multicomponent nature of both the matrix and precipitate, a large number of suitable standards are needed. Therefore, we report the ratio of integrated intensities only for FBB-1, -2, and -7. We have determined these k factors using thin foils of single-phase specimens of known compositions or standards for the AEM HF2000 operating at 200 kV for FBB-3, -8, and -12.

For the foil thickness of 100 nm or less, Cr, Fe, Ni, and Mo satisfy the criteria of a thin foil, i.e., absorption and fluorescence effects are negligible. The Cliff-Lorimer factor for Al was determined using the extrapolation method [97] due to the strong thickness dependence.

The compositions of the Fe matrix and NiAl-type phases in FBB-3, FBB-8, and FBB-12 were determined by analyzing up to 25 EDS spectra of each phase. The uncertainty (or error) of the measured compositions is estimated by the statistics of the student t-distribution. For example, in the case of the Fe matrix, the total relative error ($\Delta\varepsilon_{wj}$) in the determination of compositions is given by [97]

$$\Delta\varepsilon_{wj} = \Delta\varepsilon_{k_j/Fe} + \Delta\varepsilon_{I_j/I_{Fe}} \tag{18}$$

where $\Delta\varepsilon_{k_j/Fe}$. and $\Delta\varepsilon_{I_j/I_{Fe}}$ are the relative errors associated with *k* factors and in the counting statistics of X-rays in the specimen of unknown compositions, respectively. They are given by [97]

$$\Delta\varepsilon_{k_{j/Fe}} = \frac{t_{99}^{n-1}}{\sqrt{n}} \frac{\sigma_k}{k_{j/Fe}} 100 \tag{19}$$

$$\Delta\varepsilon_{I_j/I_{Fe}} = \frac{t_{99}^{n-1}}{\sqrt{n}} \frac{\sigma_k}{\overline{I_j/I_{Fe}}} 100 \tag{20}$$

where t_{99}^{n-1} are the student-t values for *n* measurements at a 99% confidence level; σ_k and σ_I are the standard deviations for the *k* factor and intensity-ratio measurements, respectively; $k_{j/Fe}$ is the mean of the *n* values of the *k* factor, and $\overline{I_j/I_{Fe}}$ is the mean of the *n* values of I_j/I_{Fe}. Equations analogous to Eq. (18) to Eq. (20) may be written for NiAl-type precipitates.

B.3.3 Results and Discussions

B.3.3.1 Phase Transformation

Preliminary DSC studies on the as-cast materials revealed that there was no strong peak observed around the solvus temperature of NiAl due to the formation of a limited amount of the NiAl phase. Therefore, it was not able to determine the phase-transition temperatures, especially the solvus temperature of NiAl precipitates. Consequently, aged materials were used for DSC studies to form a sufficient amount of NiAl precipitates. The DSC-heating curves of the alloys are compared in Fig. 7(a). All curves show that the transformation from β′ to β starts at a temperature [$T_{\beta'(NiAl)}$] of about 1,023 K and completes at a temperature (T_β) around 1,323 K. Therefore, the solution-treatment temperature (1,473 K) used in this study was adequate. There is another exothermic transition peak at a temperature higher than $T_{\beta'(NiAl)}$ for the alloys containing

less Al (FBB-8 and FBB-12). This feature is most likely to be the FeAl-phase separation (also a β′ phase) inside the NiAl particles, which was suggested by the investigation of an Al-rich Fe-23.2Al-4.1Ni (at.%) alloy system by Liu et al. [103]. They revealed that two kinds of B2 phases (NiAl and FeAl) coexist in a Fe-Ni-Al system, when the as-quenched alloy was aged at a temperature around 998 K. In other words, this separation depends on the alloy composition, as this transition peak was not observed in the alloys with higher Al contents (FBB-3 and FBB-7). To determine whether the formation of a possible FeAl phase occurred during the aging or the solution-treatment process, the DSC studies were also carried out on the solution-treated alloys FBB-3 and FBB-8. A comparison of the DSC curves in the solution-treated and aged conditions is shown in Fig. 7(b). As can be seen, the DSC curves of FBB-3 did not reveal the FeAl peak in neither a solution-treated nor aged condition. The FeAl-phase peak was not observed in the solution-treated but in the aged FBB-8, which suggests that the formation of the FeAl phase most likely occurred during the aging process.

In Fig. 7(a), the endothermic peak at a temperature of ~ 923 K is most likely the solvus temperature of the secondary NiAl precipitates [27]. However, the ferromagnetic to paramagnetic transition temperature (T_c) of the Fe-Al-Ni system was reported [104] to be also between 873 and 973 K. Therefore, further studies will need to be carried out to verify this phase transition. Another small endothermic peak (T_γ) is observed in all alloys except FBB-12 around 1,523 K, i.e., between T_β and the melting temperatures (T_m). Marcon et al. reported that depending on the composition, the γ-Fe loop exists in the isoplethal section from the Fe corner to NiAl in the Fe-Ni-Al system [104]. Therefore, this feature reveals a possibility of a small amount of α Fe transforming to γ Fe. However, it was reported that this transformation can be suppressed by the small addition of Al [2.5 atomic percent (at.%)] in the Fe-NiAl pseudo-binary phase

diagram [105]. The difference might be due to the much complex alloy systems in our study. Also, as indicated in Fig. 7, T_m shows a slight decrease with increasing the Al content.

B.3.3.2 TEM

Figures 8, 9, 10, 11, 13, 14, and 15 show the TEM micrographs of FBB-1, -2, -3, -4, -7, -8, and -12, repectively. In all cases, TEM micrographs are shown in both as-quenched and heat-treated conditions. Even though both BF and DF micrographs are taken in all specimens, the shape, size, and the state of coherency of *B*2 precipitates are visualized better in the DF micrographs taken using the (100)-type superlattice reflection.

All alloys show the nucleation and growth of *B*2 precipitates in as-quenched specimens. Our previous research (yet unpublished) at NU has shown that the nucleation of *B*2 precipitates in such alloys can not be suppressed even by quenching the liquid alloy using a melt-spinning process.

In FBB-1 (Fig. 8), -3 (Fig. 10), -4 (Fig. 11), -7 (Fig. 13), and -8 (Fig. 14), the *B*2 precipitates are fully coherent in both as-quenched and heat-treated conditions. This feature is inferred from the absence of any interfacial dislocation around the *B*2 precipitates. In FBB-2 (Fig. 9), the B2 precipitates are fully coherent in the as-quenched state, but they seem to be semicoherent after the 973 K heat treatment. Most of the *B*2 precipitates in Fig. 9(d) show the presence of a few interfacial dislocations. Figures 10 and 11 demonstrate that relatively larger precipitates are undergoing a coherency-induced morphological transition, from a spherical to cuboidal shape, as predicted by the theory of the strain-induced microstructure evolution in a two-phase system. As seen in Fig. 15, most NiAl-type (*B*2) precipitates are fully coherent in FBB-12. However, some appear to be semicoherent due to the presence of interfacial dislocations.

In FBB-7 and FBB-8, *B*2 precipitates seem to have undergone further phase separation during quenching and aging (see dark regions within *B*2 precipitates in Fig. 13c and Fig. 14d). This trend has most likely originated from the alloy composition, which in turn has caused changes in tie-line composition of *B*2 precipitates. In FBB-1 to FBB-4, the alloy compositions are such that the NiAl-type precipitates are nearly stoichiometric, whereas in FBB-7 and FBB-8, the NiAl-type precipitates are Ni-rich. In our previous research, sponsored by the Electric Power Research Institute (EPRI), we found that depending on the alloy composition, the *B*2 domains may phase-separate into NiAl- and FeAl-types during quenching, the latter being dispersed only within the NiAl-type domain and has nanoscale dimension. During subsequent aging at 973 K, the FeAl-type domains (within NiAl-type particles) undergo disordering to form α-Fe regions within NiAl-type particles. These are some of the possible reasons why nanoscale dark regions are observed within NiAl-type precipitates in Fig. 13d and Fig. 14d.

Besides *B*2 precipitates in an Fe matrix, minor phases are also observed in FBB-2, FBB-3, and FBB-4. This trend is expected due to the additions of B and C. As an example, Fig. 12 shows the morphology and distribution of minor phases. Figure 12(a) presents the irregular-shaped particles in the as-quenched FBB-2, while Fig. 12(b) exhibits lath-shaped particles in the aged FBB-3. However, no attempt was made to characterize these phases.

As a relative measure of the coarsening resistance in the prototype alloys, we have measured the average diameter of *B*2 precipitates in each specimen. Such measurements are carried out directly in the TEM negatives and consider 20 particles only. Even though the measurements of 20 particles are insufficient for any rigorous statistical analysis, a preliminary analysis is presented to validate our original assumption on decreasing the coarsening rate by adding slow diffusing elements, such as Hf.

The measured precipitate-size data is presented in Table VII. We note that in the as-quenched state, the mean diameter of *B*2 precipitates in FBB-2, FBB-3, and FBB-4 is larger than in FBB-1, but the standard deviation is very similar. This trend is also obvious in the DF-TEM micrographs, for example, if Fig. 8(b) and Fig. 9(b) are compared. While a variation in the quenching rate is a possibility, a larger diameter may also originate from a higher nucleation temperature, thus a larger temperature interval for growth during quenching, in FBB-2, FBB-3, and FBB-4 than in FBB-1. Due to the addition of Mo in FBB-2, FBB-3, and FBB-4, it is most likely that the misfit strain in these alloys has been reduced, compared to FBB-1, thus reducing the nucleation barrier as well. This trend might have facilitated the nucleation of *B*2 particles at a higher temperature, also allowing for a larger temperature interval for growth during quenching.

After aging at 973 K for 100 hrs, the mean diameter (D) of *B*2 precipitates fall in the range of 90 to 130 nm. Now, we compare the ratio of the mean volume of precipitates, V_{973}/V_{AQ} [= $(D_{973}/D_{AQ})^3$] , as a relative measure of the coarsening resistance. It is seen than V_{973}/V_{AQ} in FBB-2, FBB-3, and FBB-4 is much smaller than in FBB-1. Even though D_{973} does not vary significantly from one alloy to another, the ratio, V_{973}/V_{AQ}, is affected by the initial precipitate size. As anticipated in the beginning of this research, Hf seems to be a better candidate than Zr as far as imparting the coarsening resistance. It is seen that the values of V_{973}/V_{AQ} in FBB-7 and FBB-8 are one to two orders of magnitude smaller than in FBB-1 to FBB-4, indicating the improved coarsening resistance.

B.3.3.3 AEM

The representative EDX spectra from the matrix and precipitate(s) in FBB-1, -2, and -7 are shown in Figs. 16, 17, and 19. The ratio of the integrated intensities are listed in Tables VIII and IX, where the relevant quantities are refered to the intensity of Fe for the matrix phase, and

to the intensity of Ni for the NiAl-type precipitate. The values presented in Tables VIII and IX are based on ten spectra collected from each phase. No attempts were made to quantitatively determine the compositions in the matrix and precipitate for these three alloys.

Due to a reduction of the Al content in FBB7, compared to FBB2, there is a decrease in the Al content in the matrix as the tie-line has shifted towards the Fe-rich corner. A visual examination of the EDX spectra from NiAl-type precipiates in FBB1 [see Fig. 16(b)], FBB2 [see Fig. 17(b)], and FBB7 [see Fig. 19(b)] demonstrates the evidence of Cr and Fe partitioning to NiAl-type precipitates. However, it is obvious that Cr and Fe partitioning to NiAl-type precipitates is affected by the alloy composition, as the tie-line compositions change with the alloy chemistry. In all alloys, the partitioning of Mo in NiAl-type precipitates is barely detectable. Consequently, due to the poor X-ray counting statistics, the I(Mo)/I(Ni) ratio shows a large relative error (see Table IX). Another important result is that neither the matrix nor precipitate EDX spectrum of FBB2 and FBB7 shows the evidence of Hf and Zr, respectively. These alloys are supposed to contain 0.25 wt.% Hf and Zr, respectively.

The representative EDS spectra of the Fe matrix and NiAl-type precipitate, taken from FBB-3, FBB-8, and FBB-12, are shown in Figs. 18, 20, and 21, respectively. Considering Figs. 18(a), 20(a), and 21(a), it is seen that the height of the Al-K_α peak decreases, relative to the Fe-K_α peak, continuously from FBB-3 to FBB-12. The compositions of the Fe matrix and NiAl-type precipitate, evaluated by analyzing the EDS spectra using the procedure described in Section B.3.2, are listed in Tables X and XI, respectively.

As seen in Table X, the Al content in the Fe matrix decreases from 9.8 wt.% (18.6 at.%) in FBB-3 to 2.3 wt.% (4.7 at.%) in FBB-12, while the Cr-, Ni-, and Mo contents remain almost the same. Similalry, Table XI shows the compositions of NiAl-type precipitates in these alloys.

The Cr content in the NiAl-type precipitate is roughly 1.5 wt.%, while the Fe content varies from 15 to 18 wt.%, and the Mo content is almost negligible.

The experimental Al-Fe-Ni isothermal section at 1,023 K shows that NiAl dissolves about 18 at.% Fe at 1,023 K [106]. Therefore, our measured values of Fe in the NiAl-type precipitate is consistent with the phase diagram, as a lower Fe content in NiAl is expected due to a lower aging temperature of 973 K.

Comparing the data in Tables X and XI, it is clear that both Cr and Mo partition predominantly to the Fe matrix. In addition, concomitant with the decrease in the Al content in the Fe matrix, there is an increase in the Ni content in the NiAl-type precipitate. This trend is consistent with the expected tie-lines in the two-phase field (bcc + *B*2) in Al-Fe-Ni isothermal sections.

With the knowledge of the compositions of β and β′ phases, the volume fraction ($V_{\beta'}$) of the latter can be estimated, using the lever rule:

$$V_{\beta'} = \frac{C_0 - C_\beta}{C_{\beta'} - C_\beta} \tag{21}$$

where C_0, C_β, and $C_{\beta'}$ are the compositions of the alloy, β matrix, and β′ precipitate, respectively. Considering Al, Cr, and Ni, we obtain $V_{\beta'}$ = 0.179, 0.178, and 0.135 for FBB-3, FBB-8, and FBB-12, respectively. In the AEM composition analysis, we have neglected the ultrafine precipitates and considered only 25 EDX spectra of β and β′ phases. Further AEM data as well as atom-probe tomography (to include ultrafine precipitates) may be needed for the accurate estimation of $V_{\beta'}$.

B.3.4 Conclusions

The microstructures of FBB series alloys, in the as-quenched and heat-treated (973 K for 100 hrs) conditions, are carried out by recording BF and DF images, and SAD patterns in a

conventional TEM. The following conclusions are drawn:

(i) All alloys exhibit nucleation and growth of *B*2 (NiAl-Type) precipitates in the as-quenched state, and they undergo coarsening during subsequent aging at 973 K.

(ii) Both fully coherent (in FBB-1, -3, -4, -7, and -8) and semi-cohenrent (in FBB-2 and -12) B2 (NiAl-Type) precipitates are observed after aging at 973 K for 100 hrs.

(iii) In FBB-7 and FBB-8, the B2 domains exhibit the additional phase separation.

(iv) A preliminary analysis of the B2-precipitate size data demonstrate that Hf is more effective than Zr in improving the coarsening resistance.

(v) Minor phases, presumably carbides and borides and possibly other intermetallics, are also observed in the as-quenched and heat-treated alloys of FBB-2, FBB-3, and FBB-4. However, no attempt was made to characterize them.

To supplement the TEM studies of microstructures of prototype alloys, the AEM investigations are also carried out using thin foils of FBB-1, -2, -3, -7, -8, and -12 that are aged at 973 K for 100 hrs. Even though no attempt was made to quantify the EDX results of FBB-1, -2, and -7, several key information regarding the partitioning behavior of alloying elements in the matrix and NiAl-type precipitates is obtained in this AEM study. The following conclusions are drawn:

(i) Both Cr and Fe partition to NiAl-type precipitates.

(ii) The partitioning of Mo in the NiAl-type precipitate is barely detectable. Consequently, I(Mo)/I(Ni) ratios exhibit a large relative error (due to the poor X-ray counting statistics).

(iii) Neither the matrix nor NiAl-type precipitate spectra showed any evidence of Hf in FBB-2 and Zr in FBB-3 and -7. Therefore, in the future, further care or a new strategy is

needed while preparing prototype alloys containing small amounts Hf and/or Zr.

To relate the compositions of phases (the Fe matrix and NiAl-type precipitate) with mechanical properties, we have quantified the compositions in the matrix and the precipitate of model alloys FBB-3, FBB-8, and FBB-12, which were aged at 973 K for 100 hrs using the AEM techniques. An important result is that the Al content in the Fe matrix decreases significantly from FBB-3 to FBB-12, with a concomitant increase in the Ni content in the NiAl-type precipitate. The volume fraction of *B2* precipitate lies in the range of 13.5% ~ 17.9% for FBB-3, -8, and -12.

B.4 Mechanical Behavior

B.4.1 Introduction

Limited work in the literature has been performed on the mechanical behavior of Fe-Ni-Al-(Cr) systems at elevated temperatures. There is no systematic study of the ductility of these materials. Only recently, Stallybrass et al. [27] reported that the Fe-Ni-Al-Cr alloys with a high volume fraction (0.37) of β′ exhibited a bending ductility less than 1.5% even at temperatures higher than 1,273 K. The reason for the low ductility of these materials has not been fully understood. Nevertheless, the steam-turbine materials generally require a tensile ductility of about 10% at room temperature for sufficient workability in as-cast and subsequent fabrication stages.

The effects of various alloying elements on the ductility and toughness of the β phase have been reported in the literature [107-109]. Leslie ([107]; also references therein) has summarized the effect of many alloying elements on the strength, ductility, and toughness of the β-solid solution. Specifically, it has been established that Co, Ni, Rh, Ir, and Pt increase toughness (decrease the notch-impact transition temperature), while Si and P decrease toughness

(increase the notch-impact transition temperature) and also to a lesser extent by Cr, Mn, and Re. In this regard, Al behaves analogous to Si in the β solid solution. Recently, Herrmann et al. [109] reported the tensile strength and ductility of the Fe-(4 to 18)Al (atomic percent) solid solution at room temperature. With increasing the Al content, an increase in the strength and a concomitant decrease in the ductility were observed. Furthermore, α Fe is known to exhibit cleavage fracture, particularly at low temperatures, due to the limited number of active slip systems.

Pugh [110] proposed that the ductility of pure metals is related to the ratio of the bulk modulus to shear modulus (K/G). The rationale is that with decreasing K/G, more energy is stored as dilation rather than shear deformation. In fact, the measurement of polycrystalline elastic constants of β solid solutions show a marked increase in K/G when Ni and Pt are added to Fe, leading to an increase in the fracture toughness. On the other hand, K/G, slightly decreases when Cr and Mn are added, leading to a decrease in the fracture toughness. However, such a simplistic correlation fail in many cases [107]. A more fundamental hypothesis is that the elements, which increase ductility, also change bonding so as to increase the cross-slip of screw dislocations in the α Fe [107]. The polycrystalline NiAl with a B2 structure exhibits no tensile ductility at room temperature due to the lack of five independent slip systems to satisfy the Von Mises' criterion for the polycrystalline plasticity [111]. Like many bcc metals and B2 aluminides, NiAl exhibits cleavage fracture. However, the cleavage plane is not well defined [112,113]. It has been observed that in B2-NiAl, the fracture of {511} transient planes may proceed before cleavage on {110} planes [112,113]. Darolia et al. [114] reported that small additions of Fe, Ga, and Mo significantly improve the tensile ductility, but Fe is the most effective. For example, NiAl along <110> has a tensile ductility of only 0.8%, but with the addition of 0.25 at.% Fe (substituting for Al in NiAl), the tensile ductility increases to 5.9% [114]. In another study, Field

et al. [115] reported that the addition of Cr promotes the activation of the <111> slip system. Law and Rachinger et al. [116,117] suggested that Cr, Mn, and Fe lower the ordering energy of NiAl and favor <100> slip, but this argument was disputed by Cotton [118]. Small additions of Mo were also reported to increase the ductility of the polycrystalline NiAl at room temperature [119], while Hahn and Vedula [111] demonstrated that small deviations from the stoichiometric composition make NiAl even more brittle at low temperatures.

Based on the available literature, it is implicit that the dissolved Al in the β solid solution, and the volume fraction and stoichiometry of the NiAl precipitates are expected to be the major factors controlling the ductility of β/β′ alloys. To investigate these factors, we have carried out a systematic study. Specifically, six β/β′ (FBB) alloys with the nominal compositions of Fe-xAl-10Ni-10Cr-3.4Mo-0.25Zr-0.005B (x = 3 - 10 wt.%) were fabricated to investigate the effects of Al on the phase transformation, microstructure, and partitioning behavior of alloying elements, precipitate-volume fraction, and bending ductility at room temperature. An attempt was made to improve the ductility of the NiAl-strengthened ferritic steels by optimizing the Al concentration.

On the other hand, some research work on the tensile and creep behavior above 873 K has been performed in this ferritic-alloy system, in order to evaluate their applications at high temperatures. The yield stress as a function of temperature for Fe-Ni-Al-Cr alloys has been studied [120]. It is shown that the yield stress decreases dramatically above 873 K due to the dissolution of hyperfine cooling precipitates, and the value lies above conventional heat-resistant steels and below Ni-based superalloys. Creep properties have been examined by compressive and tensile creep tests in the stress range of 10 - 350 MPa and temperature range of 873 - 1,273 K [26,27,121-123]. Similar results have been reported that the stress exponent is determined to

be 4 with the compensation of the threshold stress on the order of Orowan stress, and the creep-activation energy is on the order of magnitude of the activation energy for self-diffusion in Fe. The steady-state creep rate is about 10^{-8} s^{-1} at a compressive stress level of 50 MPa and 1,023 K, in Fe-Al-Ni and Fe-Al-Ni-Cr alloys with a 20 ~ 24 % volume fractions of NiAl precipitates [27,121,122]. However, controversy exists on the observed creep mechanism. Jung [121-123] observed the diffusional creep at a low stress in Fe-Al-Ni alloys, which was not found in Fe-Al-Ni-Cr alloys with a comparable volume fraction in the same temperature and stress ranges. Jung suggested that the creep mechanism was grain-boundary sliding, accommodated by the dislocation creep within the grains at high stresses and by the diffusional creep at low stresses, while others claimed a dislocation-creep mechanism with a single slope of stress dependence [121,122]. Zhu et al. [26] investigated the dislocation-particle interactions of the crept Fe-Al-Ni-Cr alloys by TEM, and suggested that the operative deformation mechanism under low stresses was a dislocation local climb coupled with a weak attractive interaction between dislocations and particles. Stallybrass et al. [27,120] reported that the threshold stress increases with the volume fraction of precipitates and decreases rapidly with the increased temperature.

Further alloy optimization to improve the creep resistance in the ferritic superalloy requires a fundamental understanding of the composition-microstructure-property relationships. In particular, quantitative analyses of precipitation configurations are desired, since the creep behavior is largely dependent on the precipitate parameters through various dislocation-particle interactions (e.g., particle shearing, Orowan bowing, dislocation climb, and dislocation detachment) in the precipitation alloys. In the present work, prescreening in the creep properties of the designed ferritic alloys has been conducted by short-term compressive-creep tests. Detailed studies on the selected compositions with the optimal creep resistance have been

performed by tensile-creep tests. Using a power-law creep model, the stress and temperature dependence on the secondary creep rate and the threshold stress are determined. The creep mechanism during compressive creep has been identified as a mixture dislocation-particle interactions of Orowan bowing and dislocation climb.

B.4.2 Experimental Methods

B.4.2.1 Ductility

From the heat-treated rods, strips with a size of 19.05 x 3.17 x 0.76 mm for three-point-bending tests were cut by electron-discharge machining (EDM), and then tested at a strain rate of 2×10^{-4} s^{-1} at room temperature. The fracture surfaces were investigated by the scanning-electron microscopy (SEM) to identify the fracture mechanisms.

B.4.2.2 Creep

Compressive-creep specimens were cut from the ingot into cylinders with a 4-mm diameter and 6-mm height using EDM. Short-time compressive-creep tests were conducted to prescreen the creep property of different compositions, employing the Material Testing Systems (MTS) facility. A constant compressive load with an initial engineering stress level of 140 MPa was applied at 973 K for 100 hrs. The temperature variation is within 2K, as monitored by a thermocouple attached on the specimen. After the creep test, the sample was cooled in air. Prescreening of creep properties for FBB-1, -2, -3, and -4 were conducted in vacuum, while compressive-creep tests for the other alloys were performed in air.

For selected alloys with the optimal compressive-creep resistance, tensile-creep experiments were performed using dog-bone specimens through a dead-load creep frame. Compared to previous prescreening compressive-creep tests on samples with a small geometry (4 mm in diameter and 6 mm in height), tensile-creep tests with a larger specimen geometry could

reduce the errors caused by external environments. The steady-state creep rate, rupture time, and Larson-Miller parameter can be determined by tensile-creep tests, and, thus, those parameters can be compared with other ferritic steels, most of whose data are based on the tensile creep. The creep experiments were conducted in a constant dead-load creep frame. Each specimen is mounted in a testing fixture and suspended within the creep-frame furnace. A chromel-alumel thermocouple wired to the center of the specimen gauge length is connected to a digital temperature recorder which, in turn, is used to monitor the temperature of the specimen during testing, with ± 1 K variation during the constant temperature test. At the beginning of each test, the specimens are heated to the desired temperature and stabilized before any load is applied. Loading is in the uniaxial tension with a constant load throughout the test. In addition to the temperature, the specimen extension, measured by a dial gauge attached to the testing fixture, is also recorded as a function of time. The dog-bone specimen has a gauge length of 28 mm, a gauge diameter of 3.175 mm, and a total length of 47 mm.

Thin slices were cut perpendicular to the cylinder axis for compressive-crept samples and subsequently grounded to a thickness of ~ 50 micron. Foils for TEM characterizations were further prepared by electro polishing. An electrolyte containing 6 vol.% perchloric acid, 60 vol.% Methanol, 33.5 vol.% ethoxy-ethanol, and 0.5 vol.% glycerin in methanol is maintained at 243 to 253 K, and applied by a voltage of 16 V. Dislocation-particle interactions have been examined in an FEI Tecnai 20 microscope operating at 200 kV.

B.4.3 Results and Discussions

B.4.3.1 Three-Point-Bending Experiments and Fracture Behavior

Three-point-bending tests were performed to assess the ductility of model alloys. In this test, the bending flexural strain of a strip is calculated as [124]

$$\varepsilon_f = 6D't / L^2 \tag{22}$$

where ε_f is the strain on the outer surface, D′ is the maximum deflection at the center of the strip (mm), t is the thickness (mm), and L is the support span (mm). The calculated bending ductility and measured hardness are shown in Fig. 22. Reducing the Al concentration from 10 wt.% to 3 wt.% improves the failure bending strain from 0.5% to more than 5%. The hardness decreases slightly, when the Al content is reduced from 10 wt.% to 6.5 wt.% below which the hardness drops significantly.

The SEM fractographs of FBB-3, FBB-8, and FBB-9 are shown in Figs. 23(a)-(c). The flat facets in all cases exhibit river patterns, which are the characteristic feature of a brittle cleavage fracture. The sharp drop in the hardness and a concomitant increase in the ductility from FBB-12 (4 wt.% Al) to FBB-13 (3 wt.% Al) suggest a possible change of fracture modes. Figure 23(d) shows the bending fracture surface of the alloy FBB-13. It exhibits a mixed fracture mode of cleavage and ductility. The representative ductile fracture is shown as an inset in Fig. 23(d).

Following the brief discussion in Introduction, it is implicit that many properties of β/β′ alloys are expected to be governed by the intrinsic properties of the constituent phases. Specifically, the bulk NiAl exhibits only a limited ductility, and that of the α Fe is strongly influenced by alloying elements, such as Al. In addition, it has been reported that the ductility of the polycrystalline alloys decreases, as the volume fraction of the strengthening particles increases [125].

Our TEM and AEM studies show that the microstructures of model alloys consist of the β matrix and spherical/cuboidal β′ strengthening precipitates. In this class of alloys, we find that two major factors governing the ductility: viz. the volume fraction of β′ and the Al content in the

α-Fe matrix. In model alloys containing 4 - 10 wt.% Al, the volume fraction of β′ lies in the range of 0.13 - 0.18. When the Al content is reduced while keeping the Ni content the same, three microstructural changes take place simultaneously: (1) the volume fraction of β′ decreases, (2) the Al content in the β matrix decreases, and (3) the Ni content in the β matrix slightly increases. It is believed that the improvement in the ductility for FBB-13 is related to the decrease in both the precipitate volume fraction and Al solubility in Fe. However, among these two factors, which one is decisive to the ductility is not clear at this stage, as both of them change when increasing the Al additions. To understand each of their individual effects, we need to control one of those factors at a constant value while changing the other. In the future, alloys will be fabricated according to the thermodynamic-calculation results and investigate the individual effects of each factor.

Although the volume fraction of β′ decreases moderately from FBB-3 to FBB-12, the Al content in the β matrix decreases significantly from 18.6 at.% in FBB-3 to 4.7 at.% in FBB-12. In their study, Herrmann et al. [109] reported that the presence of DO_3-type chemical order may also lower the ductility of Fe-Al alloys. However, in our model alloys, the presence of DO_3-type could not be seen in TEM diffraction patterns. Thus, its influence on ductility is ruled out. Among other alloying elements in the β matrix, dissolved Cr and Mo may also cause a decrease in the ductility and toughness of Fe [107]. Nevertheless, this trend cannot explain the ductility differences for FBB-3 to FBB-12 alloys, as AEM results reveal that the amount of the dissolved Cr and Mo in the β matrix are almost the same. In addition, AEM results reveal that the Al- and Ni-contents in the β matrix have decreased and increased, respectively, from FBB-3 to FBB-12. Therefore, both these factors have contributed to the improvement in the ductility of FBB-12.

Several studies [113,114,126] have shown that the dissolved Fe modifies the preferred

slip vector of the polycrystalline NiAl, and thus improves the ductility. Also, Kovalev et al's study [127] found that the addition of 2 at.% Fe decreases the ductile-brittle transition temperature of NiAl by about 473 K. Our AEM results show that the Fe content in β′ precipitates varies from 15.3 at.% in FBB-3 to 18.1 at.% in FBB-8, which indicates that the softening effects in FBB-8 may be higher than in FBB-3. The AEM results also reveal that the chemistry of the β′ has changed from Al-rich in FBB-3 to slightly Ni-rich in FBB-12 due to a reduction in the Al content in the alloy. It has already been shown [117] that a small deviation from the stoichiometric composition makes NiAl even more brittle at low temperatures. Due to the insignificant partitioning of Cr and Mo to β′, the ductility of the β′ precipitates in FBB-8 should be the highest. However, the ductility of all model alloys with the Al content higher than 4 wt.% is nearly the same, implying the intrinsic ductility of the β′ precipitates is nearly constant. Therefore, the two major factors governing the poor ductility of the β′-strengthened ferritic steels are the volume fraction of NiAl-type precipitates and the Al content in the α-Fe matrix.

Although the ductility of β′-strengthened ferritic steels can be improved by reducing the Al content, concomitantly the hardness decreases, as shown in Fig. 22. This trend is due to the decrease in the volume fraction of β′, and also due to the decrease in the solid-solution strengthening of the β matrix, as the dissolved Al is reduced. A major objective of this research is to design a creep-resistant ferritic steel with a decent ductility at room temperature for sufficient fabricability. A certain amount of Al is needed for the formation of sufficient β′ precipitates for both creep and oxidation resistance. Combining the ductility and hardness of the model alloys shown in Fig. 22, an optimal balance appears to be at about 6.5 wt.% Al. The tensile ductility of the alloy with 6.5% Al can be further improved to more than 10 wt.% by thermal-mechanical treatments, which will be discussed elsewhere [128].

B.4.3.2 Compressive and Tensile Creep Behavior

The strain (ε) vs. time (t) curves for FBB-1, -2, -3, and -4 at 973 K and 160 MPa in vacuum for 1 hr are plotted in Figure 24. The alloy FBB-1 shows a typical creep curve. During the primary creep stage, the creep rate is very large and decreases very quickly. Then, the creep rate becomes constant, and creep goes into the steady-state stage. The tertiary stage doesn't appear within 1 hr. However, the alloys FBB-2, FBB-3, and FBB-4 exhibit a different creep behavior. There is no obvious primary creep. The creep goes into a steady-state stage directly. Similarly, no tertiary stage appears within 1 hr. Among FBB-2, FBB-3, and FBB-4 alloys, FBB-3 exhibits the lowest strain after one hr. Alloys with the same wt.% of Zr (FBB-3) appear to have a better creep resistance than alloys with Hf (FBB-2), as shown in Figure 24. Therefore, FBB-3 was selected as the base alloy for further creep improvement.

Figure 25 shows the typical creep curves of strain vs. time for the alloys FBB-3, -7, -8, -9, -12, and -13 with different Al concentrations. The primary creep stage, where the strain rate decreases as a function of time, is very transient in all the alloys except FBB-12, before the material steps into the secondary-creep stage where the strain rate is approximately constant. Either secondary or tertiary creep was achieved during the 100-hrs tests. The regime of the secondary creep is relatively shorter in the alloys FBB-3 and -7 than the other alloys, indicating that microstructure instabilities (e.g., coarsening of precipitates, grain growth, and/or change of dislocation structures) occurred during the steady-state creep and accelerated the onset of the tertiary creep. Steady-state creep rates at 973 K and 140 MPa are plotted in Fig. 26 as a function of the Al addition. The total variation in the creep rates was nearly two orders of magnitudes ($10^{-9} \sim 10^{-7}$ /s). Optimal compositions with minimal secondary creep rates were exhibited by the

alloys with ~ 6.5 wt.% Al (FBB-8). Stallybrass et al. [27] measured the compressive steady-state creep rates to be in the range of 7.2 x 10^{-5} ~ 2.8 x 10^{-6} /s at 973 K and 140 MPa for the Fe-Ni-Al-Cr alloys with 9 ~ 37 % volume fractions (vol.%) of precipitates. Compared to his results, FBB alloys show 1 ~ 3 orders of magnitude lower creep rates with less than 20 vol.% of precipitates. Such incredible improvement in the creep resistance is probably attributed to the addition of Mo as a solid-solution strengthening element in the Fe matrix. The mobility of dislocations is reduced by moving viscously and dragging the solute atmosphere [129]. The minimal creep rates in the solid-solution Fe-Mo were reported to be approximately three orders of magnitude lower than that in α Fe [130].

Figure 26 presents the steady-state creep rates, average particle diameter, and precipitate volume fraction as a function of the Al concentration. With Al increases, the average particle size decreases. The precipitate volume fractions in FBB-3, -8, and -12 have been determined to be 17.9%, 17.8%, and 13.5%, respectively, by AEM analyses, as reported in Section B.3. The volume fraction of precipitates in FBB-13 has been estimated to be ~ 7% by a thermodynamic model [131]. It can be concluded that the volume fraction increases, as Al increases to 6.5 wt.% and saturates with a further addition of Al.

The relationship between microstructural parameters and creep properties are revealed by clarifying the underlying creep mechanisms. Figure 27 presents a typical feature of dislocation-particle interactions examined by TEM, which reveals the existence of two types of strengthening mechanisms: dislocation loops bowing out between particles and dislocation climb around particles. Both mechanisms can introduce a threshold stress or back stress to resist the dislocation motions. Particle shearing was not observed probably due to the coarse size of precipitates. The results are consistent with Zhu et al's investigation [26]. The threshold stress

could equal the Orowan stress, or a ratio of the Orowan stress for the dislocation climb (e.g., 0.4 ~ 0.7 for the local climb and 0.004 ~ 0.02 for the general climb mechanisms [132,133]). The Orowan stress can be calculated from the following expression [134]:

$$\sigma_{OR} = \frac{0.81Gb}{\pi\lambda_s(1-\nu)^{1/2}} \ln\left(\frac{1.63r}{b}\right) \tag{23}$$

$$\lambda_s = 0.82 \times \left[\left(\frac{\pi}{f}\right)^{1/2} - 2\right] r \tag{24}$$

where λ_s is the square lattice spacing, r is the particle radius, f is the volume fraction, and ν is the Poisson's Ratio. Using 42 GPa as the shear modulus of Fe at 973 K, ν of 0.33, b of 0.20269 nm, and r determined by TEM, we estimate the Orowan stress for FBB-3, -8, and -12 to be 190, 143, and 105 MPa, respectively. Assuming that the same mechanism (either dislocation local climb or Orowan bowing) is dominant in the alloys with Al ranging from 3 wt.% to 6.5 wt.%, the increased volume fraction probably leads to a higher creep threshold stress, and, thus, largely improves the creep resistance. However, such correlation is not valid for alloys with Al > 6.5 wt.%. It is possible that the predominant mechanism changes from the Orowan bowing to local climb or from local climb to general climb at Al > 6.5 wt.%, leading to the reduced values of the threshold stress and as the increased creep rates for FBB-7 and -3. Although FBB-8 and -3 have the same volume fraction, the Al concentration in the matrix is much higher (18.6 at.%) in FBB-3 than that (8.2 at.%) in FBB-8, while the Fe concentration in the matrix is 10.4 at.% lower in FBB-3 than in FBB-8 (see Tables X and XI). The compositions of other elements in the matrix and elements in the precipitate are similar in the two alloys. Therefore, the accelerated creep rates in the range of 6.5 ~ 10 wt.% Al is probably associated with the high Al concentration in the matrix or the change of dislocation-particle interaction mechanisms.

The effect of Zr on the creep property was also studied. As shown in Figure 28, additional Zr in FBB-14 does not show an apparent improvement on the steady-state creep rate, at the compressive stress level of 140 MPa.

As a conclusion of the prescreening compressive-creep experiments, the optimal composition with both good creep resistance and ductility has been determined to be FBB-8. To further improve the creep resistance, the solid-solution element, W, was added into FBB-8 to design the alloys, FBB-8W1 and FBB-8W2, considering that W can strengthen the matrix and reduce the creep rate dramatically. The tensile-creep tests for FBB-8, -8W1, and -8W2 have been conducted, using dead-load creep frames by constant-load stress-jump tests at 973 K from engineering stresses of 60 ~ 140 MPa. The stress transition was taken after the steady-state creep rate was obtained for the previous level of stress. A well-established steady-state creep regime was observed for both the alloys at the studied stress levels. The dependence of the secondary creep rate at 973 K on the true stress for the alloys is plotted on a logarithmic scale in Figure 29(a). The data points exhibit an apparent single-slope behavior. From the slope of the straight line, the apparent-stress exponent can be determined. A strong stress dependence was observed with the high apparent-stress exponent in the range of 6.8 ~ 9.9, which is commonly found in particle-strenghened materials. With the addition of W, the secondary creep rates of FBB-8W1 and 8W2 are reduced by 1 ~ 2 orders of magnitudes, compared to FBB-8.

The stress dependence of the secondary creep rate of particle-strengthened materials can usually be described by a phenomenological equation involving a threshold-stress compensation, given by

$$\dot{\varepsilon} = A(\sigma - \sigma_{th})^n \exp\left(-\frac{Q}{RT}\right) \tag{25}$$

where $\dot{\varepsilon}$ is the steady-state creep rate, A is the constant, σ is the applied stress, σ_{th} is the

threshold stress, n is the stress exponent, Q is the activation energy, R is the gas constant, and T is the temperature. A linear fit was obtained by plotting the $\dot{\varepsilon}^{1/n}$ against the stress in Figure 29(b). A good fit was achieved with a value of n = 4, which was also observed by Zhu et al. [26] and Stallybrass et al. [27]. The threshold stress can be estimated by extrapolating the stress at $\dot{\varepsilon}^{1/n}$ = 0. Therefore, the relationships between the stress and strain rate are described as

$$\text{FBB-8:}\quad \dot{\varepsilon} = 4.28\times10^{-14}\times(\sigma - 44.6)^4 \tag{26}$$

$$\text{FBB-8W1:}\quad \dot{\varepsilon} = 2.16\times10^{-15}\times(\sigma - 53.5)^4 \tag{27}$$

$$\text{FBB-8W2:}\quad \dot{\varepsilon} = 3.84\times10^{-16}\times(\sigma - 40)^4 \tag{28}$$

The threshold stresses for FBB-8, -8W1, and -8W2 at 973 K are determined to be 44.6, 53.5, and 40 MPa, respectively. Note that the threshold stress of FBB-8W2 is lower than that of FBB-8 (44.6 MPa) and FBB-17 (58.8 MPa). A similar threshold stress and much lower secondary creep rate are observed for FBB-8W2, compared with FBB-8. The possible reason is twofold: (1) a W-intermetallic phase forms inside the material, which enhances the strength of the material at elevated temperatures, and (2) W provides significant solid-solution strengthening in the Fe matrix to reduce the steady-state creep rate.

Figure 30 compares the Larson-Miller parameter (LMP) of FBB-8 with the other Fe-based materials candidates for steam-turbine applications [135]. FBB-8 does not show the superior creep resistance, relative to the other candidates at high stresses (> 100 MPa). However, considering the application stress for steam turbines is only 35 MPa, the creep resistance of FBB-8 is comparable with the other candidate materials at 80 MPa, and higher than most materials except HR-1200 at 60 MPa.

B.4.4 Conclusions

The DSC results show a transition peak between the transformation temperatures of β′

to β in the alloys with low Al contents. The AEM analyses verify that this transformation is most likely to be the FeAl phase separation inside the β′ (NiAl) precipitates. The TEM study exhibits that the microstructure of the model alloys consists of the β-Fe matrix and β′ (NiAl-type) precipitates with a diameter between 130 and 150 nm. The volume fraction of β′ lies in the range of 0.07 - 0.18 for the studied alloys.

The three-point-bending test reveals that the model alloys, containing 4 ~ 10 wt.% Al, exhibit very limited ductility (< 2%) at room temperature, and their fracture mode is predominantly of a cleavage type. Two major factors governing the poor ductility are the volume fraction of NiAl-type precipitates and the Al content in the α-Fe matrix. Among these two factors, it is necessary to undertake further studies with alloys along a particular tie-line by keeping the volume fraction of β′ constant but varying the Al content. This approach may help establish the dominance of either of these two factors. A bending ductility of more than 5% can be achieved by lowering the Al concentration in alloys to 3 wt.%. However, the alloy containing about 6.5 wt.% Al is found to have an optimal combination of hardness and ductility.

From prescreening compressive-creep tests, we have determined that the optimal compositions with the superior creep resistance contain ~ 6.5 wt.% Al. Orowan bowing and dislocation climb were identified to be dislocation-particle interaction mechanisms. Steady-state creep rates decreased in the region of 4 ~ 6.5 wt.% Al due to an increased volume fraction of precipitates and the enhanced resistance to the dislocation motion. Accelerated creep rates were found in the region of 6.5 ~ 10 wt.% Al, associated with a high Al concentration in the matrix or change of dislocation-particle interaction mechanisms.

The tensile-creep experiments by stepwise loading have been performed for FBB-8, -8W1, and -8W2. With the threshold-stress compensation, the stress exponent is determined to be

4, indicating the power-law creep. The threshold stress is in the range of 40 ~ 53 MPa. An addition of W can significantly reduce the secondary creep rates. Compared to other candidates for steam-turbine applications, FBB-8 does not show superior creep resistance at high stresses (> 100 MPa), but exhibit superior creep resistance at low stresses (< 60 MPa).

C. DEVELOPED PRODUCTS AND TECHNOLOGY-TRANSFER ACTIVITIES

C.1 Publications

- S. Huang, D.L. Worthington, M. Asta, V. Ozolins, G. Ghosh, and P.K. Liaw, "Calculation of Impurity Diffusivities in α-Fe Using First-Principles Methods," Acta Mater., 2010;58:1982.
- Z. K. Teng, M. K. Miller, G. Ghosh, C. T. Liu, S. Huang, K. F. Russell, M. E. Fine, and . Liaw, "Characterization of nanoscale NiAl-type precipitates in a ferritic steel by electron microscopy and atom probe tomography," Scripta Mater., 2010;63:61.
- Z. K. Teng, C. T. Liu, G. Ghosh, P. K. Liaw, and M. E. Fine, "Effects of Al on the microstructure and ductility of NiAl-strengthened ferritic steels at room temperature," Intermetallics, 2010;18:1437.
- Z. K. Teng, C. T. Liu, M. K. Miller, G. Ghosh, E. Kenik, S. Huang, and P. K. Liaw, "Room temperature ductility of NiAl-strengthened ferritic steels: effects of precipitate microstructure and hot rolling," 2010, in preparation.
- Z. K. Teng, F. Zhang, M. K. Miller, S. Huang, Y. T. Chou, R. H. Tien, C. T. Liu, Y. A. Chang, and P. K. Liaw, "New ferritic steels with combined optimum creep resistance and ductility designed by coupling thermodynamic calculations with focused experiments," 2010, in preparation.
- S. Huang, X. Li, G. Ghosh, E. A. Kenik, J. Ilavsky, Z. Teng, G. Wang, M. E. Fine, C. T. Liu, L. Liu, and P. K. Liaw, "Study of the nanoscale (Ni,Fe)Al precipitates in the ferritic superalloy by ultra-small-angle X-ray scattering," 2010, in preparation.
- S. Huang, E. A. Kenik, J. Ilavsky, G. Ghosh, Z. Teng, G. Wang, M. E. Fine, C. T. Liu, and P. K. Liaw, "Effects of Al on the creep behavior and microstructure of a ferritic superalloy strengthened by NiAl precipitates," 2010, in preparation.

C.2 Presentations

- P. K. Liaw, C. T. Liu, G. Ghosh, M. E. Fine, M. Asta, M. K. Miller, S. Huang, Z. K. Teng, and G. Y. Wang, "Computational design and prototype evaluation of aluminide-strengthened ferritic superalloys for power-generating turbine applications up to 1,033 K," International Conference on Advanced High-Temperature and High-Strength Structural Materials (HTHSSM), Hong Kong, Oct. 4-8, 2009.

- S. Huang, D. L. Worthington, M. Asta, V. Ozolins, G. Ghosh, and P. K. Liaw, "First-principles calculation on impurity diffusivities in ferritic iron," The TMS 138th Annual Meeting & Exhibition, San Francisco, CA, Feb. 15-19, 2009.
- Z. K. Teng, P. K. Liaw, C. T. Liu, G. Ghosh, M. E. Fine, S. Y. Huang, and G. Y. Wang, "Ductility of NiAl-strengthened ferritic superalloys at room temperature," The TMS 138th Annual Meeting & Exhibition, San Francisco, CA, Feb. 15-19, 2009.
- Z. K. Teng, C. T. Liu, M. K. Miller, G. Ghosh, E. Kenik, S. Huang, and P. K. Liaw, "Room temperature ductility of NiAl-strengthened ferritic steels: effects of precipitate microstructure and hot rolling," The TMS 139th Annual Meeting & Exhibition, Seattle, WA, Feb. 14-18, 2010.
- S. Huang, X. Li, G. Ghosh, E. A. Kenik, J. Ilavsky, Z. K. Teng, G. Wang, M. E. Fine, C. T. Liu, L. Liu, and P. K. Liaw, "Investigation of the nanoscale NiAl precipitates in the ferritic superalloy by USAXS," The TMS 139th Annual Meeting & Exhibition, February, Seattle, WA, Feb. 14-18, 2010.

C.3 Awards

- Z. K. Teng, 1st and 2nd Place Awards, Annual Sigma Xi Student Presentation Competition, The University of Tennessee, Knoxville, April 16, 2009 and March 23, 2010.
- Z. K. Teng, 1st Place Award, Oak Ridge Chapter of the 2009 ASM International Educational Symposium Student Poster Competition, April 22, 2009.
- Z. K. Teng, Winner of the 2010 TMS Annual Student Poster Contest in Structural Materials Division, The TMS 139th Annual Meeting & Exhibition, Seattle, WA, Feb. 14-18, 2010.
- S. Huang, 2nd and 1st Place Awards, Annual Sigma Xi Student Presentation Competition, The University of Tennessee, Knoxville, April 16, 2009 and March 23, 2010.
- S. Huang, 2nd Place Award, Student Research Poster Presentation, Oak Ridge Chapter of ASM International, Nov. 19, 2009.
- S. Huang, 3rd Place Award, Oak Ridge Chapter of the 2009 ASM International Educational Symposium Student Poster Competition, April 22, 2009.

- M. E. Fine, University of Minnesota Alumni Outstanding Achievement Award, 2010.
- P. K. Liaw, L. R. Hesler Award, The University of Tennessee, 2010.

C.4 Networks and Collaborations

- Oak Ridge National Laboratory: M. K. Miller and E. A. Kenik.
- University of California, Los Angeles: V. Ozolins.

D. GRAPHICAL MATERIALS LISTS

Table I: Calculated energetics for self- and impurity-diffusion in the bcc Fe. Vacancy-formation energies (ΔH_v^f), migration energies (ΔH_v^{mig}), and solute-binding energies (ΔH_b) are calculated in the fully-ordered ferromagnetic state and used to compute the corresponding value of the diffusion-activation energy (Q_0^F). The variable, α, parameterizes the dependence of the activation energy on magnetization - the values for Fe, W, and Mo are taken from the experimental measurements [54,72], while the values for Ta and Hf have been estimated from first-principles calculations of the induced magnetization, as discussed in the text. The activation energy in the paramagnetic state (Q^P) is derived as $Q^P = Q_0^F/(1+\alpha)$.

	Fe	W	Mo	Ta	Hf
ΔH_v^f (eV)	2.23	-	-	-	-
ΔH_b (eV)	-	-0.14	-0.17	-0.32	-0.65
ΔH_v^{mig} (eV)	0.64	0.71	0.54	0.44	0.18
α	0.156	0.086	0.074	0.057	0.047
Q_0^F (eV)	2.87	2.80	2.60	2.35	1.75
Q^P (eV)	2.48	2.58	2.42	2.22	1.67

Table II: Correlation factors (f_2) for Mo- and W-solute diffusion at representative temperatures of 800, 1,000, and 1,200 K. The results are calculated within the Le Claire formalism using first-principles-calculated migration energies, as discussed in the text. The calculated value of f_2, as well as the ratio of f_2 to the constant value of the correlation factor for the bcc Fe self-diffusion ($f_0 = 0.727$), is listed for each solute.

	W		Mo	
T (K)	f_2	f_2/f_0	f_2	f_2/f_0
800	0.77	1.06	0.22	0.30
1,000	0.74	1.02	0.28	0.39
1,200	0.73	1.00	0.33	0.46

Table III: Activation energies in the fully-ordered ferromagnetic state (Q_0^F) and paramagnetic state (Q^P) are listed, along with diffusion prefactors for self diffusion in the bcc Fe. Results obtained from the present calculations are compared with the available published experimental measurements. The calculated prefactors in this work are weakly temperature dependent, and the result listed in this Table and Tables IV and V correspond to T = 1,050 K.

	Q_0^F (kJ/mol)	Q^P (kJ/mol)	D_0 (m^2/s)
Present work	277	239	6.7×10^{-5}
Iijima et al. [54]	289.7 ± 5.1	250.6 ± 3.8	2.8×10^{-4}
Borg et al. [56]	-	281.5	1.2×10^{-2}
Geise et al. [55]	-	281.6	1.2×10^{-2}
Graham et al. [33]	-	239.7	2.0×10^{-4}
Walter et al. [59]	-	240.6	2.0×10^{-4}
Buffington et al. [57]	-	239.3	1.9×10^{-4}
Hettich et al. [58]	283.7	-	1.0×10^{-4}
James et al. [34]	254.0	240.6	2.0×10^{-4}
Lübbehusen et al. [60]	284.7 - 299.1	248.0 - 258.6	$6.8 - 12.3 \times 10^{-4}$
Kucera et al. [61]	-	261.5	1.1×10^{-3}

Table IV: Activation energies in the fully-ordered ferromagnetic state (Q_0^F) and paramagnetic state (Q^P) are listed, along with diffusion prefactors for impurity diffusion of W in the bcc Fe. Results obtained from the present calculations are compared with the available published experimental measurements.

	Q_0^F (kJ/mol)	Q^P (kJ/mol)	D_0 (m^2/s)
Present work	270	249	1.4×10^{-4}
Takemoto et al. [52]	312.0 ± 27.0	287.0 ± 22.0	1.5×10^{-2}
Kucera et al. [63]	-	246.2 ± 3.2	2.0×10^{-4}
Gruzin et al. [47]		292.9	3.8×10^{-1}
Alberry et al. [64]	-	243.5 ± 7.1	1.6×10^{-4}
Keiszniewski et al.[62]	-	265.7	6.9×10^{-3}

Table V: Activation energies in the fully-ordered ferromagnetic state (Q_0^F) and paramagnetic state (Q^P) are listed, along with diffusion prefactors for impurity diffusion of Mo in the bcc Fe. Results obtained from the present calculations are compared with the available published experimental measurements.

	Q_0^F (kJ/mol)	Q^P (kJ/mol)	D_0 (m^2/s)
Present work	251	234	6.3×10^{-5}
Nitta et al. [53]	-	282.6 ± 6.4	1.5×10^{-2}
Kucera et al. [63]	-	216.3	5.7×10^{-5}
Alberry et al. [64]	-	225.5 ± 4.6	7.9×10^{-5}
Borisov et al. [65]	-	205.0	3.0×10^{-5}
Nohara et al. [66]	284.5 ± 6.7	272.8 ± 5.4	3.1×10^{-3}

Table VI: FBB Alloy compositions (wt.%)

Alloys	Purpose	Fe	Al	Cr	Ni	Mo	W	Hf	Zr	B	Nb	V	C
FBB-1	Base	70	10	10	10	-	-	-	-	-	-	-	-
FBB-2	Hf	66.3	10	10	10	3.4	-	0.25	-	0.005	-	-	-
FBB-3	Zr	66.3	10	10	10	3.4	-	-	0.25	0.005	-	-	
FBB-4	Carbides	66.1	10	10	10	3.4	-	-	0.25	0.005	0.1	0.1	0.05
FBB-7	Al effect	68.3	8	10	10	3.4	-	-	0.25	0.005	-	-	-
FBB-8	Al effect	69.8	6.5	10	10	3.4	-	-	0.25	0.005	-	-	-
FBB-9	Al effect	71.3	5	10	10	3.4	-	-	0.25	0.005	-	-	-
FBB-12	Al effect	72.3	4	10	10	3.4	-	-	0.25	0.005	-	-	-
FBB-13	Al effect	73.3	3	10	10	3.4	-	-	0.25	0.005	-	-	-
FBB-17	Al effect	70.3	6	10	10	3.4	-	-	0.25	0.005	-	-	-
FBB-8W1	W effect	67.8	6.3	9.7	9.7		6.3	-	0.23	0.005	-	-	-
FBB-8W2	W effect	68.8	6.4	9.8	9.8	1.7	3.2	-	0.24	0.005	-	-	-
FBB-14	Zr effect	69.6	6.5	10	10	3.4	-	-	0.5	0.005	-	-	-
FBB-15	Zr effect	69.1	6.5	10	10	3.4	-	-	1	0.005	-	-	-

Table VII: Precipitate-size data [mean diameter (D) ± std deviation in nm] based on the measurements of 20 *B*2 particles in each specimen. As a relative measure of the coarsening resistance in these alloys, also listed are V_{973}/V_{AQ} [= $(D_{973}/D_{AQ})^3$], and the ratios of the mean volumes of precipitates after aging (V_{973}) and in the as-quenched (V_{AQ}) conditions.

Alloy#	As-quenched	973 K/100 hrs	(V_{973}/V_{AQ})
FBB-1	15 ± 3.1	5.7 ± 20.5	260
FBB-2	24.4 ± 4.5	1.8 ± 31	53
FBB-3	22.8 ± 3.5	3.3 ± 22.1	69
FBB-4	20.5 ± 4.3	00.3 ± 26.5	117
FBB-7	95 ± 22	05 ± 25	1.35
FBB-8	100 ± 18	130 ± 25	2.2

Table VIII: Ratios of integrated X-ray intensities of alloying elements in the Fe-based matrix based on the EDX spectra collected from thin foils in AEM.

Alloy#	Matrix				
	I(Al)/I(Fe)	I(Cr)/I(Fe)	I(Ni)/I(Fe)	I(Mo)/I(Fe)	I(W)/I(Fe)
FBB-1	0.125 ± 0.008	0.186 ± 0.008	0.032 ± 0.005	------	------
FBB-2	0.156 ± 0.010	0.177 ± 0.008	0.033 ± 0.008	0.017 ± 0.003	------
FBB-7	0.108 ± 0.008	0.170 ± 0.007	0.022 ± 0.006	0.017 ± 0.002	------

Table IX: Ratios of integrated X-ray intensities of alloying elements in NiAl-type precipitates based on the EDX spectra collected from thin foils in AEM.

Alloy#	Precipitate I(Al)/I(Ni)	I(Cr)/I(Ni)	I(Fe)/I(Ni)	I(Mo)/I(Ni)
FBB-1	0.779 ± 0.039	0.049 ± 0.005	0.414 ± 0.024	------
FBB-2	0.746 ± 0.062	0.028 ± 0.005	0.298 ± 0.022	0.003 ± 0.002
FBB-7	0.805 ± 0.039	0.024 ± 0.009	0.269 ± 0.049	0.003 ± 0.002

Table X: Compositions [**wt. fr.** (at. fr.)] of the Fe matrix in FBB alloys, aged at 973 K for 100 hrs, as determined using thin foils in AEM.

Alloy#	Fe-matrix Al	Cr	Ni	Mo	Fe
FBB-3	**0.098 ± 0.003** (0.186 ± 0.005)	**0.118 ± 0.009** (0.116 ± 0.009)	**0.023 ± 0.002** (0.020 ± 0.002)	**0.048 ± 0.009** (0.026 ± 0.005)	**0.713 (bal.)** (0.653)
FBB-8	**0.041 ± 0.001** (0.082 ± 0.002)	**0.115 ± 0.009** (0.119 ± 0.009)	**0.023 ± 0.002** (0.021 ± 0.002)	**0.037 ± 0.007** (0.021 ± 0.004)	**0.784 (bal.)** (0.757)
FBB-12	**0.023 ± 0.001** (0.047 ± 0.002)	**0.109 ± 0.009** (0.115 ± 0.01)	**0.035 ± 0.003** (0.033 ± 0.003)	**0.037 ± 0.007** (0.021 ± 0.004)	**0.796 (bal.)** (0.784)

Table XI: Compositions [**wt. fr.** (at. fr.)] of NiAl-type (*B*2) precipitates in FBB alloys, aged at 973 K for 100 hrs, as determined using thin foils in AEM.

Alloy#	NiAl-type precipitate Al	Cr	Fe	Mo	Ni
FBB-3	**0.302 ± 0.008** (0.482 ± 0.009)	**0.013 ± 0.001** (0.011 ± 0.001)	**0.153 ± 0.013** (0.118 ± 0.002)	**0.006 ± 0.001** (0.003 ± 0.0004)	**0.527 (bal.)** (0.386)
FBB-8	**0.274 ± 0.007** (0.448 ± 0.01)	**0.018 ± 0.002** (0.015 ± 0.002)	**0.181 ± 0.016** (0.143 ± 0.012)	**0.005 ± 0.001** (0.002 ± 0.0008)	**0.522 (bal.)** (0.392)
FBB-12	**0.248 ± 0.007** (0.415 ± 0.01)	**0.012 ± 0.001** (0.011 ± 0.0003)	**0.169 ± 0.015** (0.136 ± 0.012)	**0.003 ± 0.001** (0.001 ± 0.0009)	**0.569 (bal)** (0.437)

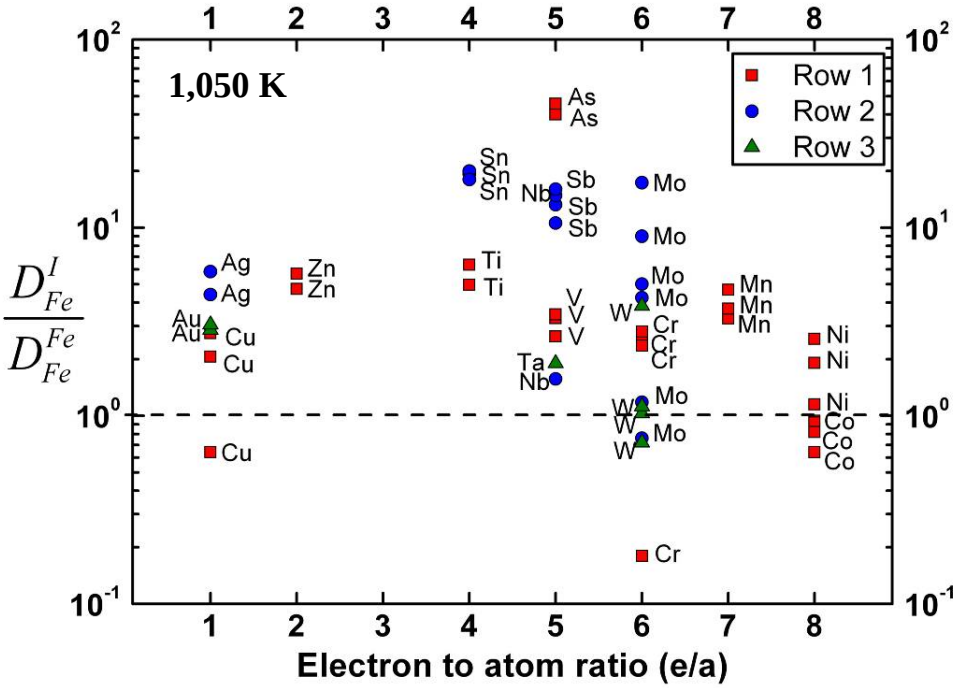

Figure 1 Ratios of diffusivities for impurity diffusion relative to self-diffusion in the α Fe plotted for a variety of solutes as a function of electron to atom ratio. The results correspond to a temperature of T = 1,050 K and are obtained from the published measurements [30-66]. Rows 1, 2, and 3 in the legend refer to the position of the element in the periodic table, corresponding to 3d, 4d, and 5d TM elements, respectively.

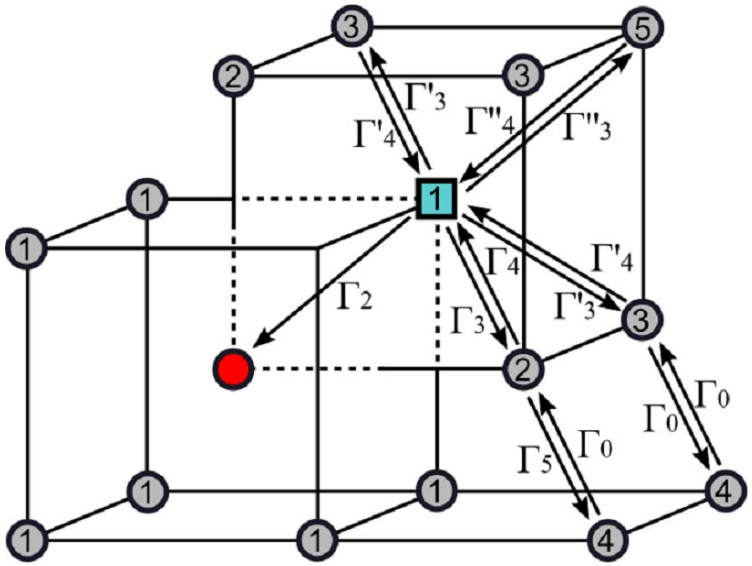

Figure 2 Illustration of the nine distinct jump frequencies considered in the calculation of the correlation factor for impurity diffusion [67,75]. The solute impurity is denoted by the red circle, the vacancy by the green square, and the solvent (Fe) atoms by grey circles. The numbers in the circles and squares correspond to the neighboring sites of the solute atom. Figure adapted from Philibert [75].

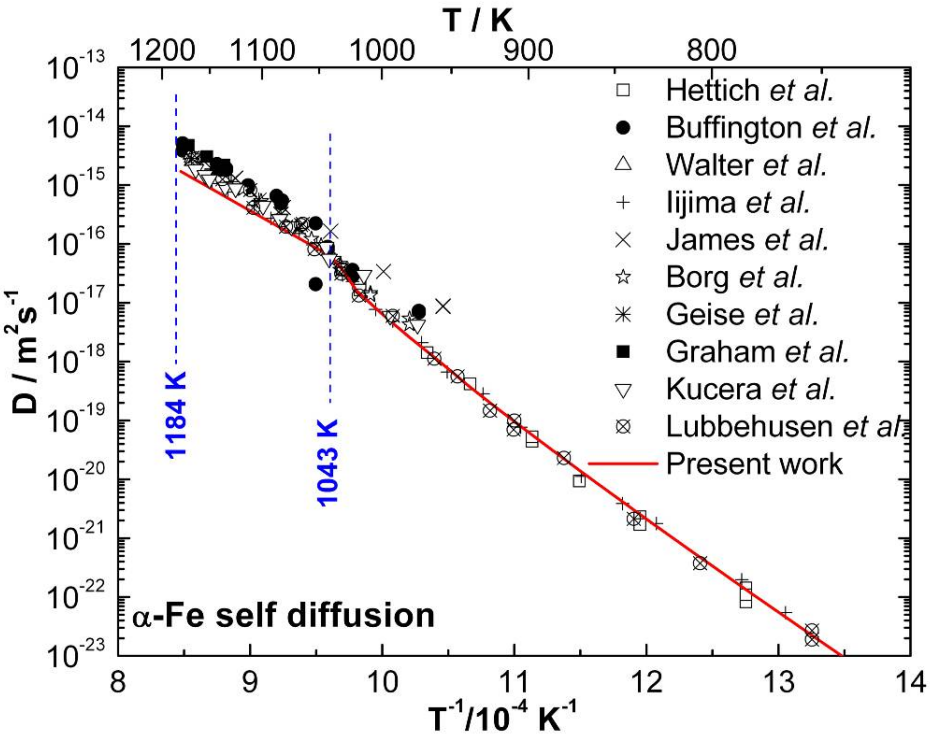

Figure 3 Predicted temperature dependence of the calculated α-Fe self-diffusion coefficients (red line) versus published experimental data [33,34,54-61].

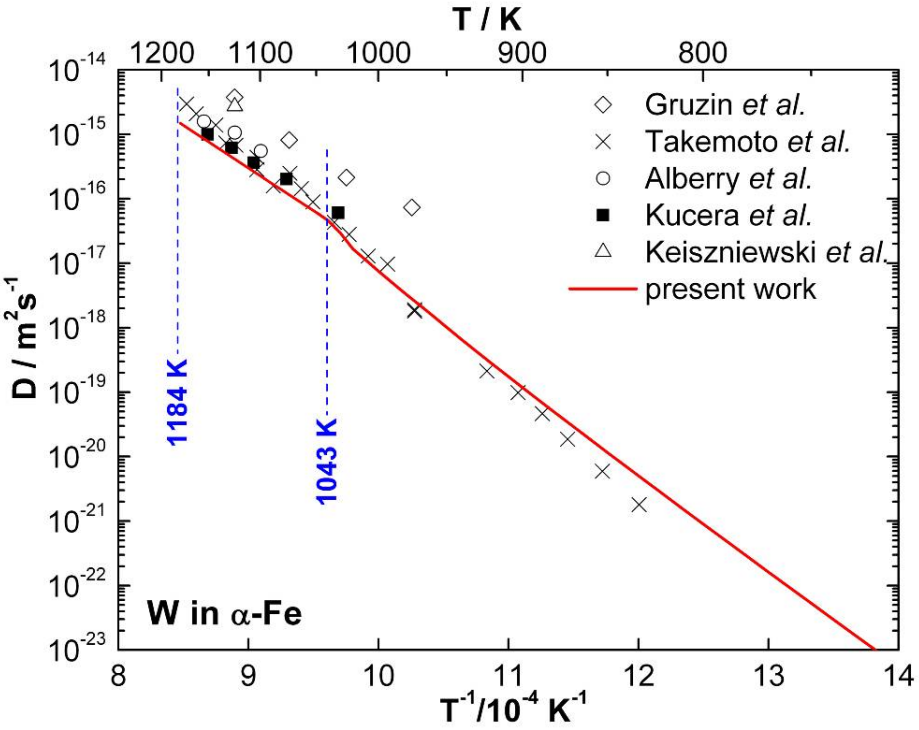

Figure 4 Predicted temperature dependence of the calculated impurity-diffusion coefficients for W in the α Fe (red line) versus published experimental data [47,52,62-64].

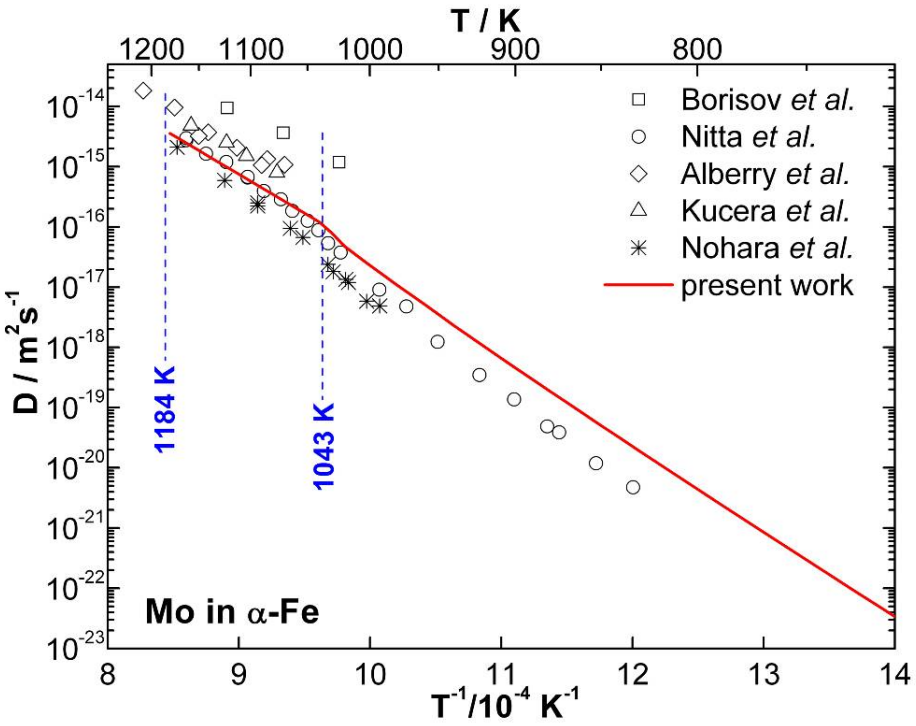

Figure 5 Predicted temperature dependence of the calculated impurity-diffusion coefficients for Mo in the α Fe (red line) versus published experimental data [53,63-66].

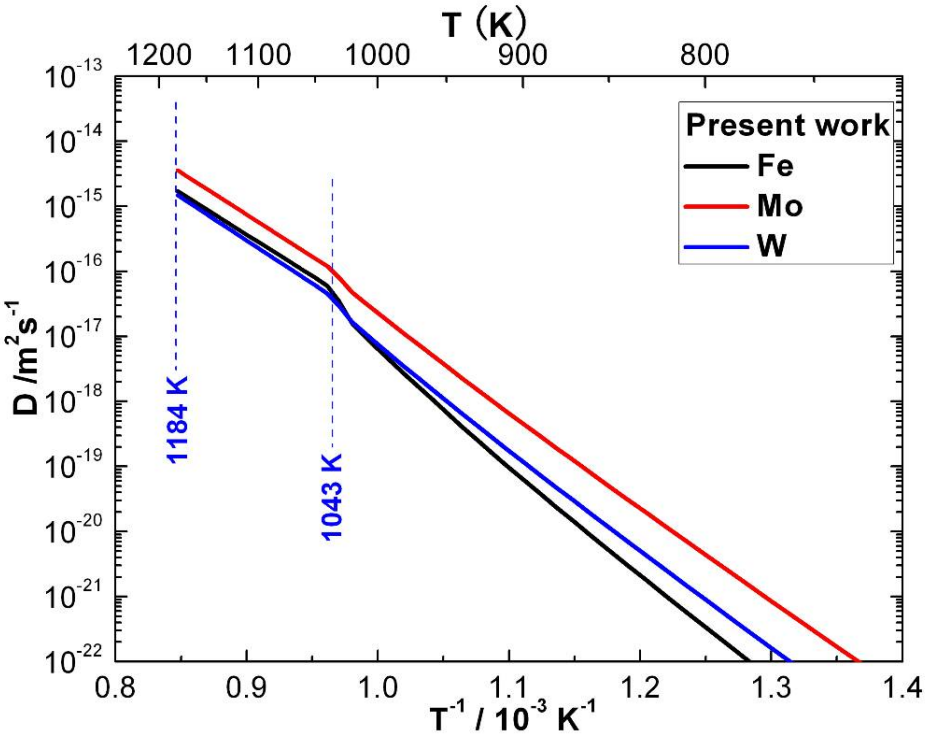

Figure 6 Predicted temperature dependence of the diffusion coefficients for W- and Mo-impurity diffusion, compared with those for self-diffusion in the α Fe.

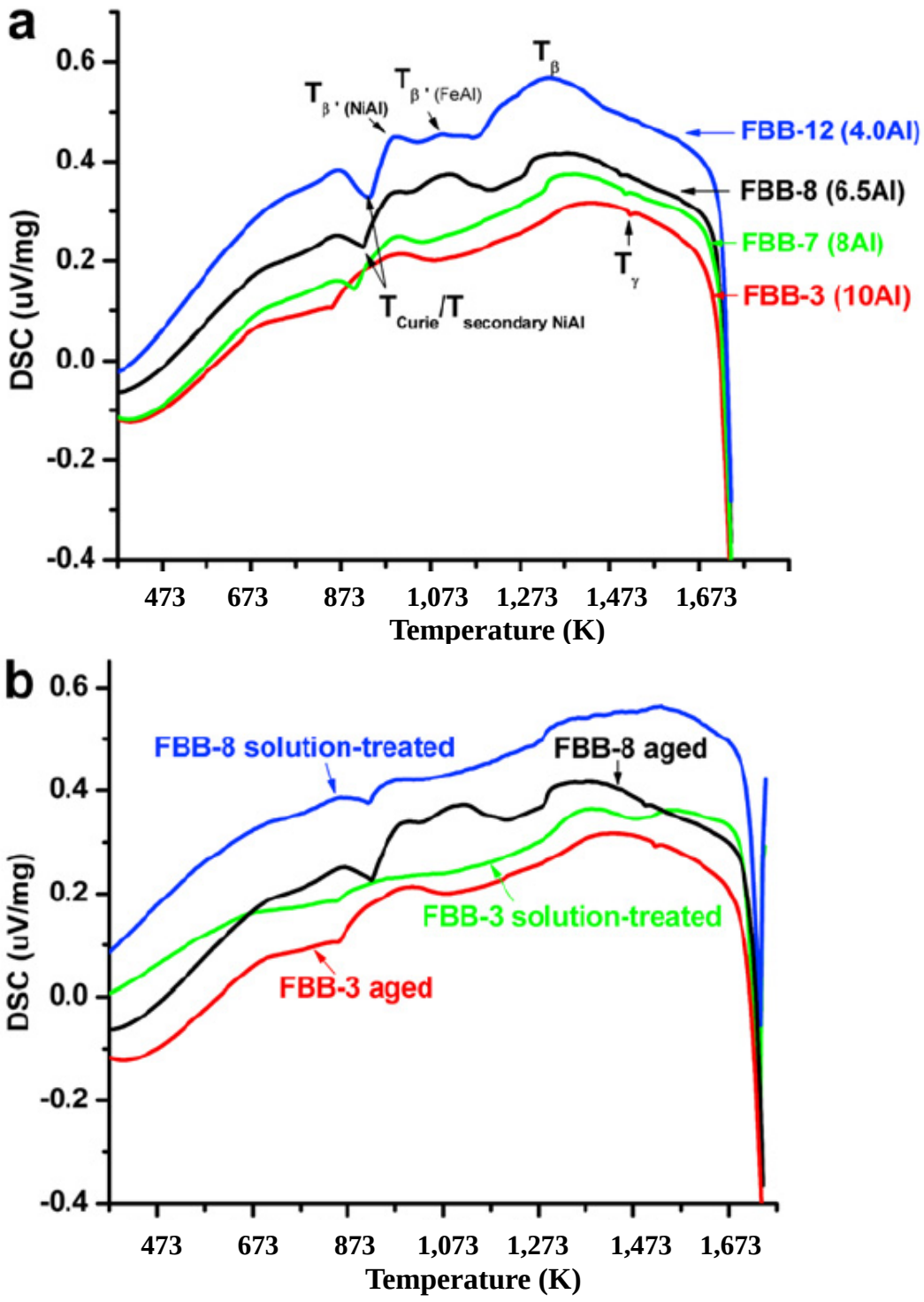

Figure 7 (a) The heating curves from the DSC analyses of the alloys with different Al% showing a phase transition peak at a temperature higher than $T_{\beta'(NiAl)}$. This trend is most likely to be the phase separation of FeAl inside NiAl, and (b) A comparison between the DSC curves of the solution-treated and aged alloys.

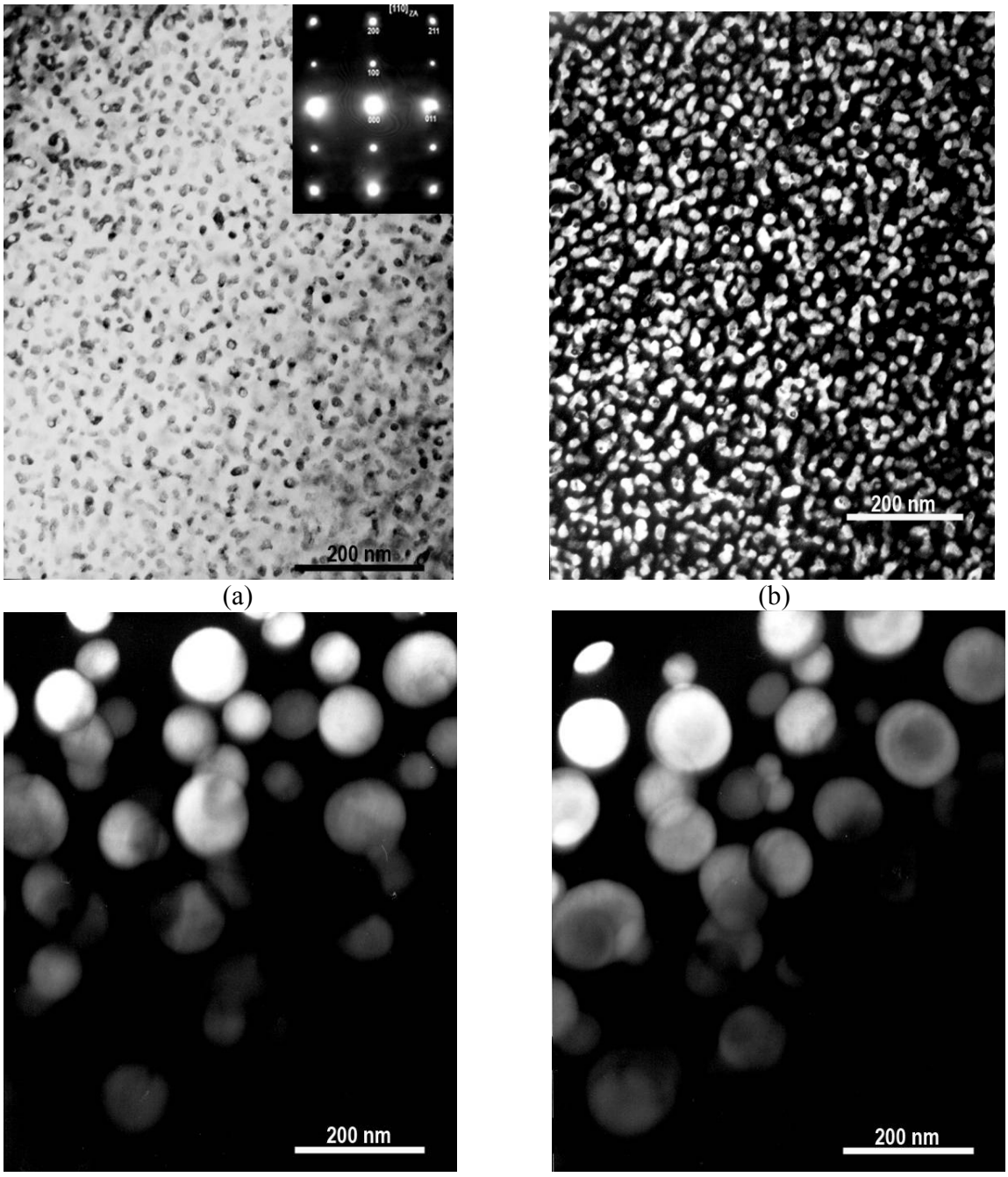

(a) (b)

(c) (d)

Figure 8. TEM micrographs of FBB-1: (a) Bright-field (BF) micrograph of the as-quenched alloy with the inset showing a [110] zon-axis selected-area-diffraction (SAD) pattern, (b) the corresponding dark-field (DF) (using the 100_{B2} reflection) micrograph of the as-quenched alloy showing *B*2 (bright) domains, (c), and (d) DF (using the 100_{B2} reflection) micrographs (from different areas) after aging (at 973 K for 100 hrs.) showing *B*2 (bright) domains.

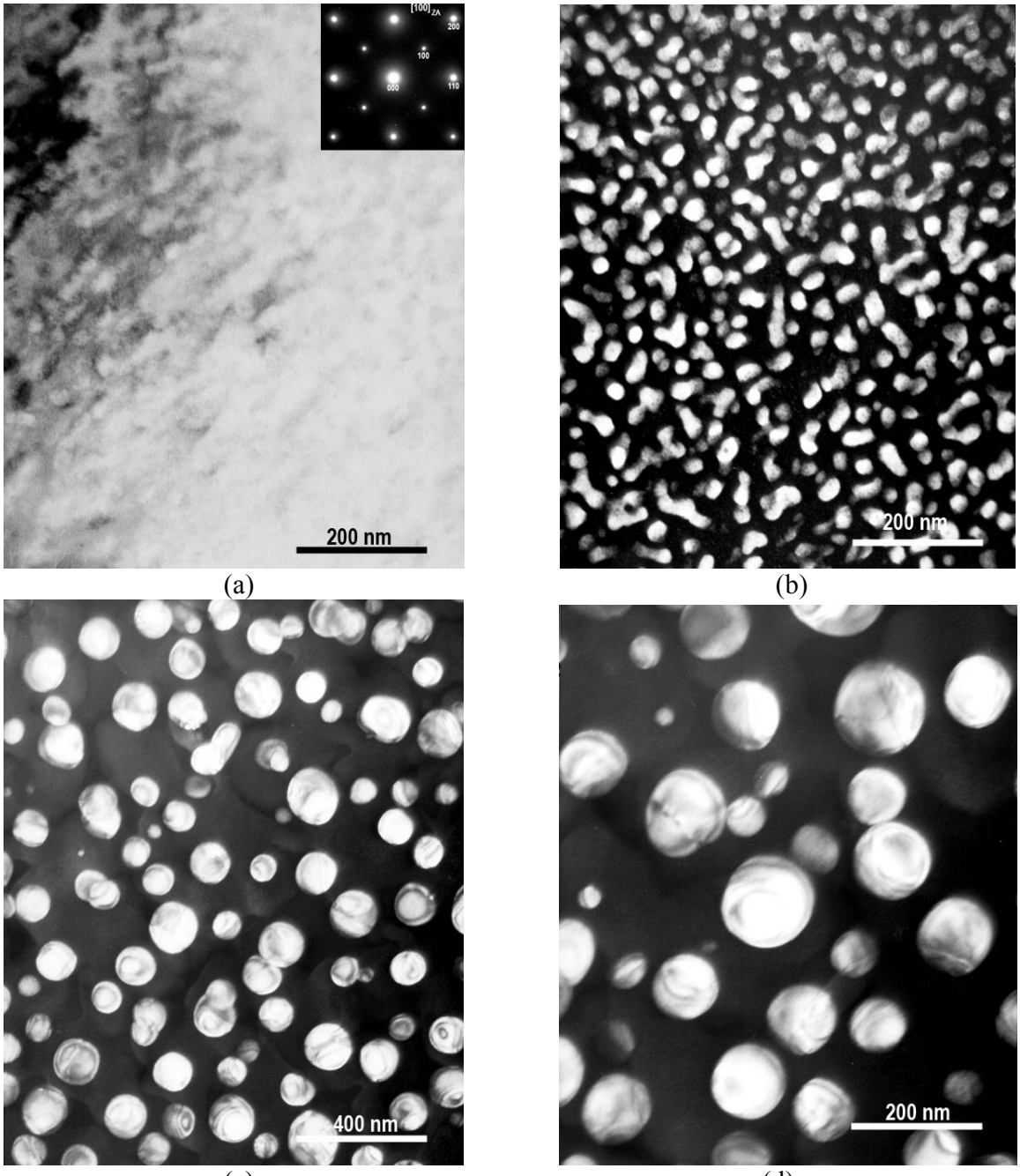

Figure 9. TEM micrographs of FBB-2: (a) BF micrograph of the as-quenched alloy with the inset showing the [100] zone-axis SAD pattern, (b) the corresponding DF (using the 100_{B2} reflection) micrograph of the as-quenched alloy showing *B*2 (bright) domains, (c) a low-magnification, and (d) a high-magnification DF (using the 100_{B2} reflection) micrographs after aging (at 973 K for 100 hrs.) showing *B*2 (bright) domains.

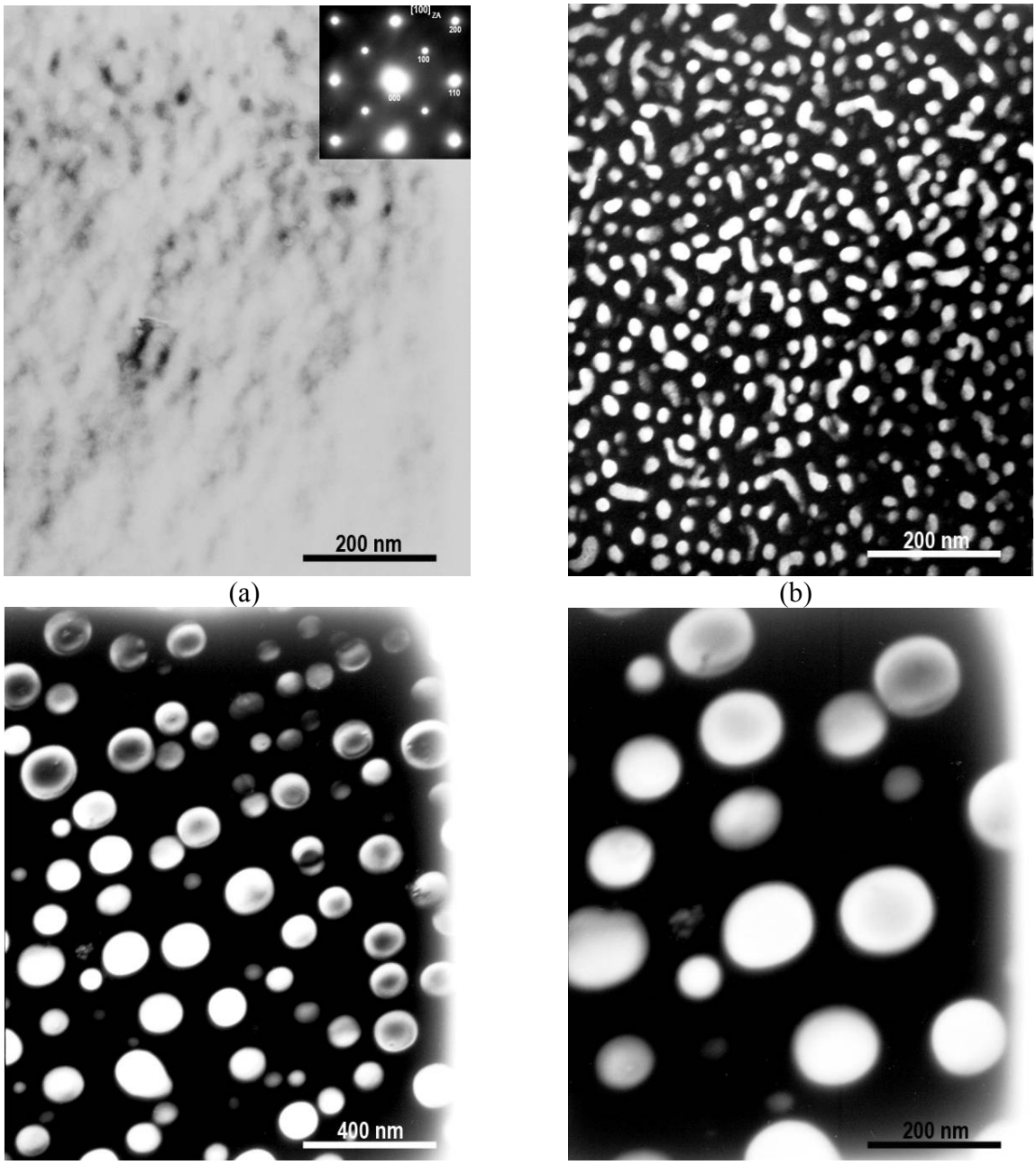

(a) (b)

(c) (d)

Figure 10. TEM micrographs of FBB-3: (a) BF micrograph of the as-quenched alloy with the inset showing the [100] zone-axis SAD pattern, (b) the corresponding DF (using the 100_{B2} reflection) micrograph of the as-quenched alloy showing *B*2 (bright) domains, (c) a low-magnification, and (d) a high-magnification DF (using the 100_{B2} reflection) micrographs after aging (at 973 K for 100 hrs.) showing *B*2 (bright) domains.

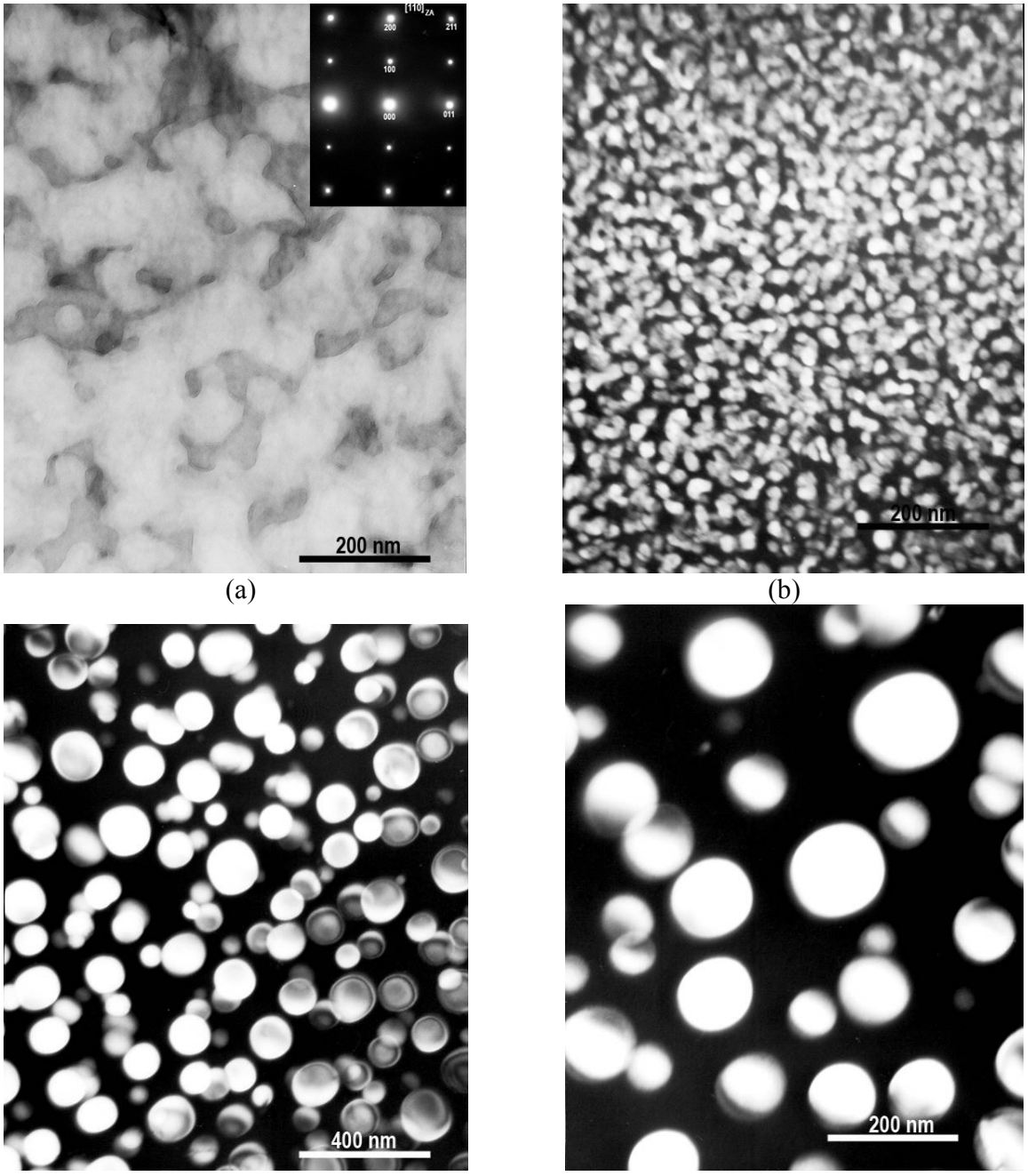

(a) (b)

(c) (d)

Figure 11. TEM micrographs of FBB-4: (a) BF micrograph of the as-quenched alloy with the inset showing the [110] zone-axis SAD pattern, (b) the corresponding DF (using the 100_{B2} reflection) micrograph of the as-quenched alloy showing *B*2 (bright) domains, (c) a low-magnification, and (d) a high-magnification DF (using the 100_{B2} reflection) micrographs after aging (at 973 K for 100 hrs.) showing *B*2 (bright) domains.

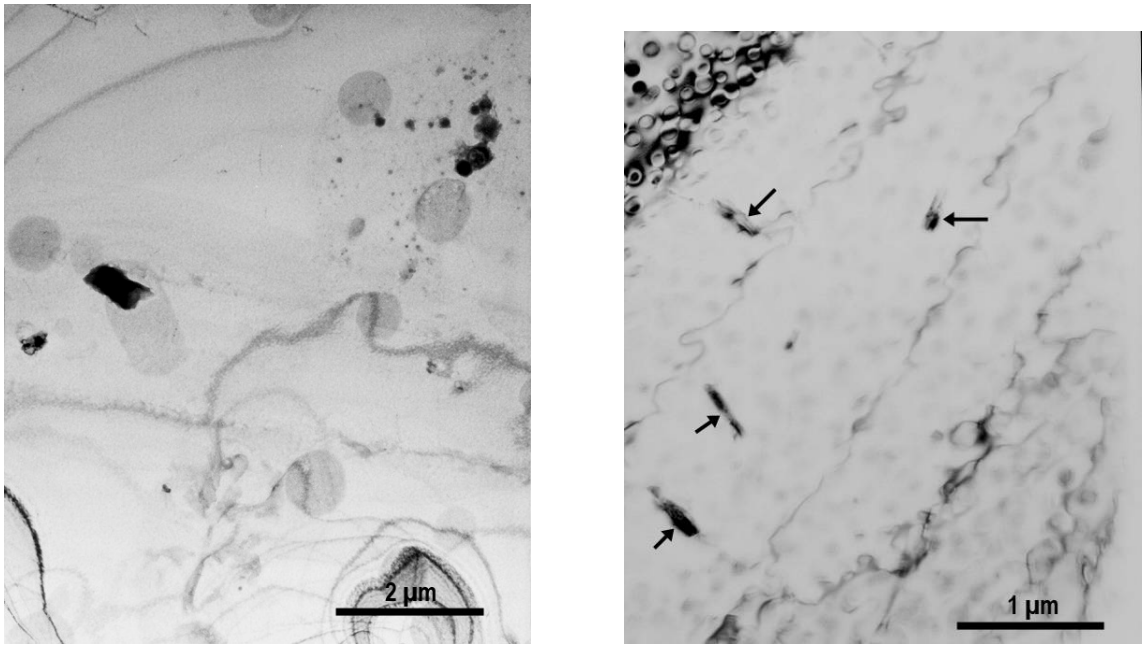

(a) (b)

Figure 12. TEM micrographs showing minor phases: (a) BF micrograph of the as-quenched FBB-2 and (b) BF micrograph of the heat-treated FBB-3 showing lath-shaped (marked with arrows) precipitates.

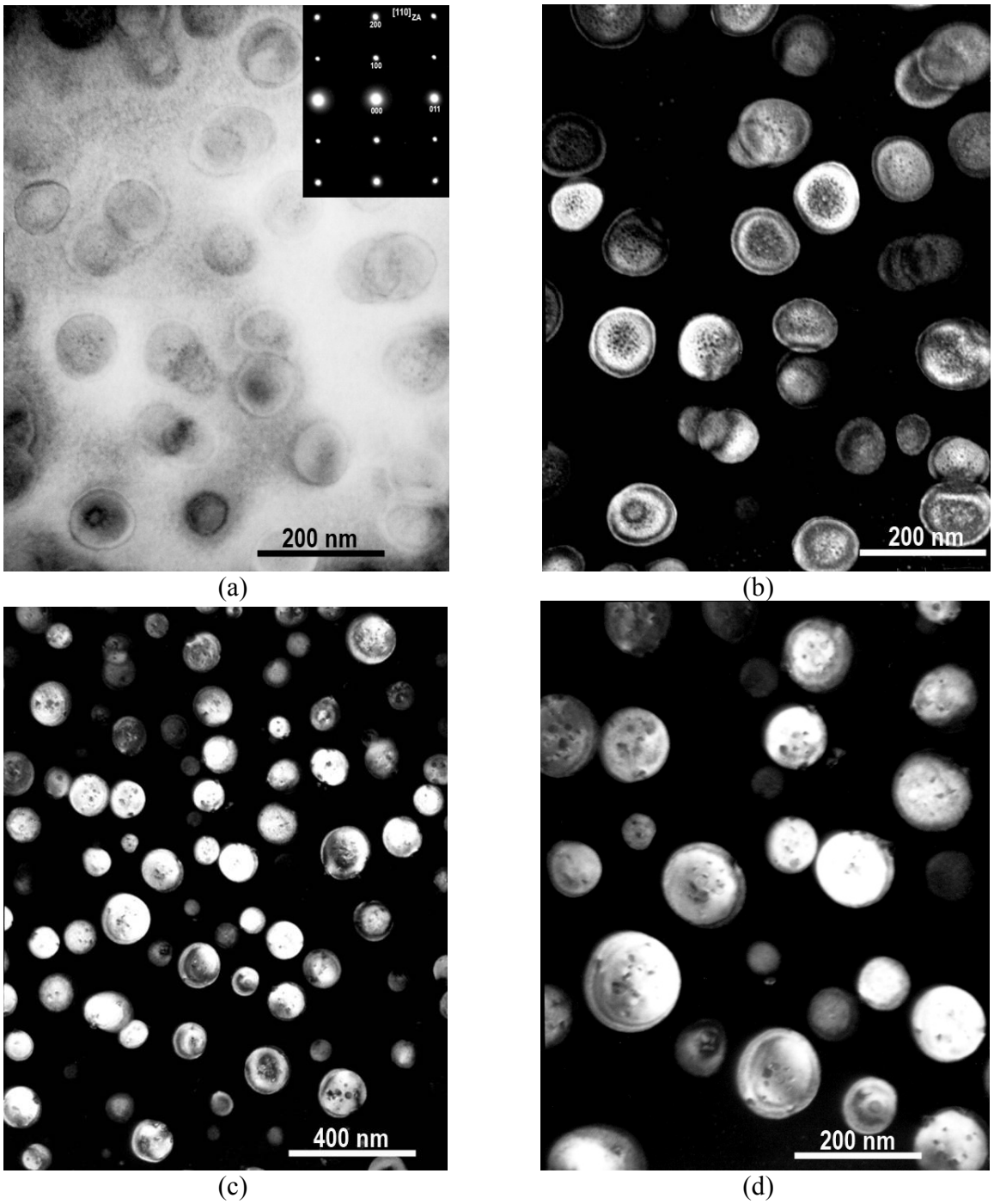

Figure 13. TEM micrographs of FBB-7: (a) BF micrograph of the as-quenched alloy with the inset showing the [110] zone-axis SAD pattern, (b) the corresponding DF (using the 100_{B2} reflection) micrograph of the as-quenched alloy showing *B*2 (bright) domains, (c) a low-magnification, and (d) a high-magnification DF (using the 100_{B2} reflection) micrographs after aging (at 973 K for 100 hrs.) showing *B*2 (bright) domains. The presence of nanoscale dark regions within *B*2 (bright) domains may be noted in (b)-(d).

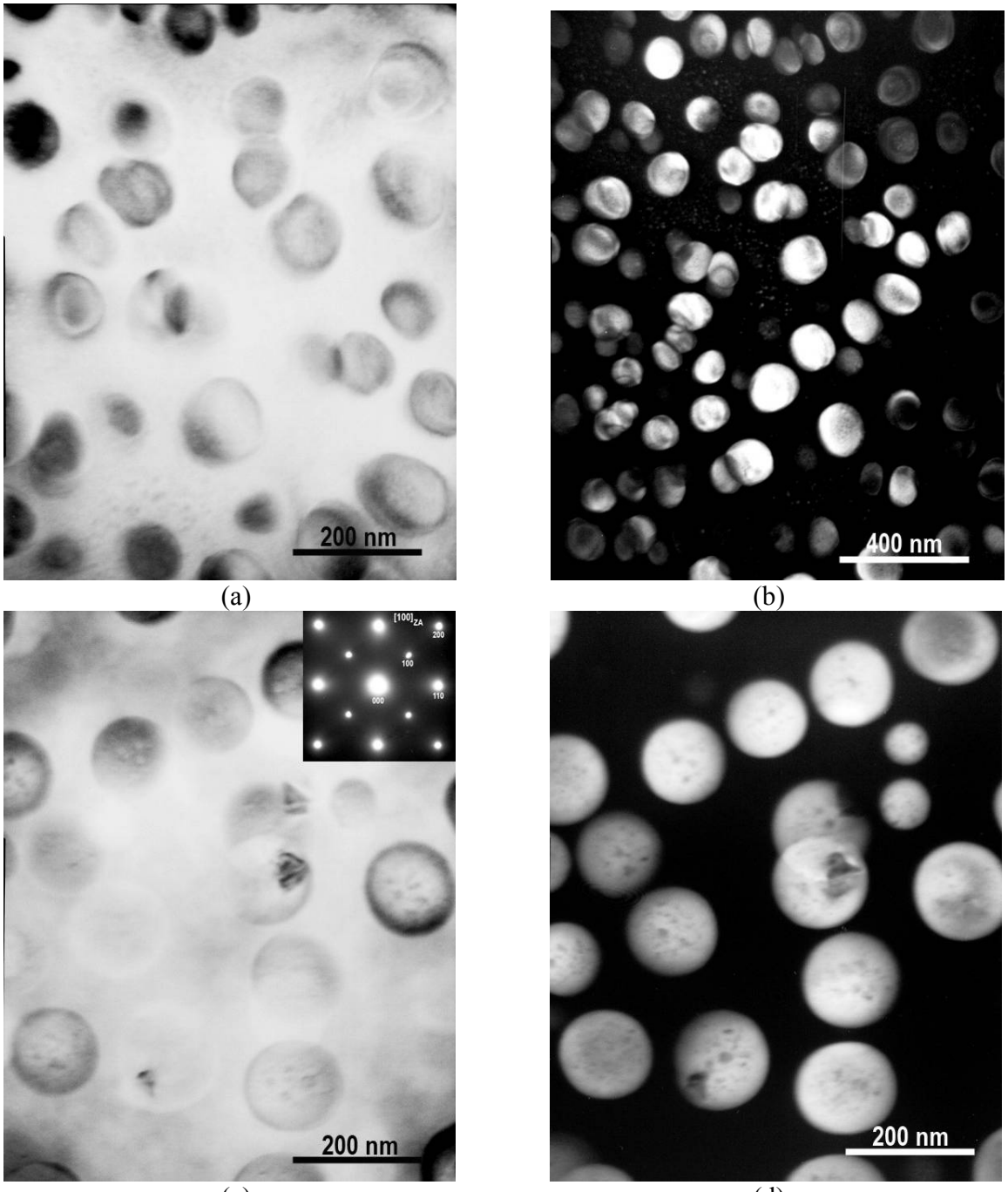

Figure 14. TEM micrographs of FBB-8: (a) BF micrograph of the as-quenched alloy, (b) the DF (using the 100_{B2} reflection) micrograph of the as-quenched alloy showing *B*2 (bright) domains, (c) BF micrograph with the inset showing the [100] zone-axis SAD pattern, and (d) the corresponding DF (using the 100_{B2} reflection) micrographs after aging (at 973 K for 100 hrs.) showing *B*2 (bright) domains. The presence of nanoscale dark regions within *B*2 (bright) domains may be noted in (c)-(d).

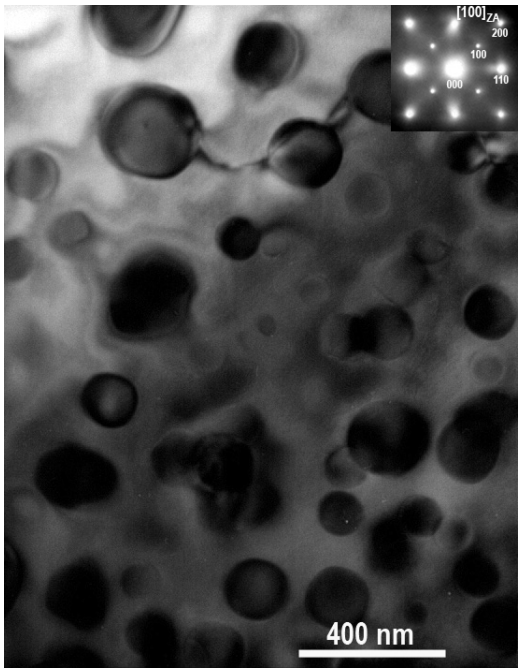

(a)

(b)

Figure 15. TEM micrographs of FBB-12: (a) BF along with the diffraction pattern (inset), and (b) the corresponding DF taken using the (100)-type superlattice reflection. While most precipitates are fully coherent, some appear to be semicoherent as the presence of dislocations may also be seen.

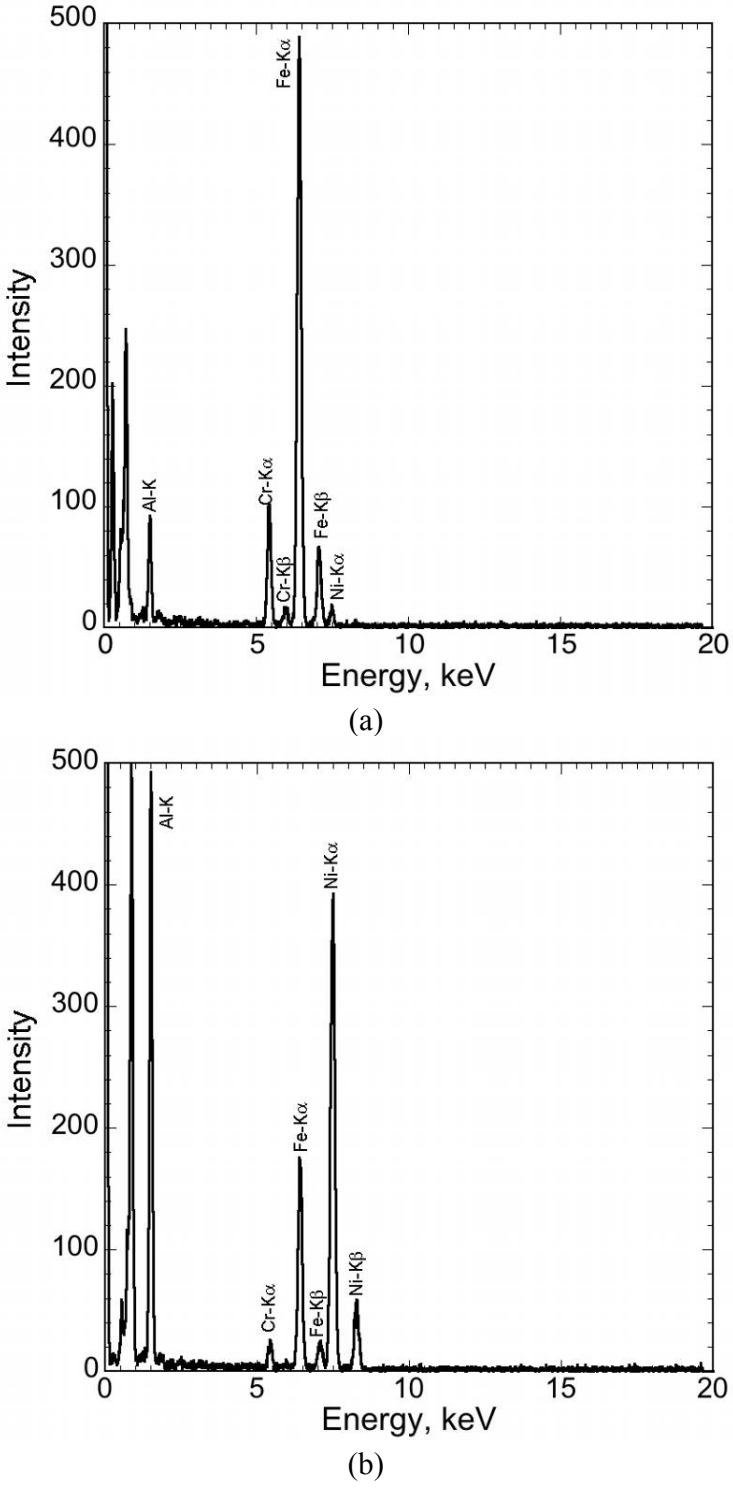

Figure 16. As-collected energy-dispersive X-ray (EDX) spectra in the analytical-electron microscopy (AEM) using thin foils of FBB-1 heat-treated at 973 K for 100 hrs: (a) matrix, and (b) NiAl-type precipitate.

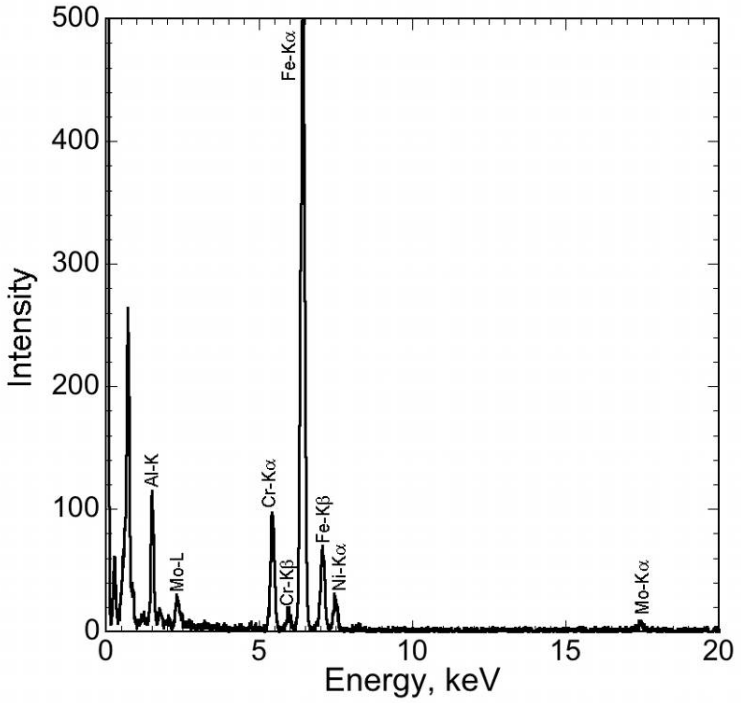

(a)

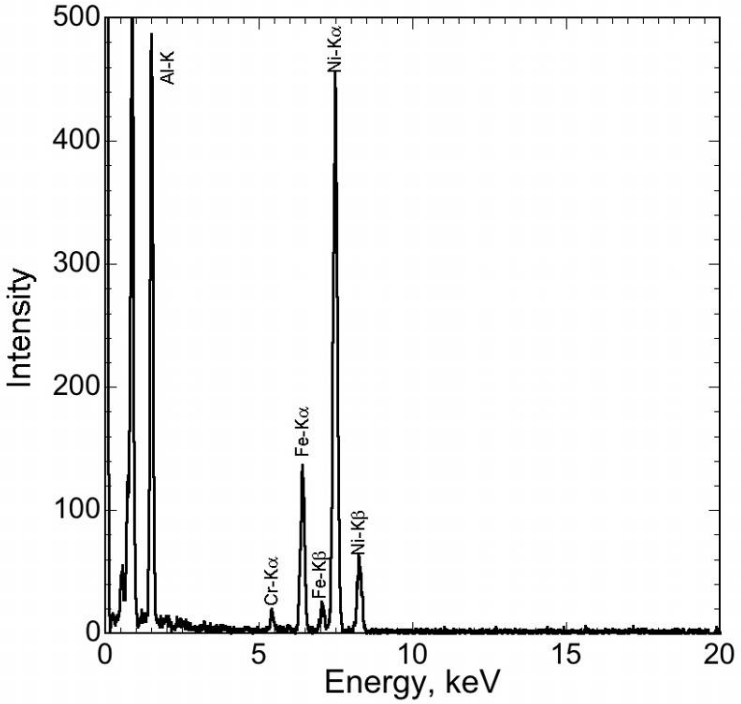

(b)

Figure 17. As-collected EDX spectra in AEM using thin foils of FBB-2 heat-treated at 973 K for 100 hrs: (a) matrix, and (b) NiAl-type precipitate.

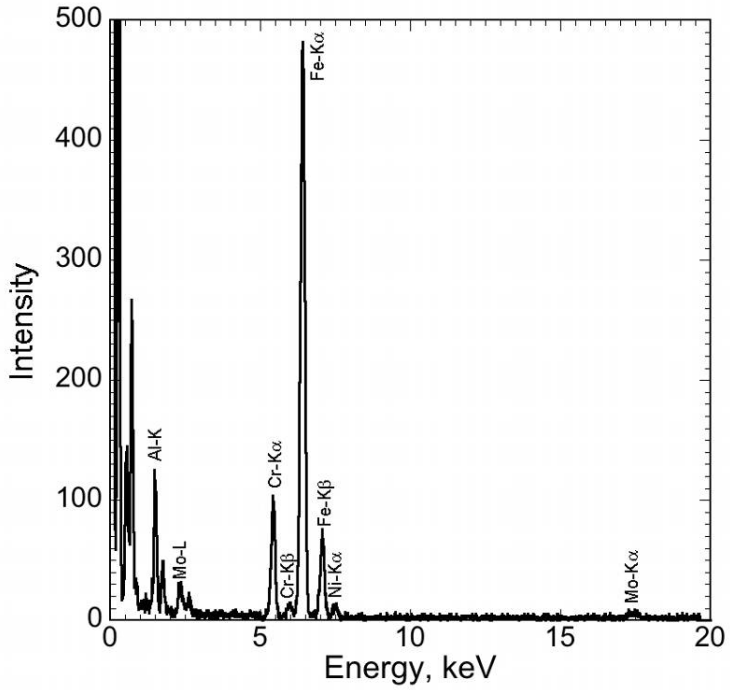

(a)

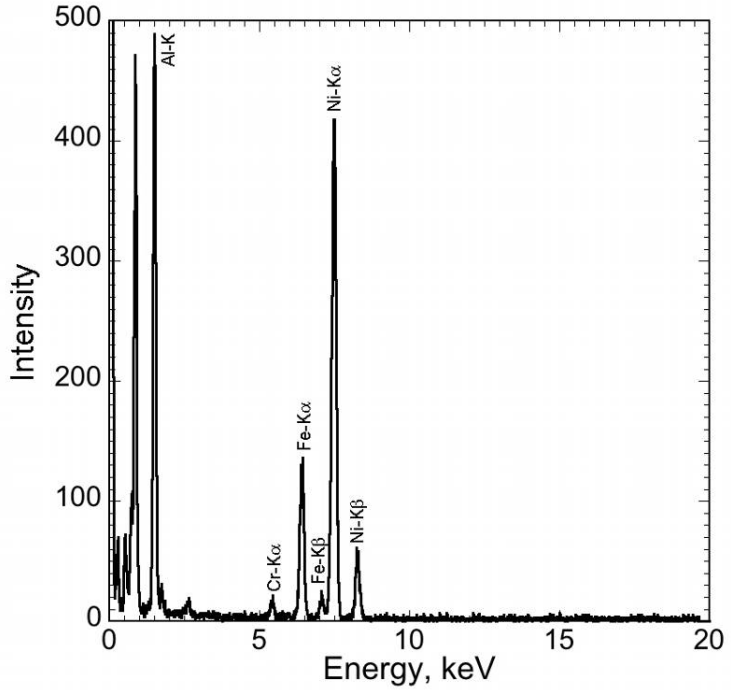

(b)

Figure 18. As-collected EDX spectra of FBB-3 aged at 973 K for 100 hrs: (a) matrix, and (b) NiAl-type precipitate.

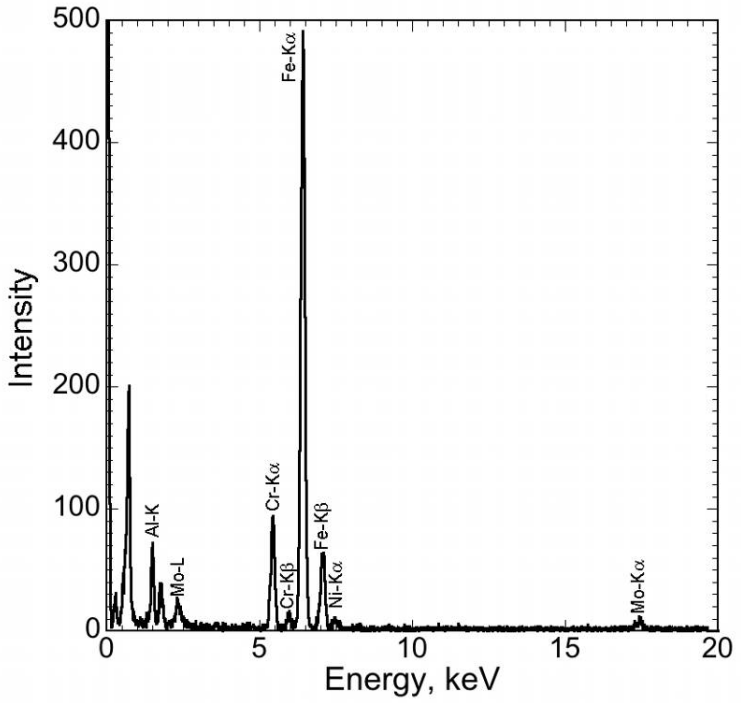

(a)

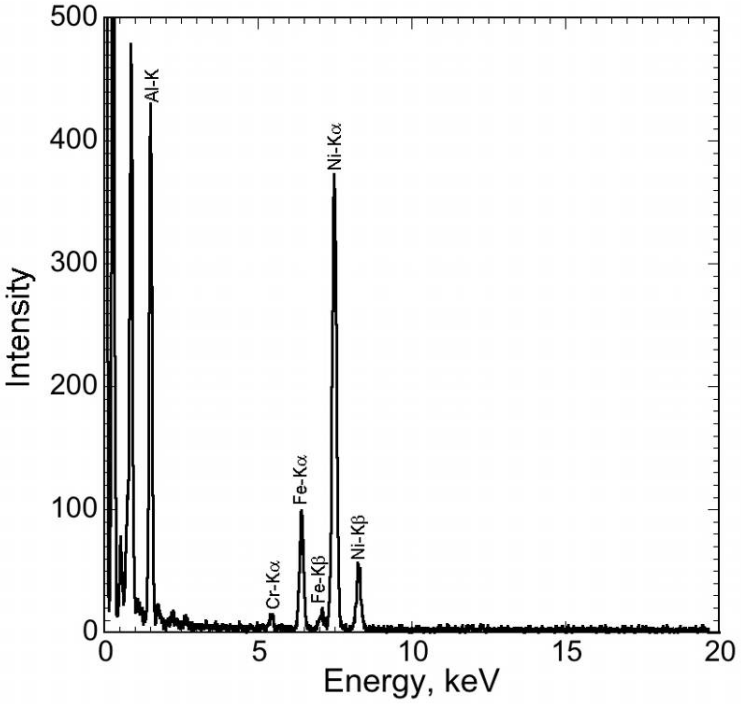

(b)

Figure 19. As-collected EDX spectra in AEM using thin foils of FBB-7 heat-treated at 973 K for 100 hrs: (a) matrix, and (b) NiAl-type precipitate.

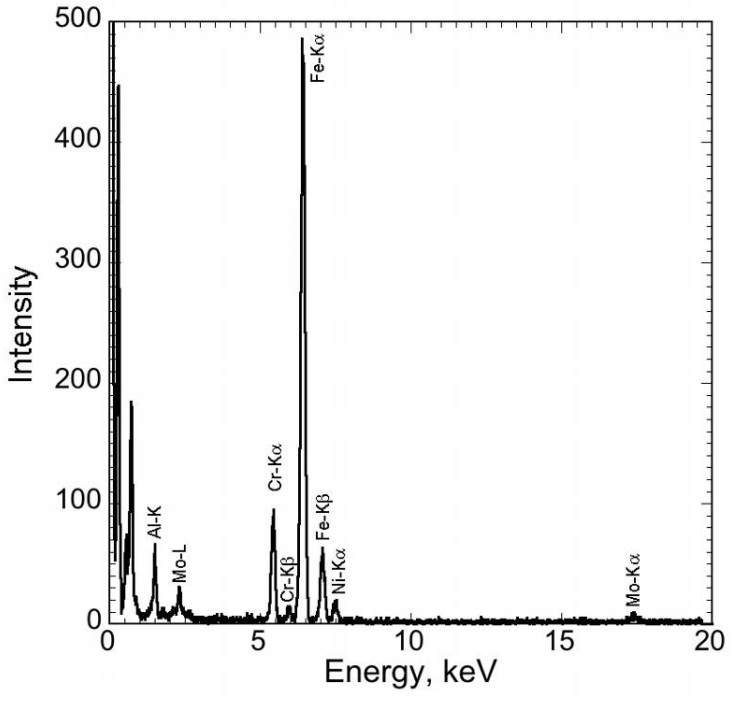

(a)

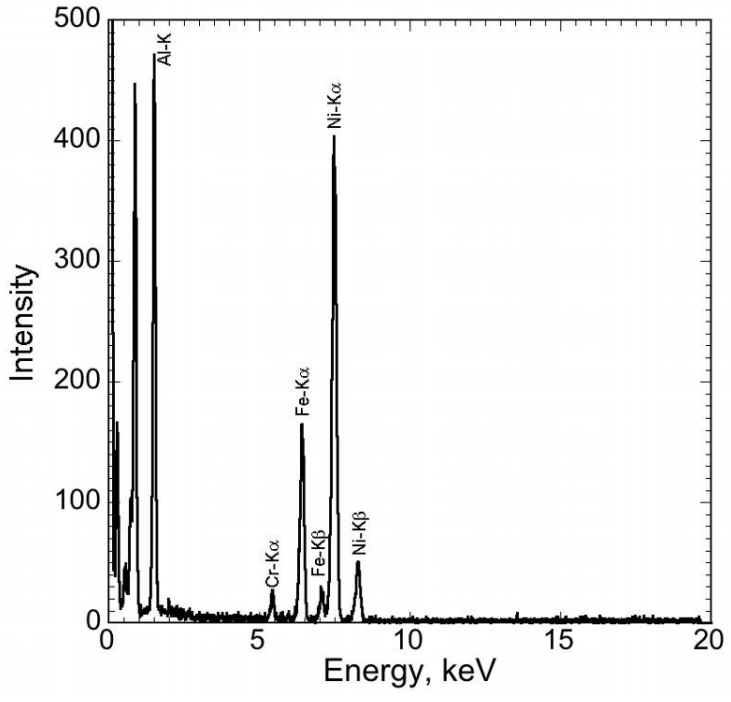

(b)

Figure 20. As-collected EDX spectra of FBB-8 aged at 973 K for 100 hrs: (a) matrix, and (b) NiAl-type precipitate.

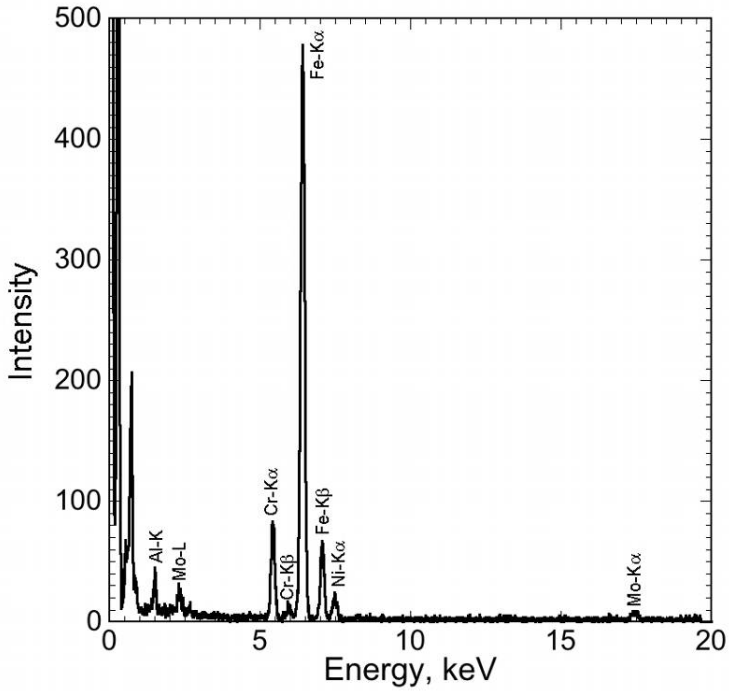

(a)

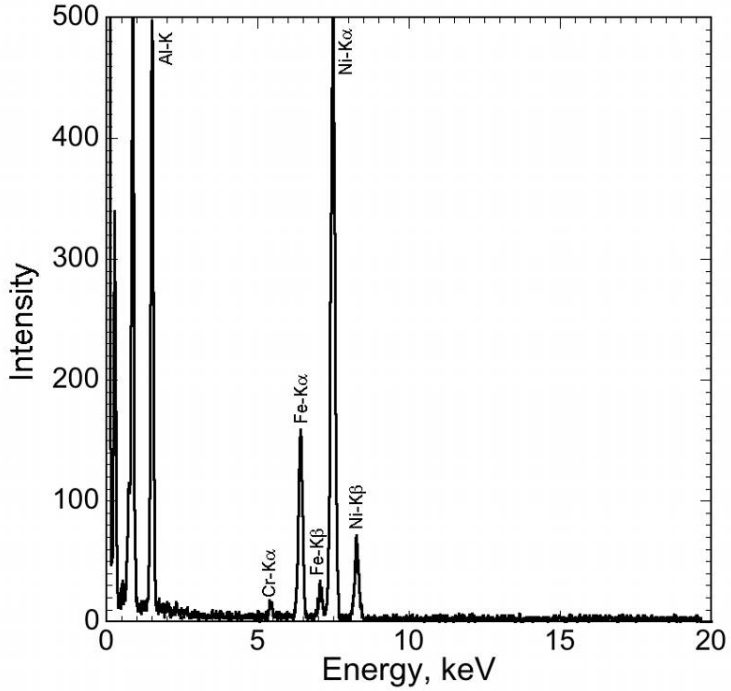

(b)

Figure 21. As-collected EDX spectra of FBB-12 aged at 973 K for 100 hrs: (a) matrix, and (b) NiAl-type precipitate.

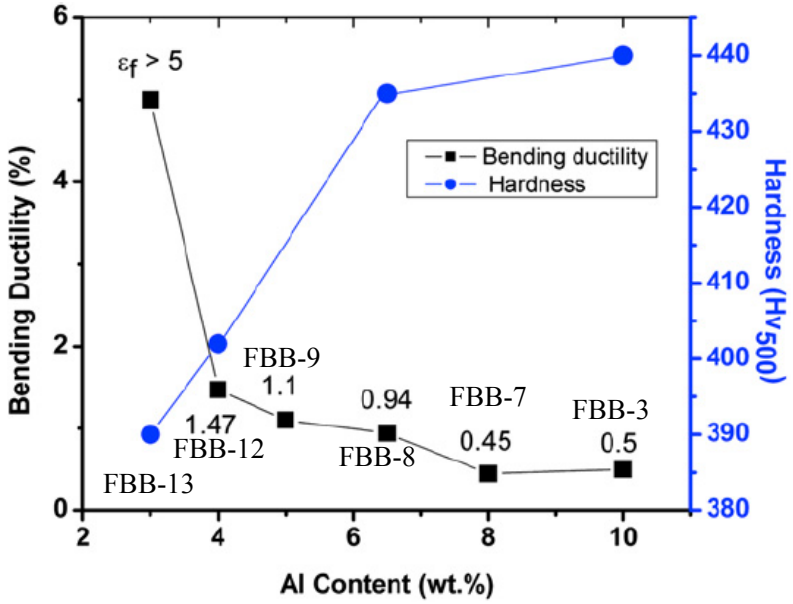

Figure 22. The effects of Al content in the alloy on the bending ductility and hardness of prototype alloys, where ε_f is the failure strain on the outer surface of the strip sample.

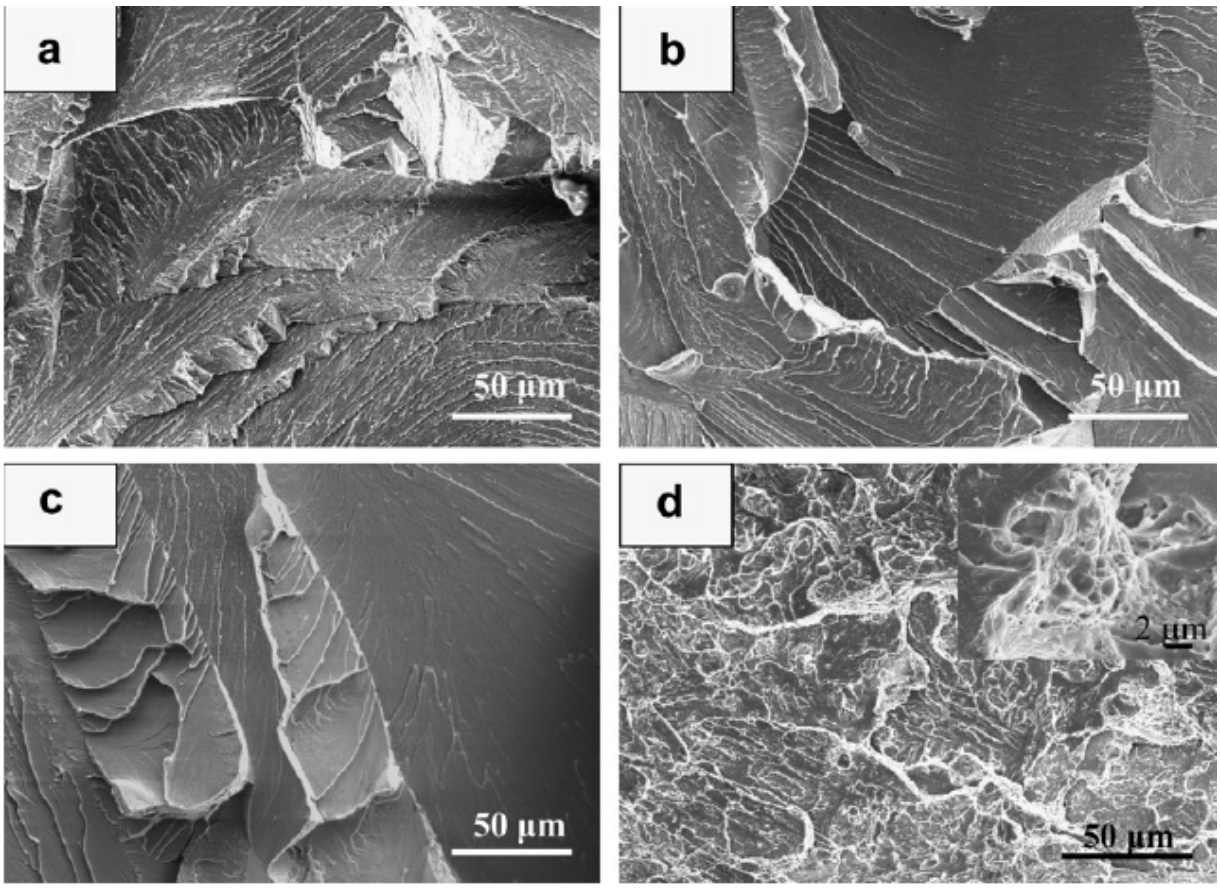

Figure 23. Cleavage-fracture surfaces of bending-tested samples (a) FBB-3, (b) FBB-8, (c) FBB-9, and (d) FBB-13, the representative ductile fracture is shown as an inset.

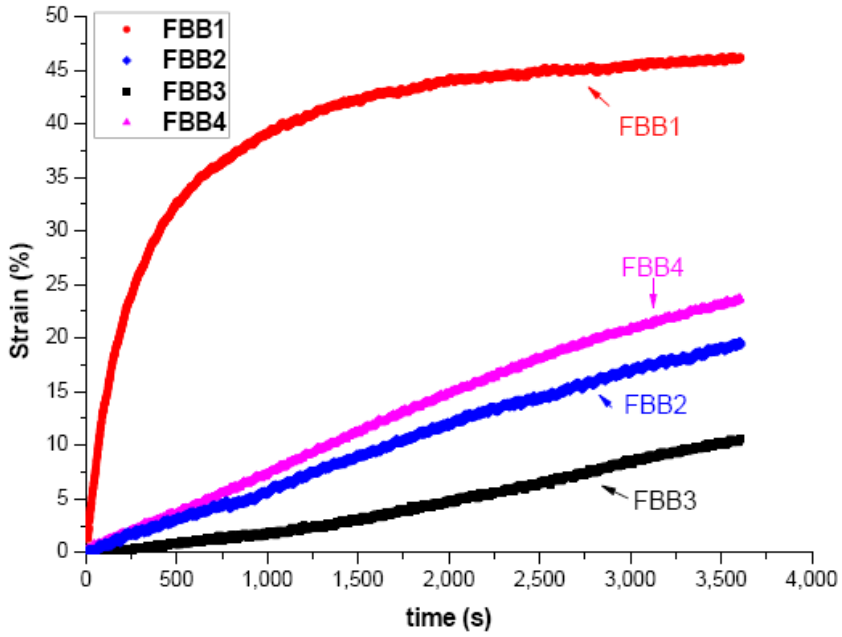

Figure 24. Strain-time compressive-creep curves of FBB-1, FBB-2, FBB-3, and FBB-4 alloys at 973 K and compressive stress of 160 MPa in vacuum for 1 hr.

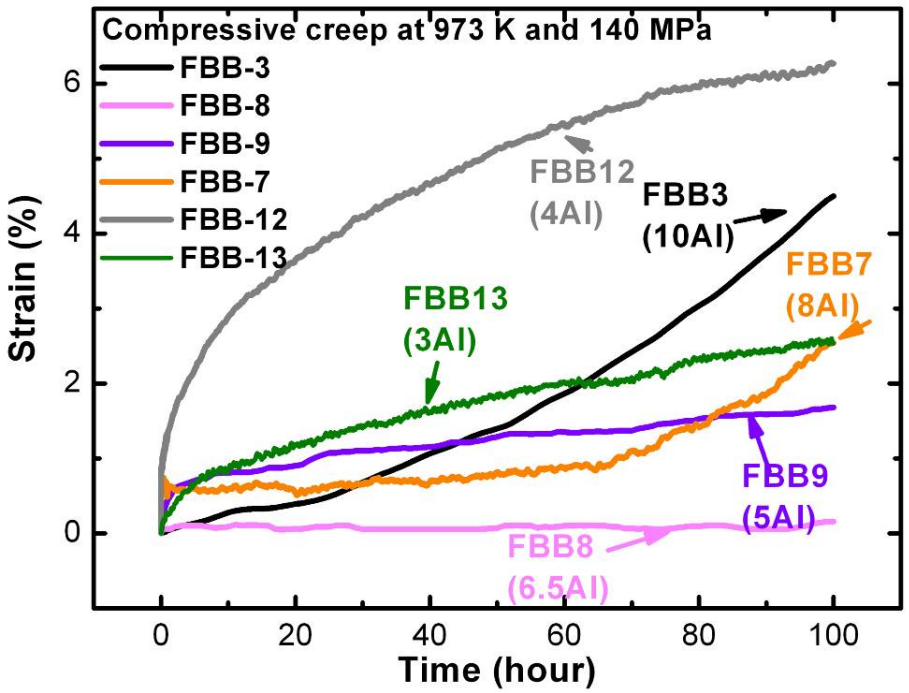

Figure 25. Compressive-creep curves for alloys with various amounts of Al plotting strain as a function of time at 973 K and 140 MPa in air.

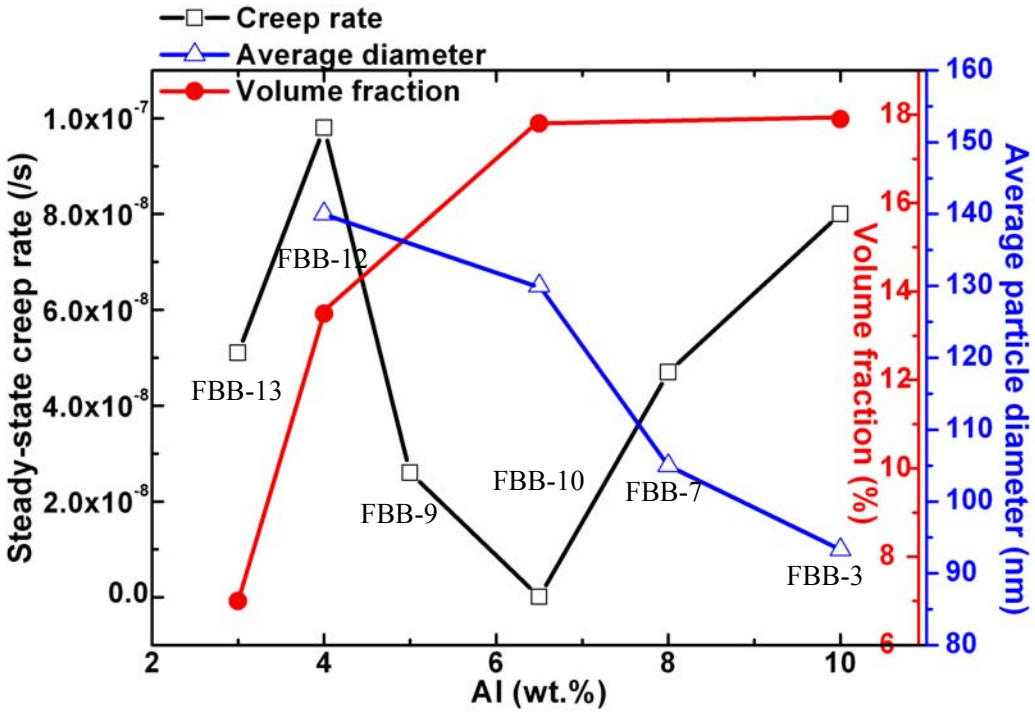

Figure 26. Compressive steady-state creep rates at 973 K and a compressive stress of 140 MPa, average precipitate diameters determined by TEM, and volume fractions of precipitates as a function of Al%.

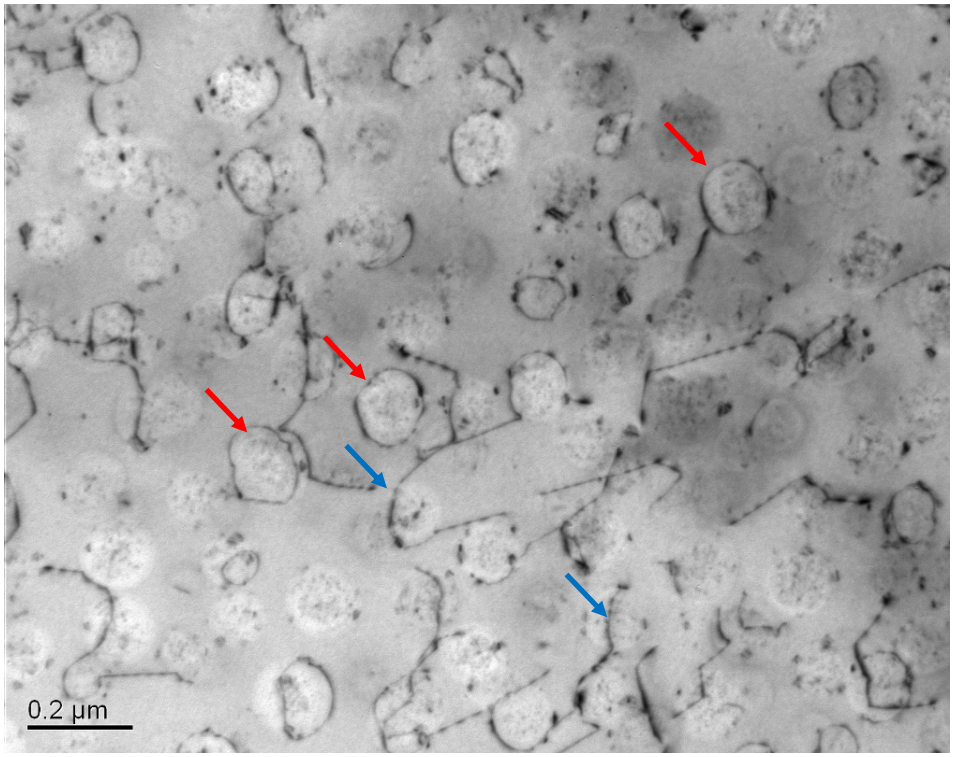

(a)

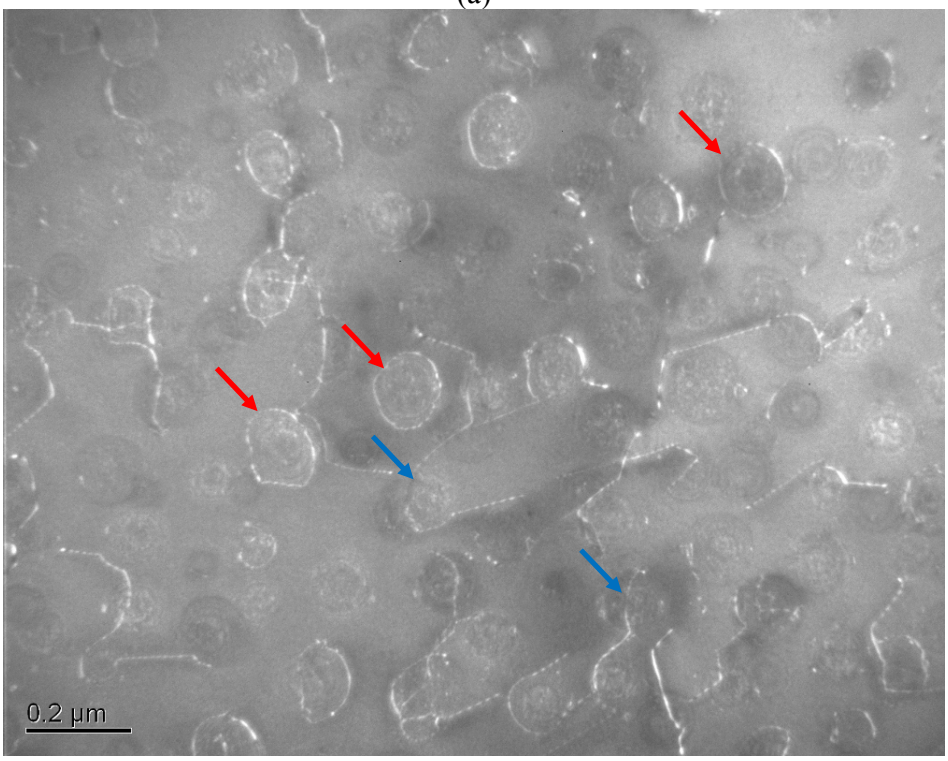

(b)

Figure 27. (a) BF and (b) DF micrographs of dislocation-particle interactions identified as the Orowan bowing (dislocation loop) (red arrows) and dislocation climb (blue arrows) in the compressively-crept FBB-8.

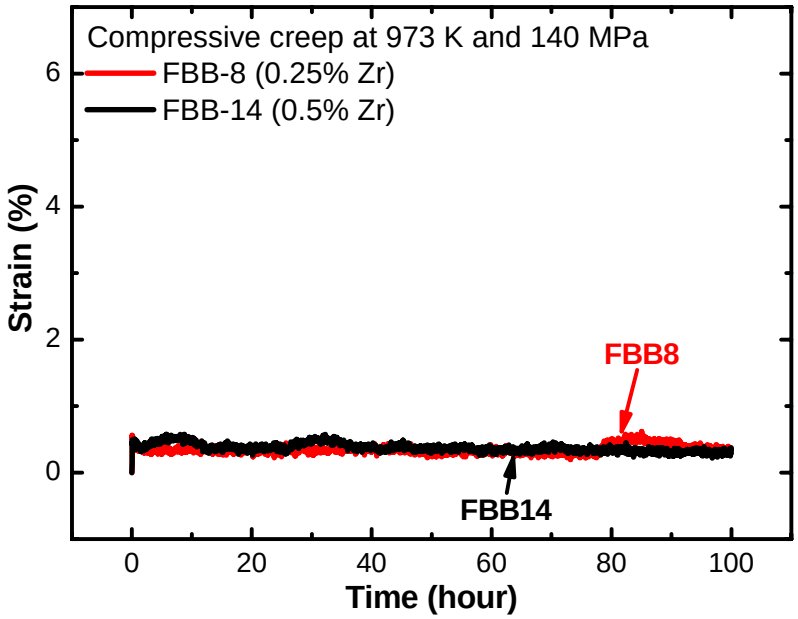

Figure 28. Compressive-creep curves of FBB-8 (0.25 wt.% Zr) and -14 (0.5 wt.% Zr) at 973 K and 140 MPa in air.

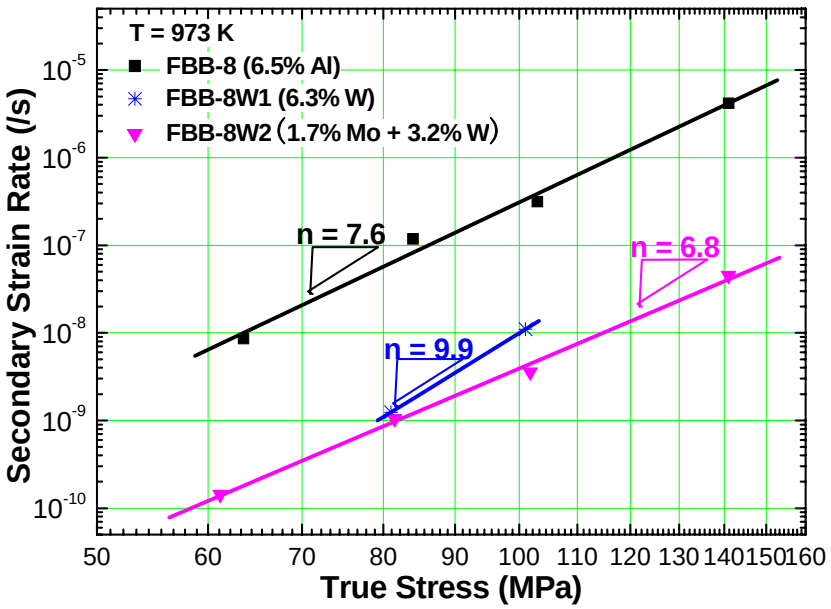

(a)

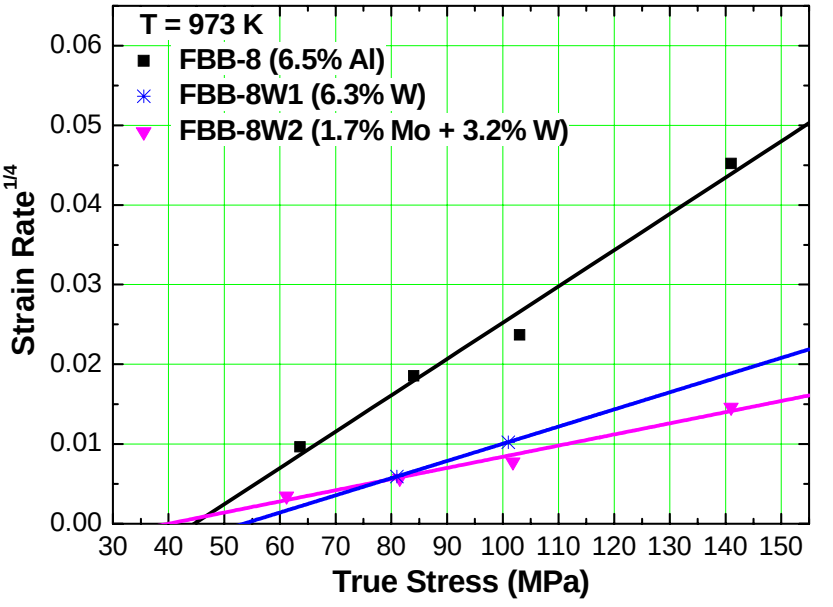

(b)

Figure 29. (a) Secondary strain rate vs. true stress at 973 K for FBB-8, -8W1, and -8W2; (b) secondary strain rate$^{1/4}$ vs. true stress at 973 K for FBB-8, -8W1, and -8W2. The threshold stresses are determined to be 44.6 MPa for FBB-8, 53.8 MPa for FBB-8W1, and 40 MPa for FBB-8W2.

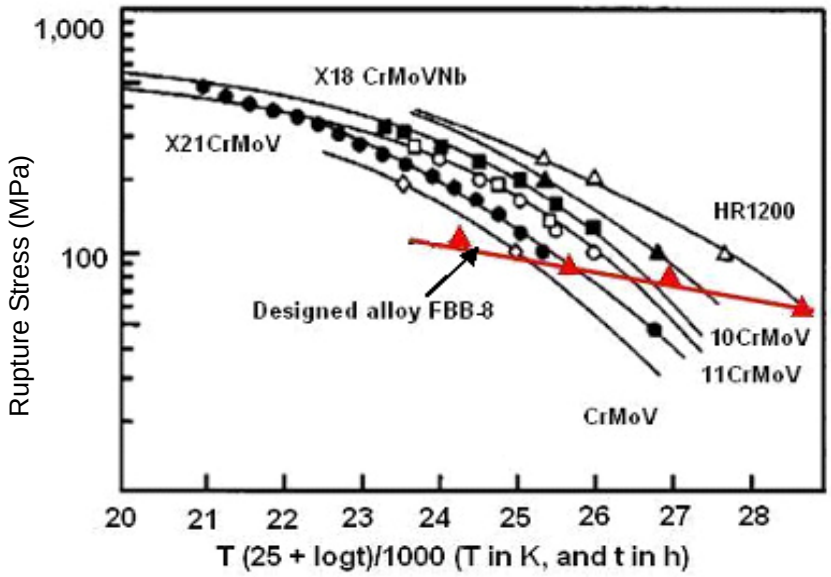

Figure 30. A comparison of the LMP plots between FBB-8 and other Fe-based materials candidates for steam-turbine applications [135], where the LMP is calculated by T(25 + log t)/1,000, where T is the temperature, and t is the rupture time. Tensile-creep tests were performed at 973 K under stresses of 140, 100, 80, and 60 MPa.

E. ACKNOWLEDGEMENT

This work is supported by The Department of Energy (DOE) Office of Fossil Energy Program, under Grant No. DE-FG26-06NT42732, with Dr. Patricia Rawls and Mr. Vito Cedro as the program directors. We very much appreciate Ms. Shenyan Huang's great efforts in preparing this report. The use of SHaRE User Facility at the Oak Ridge National Laboratory is sponsored by the Scientific User Facilities Division, Office of Basic Energy Sciences, U.S. Department of Energy. We would like to thank Dr. Carl McHargue, Director of the Center for Materials Processing, The University of Tennessee, for providing matching funds.

F. REFERENCES

[1] Turchi PEA, Abrikosov IA, Burton B, Fries SG, Grimvalle G, Kaufman L, Korzhavyi P, Manga VR, Ohno M, Pisch A, Scott A, Zhang WQ. CALPHAD 2007;31:4

[2] Ruban AV, Abrikosov IA. Rep. Prog. Phys. 2008;71:046501

[3] Van de Walle A, Ghosh G, Asta M. In: Bozzolo G, Noebe RD, Abel P, editors. Applied Computational Materials Modeling, Springer (New York), 2007. p. 1.

[4] Van de Walle A. CALPHAD 2009;33:266

[5] Fahnle M, Drautz R, Lechermann F, Singer R, Diaz-Ortiz A, Dosch H. Phys Stat Solidi B 2005;242:1159

[6] Liu ZK, J. Phase Equilib. Diffus. (in press).

[7] Lukas HL, Fries SG, Sundman B. Computational Thermodynamics: The CALPHAD Method, Cambridge University Press (Cambridge), 2007.

[8] Kattner UR, Campbell CE. Materials Science and Technology 2009;4:443

[9] Ghosh G, Olson GB. Acta Mater. 2007;55:3281

[10] Wolverton C, Yan XY, Vijayaraghavan R, Ozolins V. Acta Mater. 2002;50:2187

[11] Domain C, Becquart CS. Phys. Rev. B 2001;65:024103

[12] Domain C, Becquart CS, Foct J. Phys. Rev. B 2004;69:144112

[13] Janotti A, Krcmar M, Fu CL, Reed RC. Phys. Rev. Lett. 2004;92:085901

[14] Domain C, Becquart CS. Phys. Rev. B 2005;71:214109

[15] Krcmar M, Fu CL, Janotti A, Reed RC. Acta Mater. 2005;53:2369

[16] Sandberg N, Holmestad R. Phys. Rev. B 2006;73:014108

[17] Olsson P, Domain C, Wallenius J. Phys. Rev. B 2007;75:014110

[18] Sandberg N, Hanriksson KOE, Wallenius J. Phys. Rev. B 2008;78:094110

[19] Simonovic D, Sluiter MHF. Phys. Rev. B 2009;79:054304

[20] Mantina M, Wang Y, Chen LQ, Liu ZK, Wolverton C. Acta Mater. 2009;57:4102

[21] Van der Ven A, Ceder G. Phys. Rev. Lett. 2005;94:045901

[22] Becquart CS, Domain C. Nucl. Instrum. Methods Phys. Res. B 2002;202:44

[23] Wong KL, Lee HJ, Shim JH, Sadigh B, Wirth BD. J. Nucl. Mater. 2009;227:386

[24] Choudhury S, Barnard L, Tucker JD, Allen TR, Asta M, Wirth BD, Morgan D. J. Nucl. Mater. (to be submitted)

[25] Bhadeshia HKDH. ISIJ International 2001;41:626

[26] Zhu SM, Tjong SC, Lai JKL. Acta. Mater. 1998;46:2969
[27] Stallybrass C, Schneider A, Sauthoff G. Intermetallics, 2005;13:1263
[28] Teng ZK, Liu CT, Ghosh G, Liaw PK. Intermetallics, 2010;18:1437.
[29] Teng ZK, Miller MK, Huang S, Ghosh G, Russell KF, Liu CT, Liaw PK. Scripta Materialia 2010;63:61
[30] Totemeier TC, Gale WF, editors. Smithells Metals Reference Book, 8nd ed., Butterworth-Heinemann Co. Ltd., 2004. p. 13.
[31] Pérez RA, Torres DN, Dyment F. Appl. Phys. A 2005;81:787
[32] Klugkist P, Herzig C. Phys. Stat. Sol. (a) 1995;148:413
[33] Graham D, Tomlin DH. Phil. Mag. 1963;8:1581
[34] James DW, Leak GM. Phil. Mag. 1966;14:701
[35] Treheux D, Marchive D, Delagran J. Comptes Rendus des Seances del Academie des Sciences, Serie C: Sciences Chimiques 1972;274:1260
[36] Mortlock AJ, Ewens PM, Phys. Rev. 1967;156:814
[37] Richter I, Feller-Kniepmeier M. Phys. Stat. Solidi (a) 1981;68:289
[38] Huntz AM, Aucoutur M, Lacombe P. Compt. Rend. 1967;265:554
[39] Anand MS, Agarwala RP. J. Appl. Phys. 1966;37:4248
[40] Obrtlik K, Kucera J, Phys. Stat. Sol. (a) 1979;53:589
[41] Pavlinov LV, Isadzhan YA, Smirnov VP. Phys. Met. Metallogr. (USSR) 1968;25:959
[42] Manayenkov VP, Lazarev VA, Kulemin AV, Golikov VM. Russ. Metall. 1977;2,99
[43] Kirkaldy JS, Smith PN, Sharma RC. Metall. Trans. 1973;4:624
[44] Ham JL. Trans. Am. Soc. Met. 1945;35:331
[45] Heijwegen CP, Rieck GD. Acta Metall. 1974;22:1269
[46] Hirano K, Cohen M. Trans. Jpn. Inst. Met. 1972;13:96
[47] Gruzin PL. Dokl Akad. Nauk SSSR 1954;94:681
[48] Sato K. Trans. Jpn. Inst. Met. 1964;5:91
[49] Romig AD, Goldstein JI. Metall. Trans. A 1981;12:243
[50] Treheux D, Guiralde P. Compt. Rend. Acad. Sci. 1973;277:1299
[51] Arita M, Ohyama M, Goto KS, Someno M. Z. Metallk. 1981;72:244
[52] Takemoto S, Nitta H, Iijima Y, Yamazaki Y. Phil. Mag. 2007;87:1619
[53] Nitta H, Yamamoto T, Kanno R, Takasawa K, Lida T, Yamazaki Y, Ogu S, Iijima Y. Acta

Mater. 2002;50:4117
[54] Iijima Y, Kimura K, Hirano K. Acta Met. 1988;36:2811
[55] Geise J, Herzig C. Z. Metallk. 1987;78:291
[56] Borg RJ, Birchenall CE. A.I.M.E. 1960;218:980
[57] Buffington FS, Hirano K, Cohen M. Acta Metall. 1961;9:434
[58] Hettich G, Mehrer H, Maier K. Scripta Metall. 1977;11:795
[59] Walter CM, Peterson NL. Phys. Rev. 1969;178:922
[60] Lübbehusen M, Mehrer H. Acta Metall. Mater. 1990;38:283
[61] Kucera J, Millien B, Ruzickova J, Foldyna V, Jakobova A. Acta Met. 1974;22:135
[62] Kieszniewski J. Pr. Inst. Hutn. 1967;19:253
[63] Kucera J, Million B, Ciha K. Koveve Mater. 1969;7:97
[64] Alberry PJ, Haworth CW. Met. Sci. 1974;8:407
[65] Borisov VT, Golikov VM, Sherbedinskiy GV. Phys. Met. Metall. 1966;22:175
[66] Nohara K, Hirano K. J. Jpn Inst. Met. 1976;40:1053
[67] Le Claire AD, In: Eyring H, editor. Physical Chemistry: An Advanced Treatise, vol. 10. Academic Press (New York), 1970. chap. 5.
[68] Ruch L, Sain DR, Yeh HL, Girafalco LA. J. Phys. Chem. Solids 1976;37:649
[69] Nitta H, Iijima Y. Phil. Mag. Lett. 2005;85:543
[70] Girifalco LA. J. Phys. Chem. Solids 1962;23:1171
[71] Vineyard GH. J. Phys. Chem. Sol. 1957;3:121
[72] Hänggi P, Talkner P, Borkovec M. Rev. Mod. Phys. 1990;62:251
[73] Potter HH. Proc. R. Soc. Long. A 1034;146:362
[74] Crangle J, Goodman GM. Proc. Roy. Soc. Lond. A 1971;321:477
[75] Philibert J. Atom Movements: Diffusion and Mass Transport in Solids, Les Éditions de Physique, 1991.
[76] Satta A, Willaime F, de Gironcoli S. Phys. Rev. B 1998;57:11184
[77] Satta A, Willaime F, de Gironcoli S. Phys. Rev. B 1999;60:7001
[78] Blöchl P. Phys. Rev. B 1994;50:17953
[79] Kresse G, Joubert D. Phys. Rev. B 1999;59:1758
[80] Perdew JP, Burke K, Ernzerhof M. Phys. Rev. Lett. 1996;77:3865
[81] Kresse G, Hafner J. Phys. Rev. B 1993;47:558

[82] Kresse G, Furthmüller J. Comput. Mat. Sci. 1996;6:15

[83] Kresse G, Furthmüller J. Phys. Rev. B 1996;54:11169

[84] Methfessel M, Paxton AT. Phys. Rev. B 1989;40:3616

[85] Chen Y, Fu CL, Ho KM, Harmon BN. Phys. Rev. B 1985;31:6775

[86] Wolverton C, Ozolins V, Asta M. Phys. Rev. B 2004;69:1440109

[87] Horton GK, Maradudin AA, editors. Dynamical properties of solids: phonon physics the cutting edge, North-Holland (New York), 1974

[88] Mendelev MI, Han S, Srolovitz DJ, Ackland GJ, Sun DJ, Asta M. Phil. Mag. 2003;83: 3977

[89] Mills G, Jonsson H, Schenter GK. Surf. Sci. 1995;324:305

[90] Jonsson H, Mills G, Jacobsen KW. In: Berne BJ, Ciccotti G, Coker DF, editors. Classical and Quantum Dynamics in Condensed Phase Simulations, World Scientific, 1998

[91] Fu CC, Torre JD, Willaime F, Bocquet JL, Barbu A. Nature Mater. 2005;4:68

[92] Söderlind P, Yang LH, Moriarty JA, Wills JM. Phys. Rev. B 2000;61:2579

[93] Fu CC, Willaime F, Ordejón P. Phys. Rev. Lett. 2004;92:175503

[94] Buschow KHJ, Cahn RW, Flemings MC, Ilschner B, Kramer EJ, Mahajan S, Veyssiere P, editors. Encyclopedia of Materials: Science and Technology, Elsevier (Amsterdam), 2001;2:1884-1890

[95] Nitta H, Miura K, Iijima Y. Acta Mater. 2006;54:283

[96] Bowen AW, Leak GM. Metall. Trans. 1970;1:1965

[97] Goldstein JI, Williams DB, Cliff G. In Principles of Analytical Electron Microscopy, Joy DC, Romig Jr AD, Goldstein JI, editors. Plenum Press, New York, 1986

[98] DTSA: Desk Top Spectrum Analyzer and X-ray Database, Standard Reference Data Program, National Institute of Standards and Technology, Gaithersburg, MD, 1997

[99] Cliff G, Lorimer GW. J. Microscopy 1975;103:203

[100] Goldstein JI, Newbury DE, Echlin P, Joy DC, Fiori C, Lifshin E. Scanning Electron Microscopy and X-ray Microanalysis, Plenum Press, New York, 1984

[101] Nockolds C, Nasir MJ, Cliff G, Lorimer GW. Proc. of the Inst. of Physics, Electron Microscopy and Analysis Group, Mulvey, T., Ed., Conf. Ser. No. 52, The Institute of Physics, London, 1979, p. 417

[102] Reed SJB. Electron Microprobe Analysis, Cambridge University Press, Cambridge, 1975

[103] Liu TF, Jeng SC, Wu CC. Metall Trans A 1992;23A:1395
[104] Marcon G, Peffen R, Lemaire H. IEEE Trans Magn. 1987;14:685
[105] Hao SM, Takayama T, Ishida K, Nishizawa T. Metall Trans A 1984;15A:1819
[106] Bradley AJ. J. Iron Steel Inst. 1951;168:233
[107] Leslie WC. Metall Trans A 1972;3:5
[108] Petch NJ. Acta Metall 1987;35:2027
[109] Herrmann J, Inden G, Sauthoff G. Acta Mater 2003;51:2847
[110] Pugh SF. Phil Mag. 1954;45:823
[111] Hahn KH, Vedula K. Scripta Metall. 1989;23:7
[112] Chang KM, Darolia R, Lipsitt HA. Acta Metall. Mater. 1992;40:2727
[113] Darolia R, Chang KM, Lipsitt HA. Intermetallics 1993;1:65
[114] Darolia R, Lahrman D, Field RD. Scripta Metall. Mater. 1992;26:1007
[115] Field RD, Lahrman DF, Darolia R. Acta Metall. Mater. 1991;39:2961
[116] Law CC, Blackburn MJ. AFWAL TR-87e4102. In: Rapidly solidified lightweight durable disk materials. Air Force Wright Aeronaut Lab; 1987
[117] Rachinger WA, Cottrell AH. Acta Metall. 1956;4:109
[118] Cotton JD, Noebe RD. Intermetallics 1993;1:117
[119] Grala EM. In: Westbrook JH, editor. Mechanical properties of intermetallic compounds. New York:Wiley; 1960. p. 358
[120] Stallybrass C, Sauthoff G. Materials Science and Engineering A 2004;387:985
[121] Jung I, Sauthoff G. Strength of Metals and Alloys: Proc. 7th Int. Conf. Strength of Metals and Alloys, McQueen, H.J. et al. (eds.), Pergamon Press, Montreal 1985, 7, 731
[122] Jung, I.; Sauthoff, G. Creep and Fracture of Engineering Materials and Structures: proceedings of the Third International Conference held at University College, Swansea, B. Wilshire, R.W. Evans (eds.), The institute of Metals, London 1987, 257
[123] Jung, I.; Sauthoff, G. Z. Metallk. 1989;80:484
[124] Standard test methods for flexural properties of unreinforced and reinforced plastics and electrical insulating materials. D790. In: Annual book of ASTM standards, vol. 08.01. ASTM; 2007
[125] Martin JW. In: Micromechanisms in particle-hardened alloys. Cambridge, UK: Cambridge University Press; 1980

[126] Patrick DK, Chang KM, Miracle DB, Lipsitt HA. In: Johnson L, Stiegler JO, Pope DP, editors. High temperature ordered intermetallic alloys IV, vol. 213., MRS Proc. 1991. p. 267

[127] Kovalev AI, Barskaya RA, Wainstein DL. Surf Sci. 2003;35-40:532

[128] Teng ZK, Liu CT, Miller MK, Ghosh G, Kenic E, Liaw PK. Room temperature ductility of NiAl-strengthened ferritic steels: effects of precipitate microstructure and hot rolling, in preparation

[129] Terada D, Yoshida F, Nakashima H, Abe H, Kadoya Y. ISIJ Int. 2002;42:1546

[130] Kadoya Y, Shimizu E. Tetsu To Hagane-J. Iron Steel Inst. Jpn. 1999;85:827

[131] Teng ZK, Zhang F, Miller MK, Huang S, Chou YT, Tien RH, Liu CT, Chang YA, Liaw PK. New ferritic steels with combined optimum creep resistance and ductility designed by coupling thermodynamic calculations with focused experiments, in preparation

[132] Kassner ME. Fundamentals of creep in metals and alloys. Elsevier; 2004

[133] Brown LM, Ham RK, in: Kelly A, and Nicholson RB (Eds.), Strengthening methods in crystals, Elsevier, Amsterdam, 1971, p. 75

[134] Martin JW, Micromechanisms in particle-hardened alloys, Cambridge University Press, Cambridge, U.K., 1980, p. 43

[135] Viswanathan R, Bakker W. J. Mater. Eng. Perform. 2001;10:96

G. BIBLIOGRAPHY

The following pages include the biographical information for P. K. Liaw (Principal Investigator), G. Ghosh, M. E. Fine, M. Asta, and C. T. Liu (Co-Principal Investigators).

PETER K. LIAW

Department of Materials Science and Engineering
The University of Tennessee, Knoxville, TN 37996-2200, USA
Phone: (865) 974-6356, Fax: (865) 974-4115, E-mail: pliaw@utk.edu

Education and Training

National Tsing Hua University, Taiwan, ROC	Physics	B.S., 1972
Northwestern University	Materials Science and Engineering	Ph.D., 1980

Research and Professional Experience

1993 - Present	Professor and Ivan Racheff Chair of Excellence, Department of Materials Science and Engineering, The University of Tennessee.
1980 - 1993	Senior and Fellow Engineers, Westinghouse Research and Development Center.
1974 - 1979	Research Assistant, Department of Materials Science and Engineering, Northwestern University.

Publications Closely Related To The Proposed Project

Editor or co-editor of 22 books and author or co-author of more than 450 papers.

[1] P. K. Liaw, S. I. Kwun, and M. E. Fine (1981), "Plastic Work of Fatigue Crack Propagation in Steels and Aluminum Alloys," Metallurgical Transactions, 12(1), pp. 49-55.

[2] P. K. Liaw and W. A. Logsdon (1988), "Fatigue Crack Growth Behavior in Inconel 706 at 297K and 4.2K," Acta Metallurgica, 36(7), pp. 1731-1744.

[3] P. K. Liaw, A. Saxena, and J. Schaefer (1989), "Estimating Remaining Life of Elevated-Temperature Steam Pipes, Part I: Materials Properties," Engineering Fracture Mechanics, 32, pp. 675-708.

[4] P. K. Liaw, A. Saxena, and J. Schaefer (1989), "Estimating Remaining Life of Elevated-Temperature Steam Pipes, Part II: Fracture Mechanics Analysis," Engineering Fracture Mechanics, 32, pp. 709-722.

[5] Y. D. Wang, H. Tian, A. D. Stoica, X. L. Wang, P. K. Liaw, and J. W. Richardson (2003), "Evidence on the Development of Large Grain-Orientation-Dependent Residual Stresses in a Cyclically-Deformed Alloy," Nature Materials, 2(2), pp. 101-106.

[6] C. Fan, H. Q. Li, L. J. Kecskes, K. X. Tao, H. Choo, P. K. Liaw, and C. T. Liu (2006), "Mechanical Behavior of Bulk Amorphous Alloys Reinforced by Ductile Particles at Cryogenic Temperatures," Physical Review Letters, 96(14), Article 145506, pp. 1-4.

[7] A. L. Ortiz, J. W. Tian, J. C. Villegas, L. L. Shaw, and P. K. Liaw (2008), "Interrogation of the Microstructure and Residual Stress of a Nickel-Base Alloy Subjected to Surface Severe Plastic Deformation," Acta Materialia, 56(3), pp. 413-426.

[8] S. Y. Huang, D. L. Worthington, M. Asta, V. Ozolins, G. Ghosh, and P. K. Liaw (2010), "Calculation of Impurity Diffusivities in α-Fe Using First-Principles Methods," Acta Materialia, 58(6), pp. 1982-1993.

[9] Z. K. Teng, M. K. Miller, G. Ghosh, C. T. Liu, S. Huang, K. F. Russell, M. E. Fine, and P. K. Liaw (2010), "Characterization of Nanoscale NiAl-Type Precipitates in a Ferritic Steel by Electron Microscopy and Atom Probe Tomography," Scripta Materialia, 63(1), pp. 61-64.

[10] Z. K. Teng, C. T. Liu, G. Ghosh, P. K. Liaw, and M. E. Fine (2010), "Effects of Al on the Microstructure and Ductility of NiAl-Strengthened Ferritic Steels at Room Temperature," Intermetallics, 18(8), pp. 1437-1443.

Synergistic Activities

- Member of American Society for Metals and The Minerals, Metals & Materials Society.
- Key Reader for Metallurgical and Materials Transactions.
- Reviewer of Acta Materialia, J. Materials Research, Materials Science and Engineering, Nature Materials, and Scripta Materialia.

Awards and Honors

2010	L. R. Hesler Award, The University of Tennessee.
2004 - Present	John Fisher Professorship, The University of Tennessee.
2004 - Present	National Alumni Association Distinguished Service Professor, The University of Tennessee.
2003	Engineering Research Fellow Award, The University of Tennessee.
2003 and 2008	Moses E. and Mayme Brooks Distinguished Professor Award, The University of Tennessee.
2002	Outstanding Teacher Award, The University of Tennessee.
1997	Fellow, ASM International.
1994 - 1996	Chairman of the Flow and Fracture Committee, American Society for Metals (ASM), and The Minerals, Metals, and Materials Society (TMS).
1993 - Present	Key Reader for Metallurgical and Materials Transactions.
1990 and 1992	Westinghouse Outstanding Performance Awards.

Collaborators and Other Affiliations

Collaborators

M. D. Asta - University of California, Berkeley; R. S. Benson, C. R. Brooks, R. A. Buchanan (Deceased), H. Choo, C. S. Feigerle, D. C. Joy, J. D. Landes, R. V. Leon, C. J. McHargue, G. M. Pharr, J. R. Ray, and B. R. Upadhyaya - University of Tennessee; T. M. Besmann, M. P. Brady, J. M. Corum, R. B. Dinwiddie, C. T. Liu, L. K. Mansur, M. K. Miller, D. P. Stinton, D. Stoica, P. F. Tortorelli, H. Wang, and X. L. Wang - Oak Ridge National Laboratory; O. Buck [Deceased] and D. K. Hsu - Iowa State University; K. Chan - Southwest Research Institute; M. Denda - Rutgers University; M. E. Fine and G. Ghosh - Northwestern University; G. Harlow and R. P. Wei - Lehigh University; J. Y. Huang and R. C. Kuo - Nuclear Energy Research Institute, Taiwan; D. L. Klarstrom and L. Pike - Haynes International, Inc.; R. Perez and K. K. Sankaran - Boeing Company; R. E. Shannon - Westinghouse; L. Shaw - University of Connecticut; and S. Yao - Carnegie Mellon University.

Graduate Advisor

Professor Morris E. Fine, Professor-Emeritus, Department of Materials Science and Engineering, Northwestern University.

Graduate Advisees

Z. An, B. R. Barnard, M. L. Benson, M. Borst, N. Chawla, A. Chuang, J. A. Cook, Q. Feng, M. W. Freels, E. Garlea, L. Garimella, B. A. Green, W. Guo, E. Huang, Lan Huang, Lu Huang, S. Huang, J. W. Jeon, H. Jia, F. Jiang, L. Jiang, J. Kim, F. Liu, L. Li, Y. Lu, R. L. McDaniels, W. M. Matlin, J. Miller, N. Miriyala, M. L. Morrison, J. A. Oberhaus, W. H. Peter, G. Porter, D. C. Qiao, J. Qiao, W. Ren, T. A. Saleh, S. Shanmugham, E. Shen, R. V. Steward, M. Stoica, J. Sun, K. Tao, C. B. Thomas, H. Tian, J. Tian, J. Wall, G. Wang, W. Wei, W. Woo, X. Xie, B. Yang, W. Yuan, T. Wilson, L. Wu, Y. Zhang, Z. Teng, W. Zhao, and J. Zhu.

Postdoctoral Advisees

L. Chen, C. Chiang, C. Fan, G. Fan, Y. He, J. Y. Huang, M. Huang, H. Ito, T. Lee, J. Yu, and C. Xu.

GAUTAM GHOSH

Department of Materials Science and Engineering
Northwestern University, Evanston, IL 60208-3108, USA
Phone: (847)467-2595, Fax: (847) 491-7820, Email: g-ghosh@northwestern.edu

Education and Training

University of Calcutta	Metallurgical Engineering	B.E., 1982
Indian Institute of Technology (IIT), New Delhi	Materials Science	Ph.D., 1986

Research and Professional Experience

1992 - Present	Research Assistant Professor, Department of Materials Science and Engineering, Northwestern University.
1989 - 1991	Research Associate I, Department of Materials Science and Engineering, Northwestern University.
1986 - 1988	Research Assistant, Department of Metallurgy and Materials Engineering, Katholieke University Leuven, Belgium.

Publications Closely Related To The Proposed Subject

[1] G. Ghosh and G. B. Olson (2002), "Precipitation of Paraequilibrium Cementite: Experiments, and Thermodynamic and Kinetic Modeling," Acta Materialia, 50, pp. 2099-2119.

[2] J. Jung, G. Ghosh, D. Isheim, and G. B. Olson (2003), "Precipitation of Heusler Phase (Ni_2TiAl) from B2-TiNi in Ni-Ti-Al and Ni-Ti-Al-X (X = Hf, Zr) Alloys," Metallurgical and Materials Transactions A, 34A, pp. 1221-1235.

[3] G. Ghosh and M. Asta (2005), "Phase Stability, Phase Transformations and Elastic Properties of Cu_6Sn_5: Ab Initio Calculations and Experimental Results," J. Materials Research, 20, pp. 3102-3117.

[4] J. Z. Liu, A. van de Walle, G. Ghosh, and M. Asta (2005), "Structure, Energetics and Mechanical Stability of Fe-Cu BCC Alloys from First-principles Calculations," Physical Review B, 72, Art. No. 144109.

[5] G. Ghosh and G. B. Olson (2007), "Integrated Design of Nb-based Superalloys: Ab Initio Calculations, Computational Thermodynamics and Kinetics, and Experimental Results," Acta Materialia, 55, pp. 3281-3303.

[6] J. Z. Liu, G. Ghosh, A. van de Walle, and M. Asta (2007), "Transferable Force-Constant Modeling of Vibrational Thermodynamic Properties in FCC-Based Al-TM (TM = Ti, Zr, Hf) Alloys," Physical Review B, Vol. 75, Art. No. 104117.

[7] G. Ghosh (2008), "Phase Stability and Cohesive Properties of Au-Sn Intermetallics: A First-Principles Study," Journal of Materials Research, 23(5), pp. 1398-1416.

[8] S. Y. Huang, D. L. Worthington, M. Asta, V. Ozolins, G. Ghosh, and P. K. Liaw (2010), "Calculation of Impurity Diffusivities in α-Fe Using First-Principles Methods," Acta Materialia, 58(6), pp. 1982-1993.

[9] Z. K. Teng, M. K. Miller, G. Ghosh, C. T. Liu, S. Huang, K. F. Russell, M. E. Fine, and P. K. Liaw (2010), "Characterization of Nanoscale NiAl-Type Precipitates in a Ferritic Steel by Electron Microscopy and Atom Probe Tomography," Scripta Materialia, 63(1), pp. 61-64.

[10] Z. K. Teng, C. T. Liu, G. Ghosh, P. K. Liaw, and M. E. Fine (2010), "Effects of Al on the Microstructure and Ductility of NiAl-Strengthened Ferritic Steels at Room Temperature," Intermetallics, 18(8), pp. 1437-1443.

Synergistic Activities

- Member of Materials Research Society, The Metallurgical Society.
- Reviewer of Acta Materialia, Intermetallics, J. Alloys and Compounds, J. Applied Physics, J. Electronic Materials, J. Materials Research, J. Materials Science, J. Physics: Condensed Matter, Metallurgical and Materials Transactions A, Microelectronic Reliability, Physica B, and Scripta Materialia.
- Reviewer of NSF Proposals.
- Co-Organizer of Three TMS Symposia on Microelectronic Packaging.

Awards And Honors

1996 - 1997 Visiting Scientist, National Research Institute for Metals, Tsukuba Laboratories, Japan.
1994 - 1997 Visiting Scientist, Max-Planck Institute for Metals Research, Powder Metallurgy Laboratory, Stuttgart, Germany.

Collaborators and Other Affiliations

Collaborators

M. D. Asta - University of California, Berkeley; G. Borzone and S. Delsante - University of Genova, Italy; M. E. Fine, Y. W. Chung, L. M. Keer, G. B. Olson, S. Vaynman, J. Wang, and C. Wolverton - Northwestern University; P. K. Liaw - University of Tennessee; C. T. Liu - Auburn University and Hong Kong Polytechnic University; and A. van de Walle - Caltech.

Graduate and Post Doctoral Advisor

Graduate Advisor: Prof. V. Raghavan, IIT-Delhi.
Postdoctoral Advisors: Prof. L. Delaey, Katholieke University Leuven, and Prof. G. B. Olson, Northwestern University.

MORRIS E. FINE

Department of Materials Science and Engineering
Northwestern University, Evanston, IL 60208-3108, USA
Phone: (847) 491-3537, Fax: (847) 491-7820, E-mail: m-fine412@northwestern.edu

Education and Training

University of Minnesota	Metallurgical Engineering	B.S., 1940
University of Minnesota	Physical Metallurgy	M.S., 1942
University of Minnesota	Physical Metallurgy	Ph.D., 1943

Research and Professional Experience

1954 - Present	Northwestern University, Various Positions including Chairman of First Materials Science and Engineering Department in the USA, Associate Dean of the Technological Institute, First Chairman of the Materials Research Center, Walter P. Murphy Technological Institute Professor, and Active and Emeritus Member of Graduate Faculty.
1984 -1994	Visiting Chair Professor, University of Texas, Austin.
1946 - 1954	Technical Staff, Bell Telephone Laboratory, Murray Hill, New Jersey.
1944 - 1945	Manhattan Project, University of Chicago and Los Alamos National Laboratory, New Mexico.

Publications Closely Related To The Proposed Subject

Author or co-author of more than 335 papers, 4 patents, and 1 book.

[1] H. L. Marcus, J. N. Peistrup, and M. E. Fine (1965), "Precipitation in 17-7 PH Stainless Steel," Transactions of the American Society of Metals, 58, pp. 176-181.

[2] H. A. Calderon, M. E. Fine, and J. R. Weertman (1988), "Coarsening and Morphology of β' Particles in Fe-Ni-Al-Mo Ferritic Alloys," Metallurgical Transactions A, 19, pp. 1135-1146.

[3] J. Miyake and M. E. Fine (1992), "Electrical Conductivity Versus Strength in a Precipitation Hardened Alloy," Acta Metallurgica et Materialia, 40, pp. 733-741.

[4] G. Ghosh, G. B. Olson, and M. E. Fine (1993), "Coherency Induced Morphological Instability in Ni-Al Type Precipitates," Proceedings, 51st Annual Meeting of Microscopy Society of America, Eds, G. W. Bailey and C. L. Rieder.

[5] G. Ghosh, C. J. Kuehmann, G. B. Olson, and M. E. Fine (1996), "Knowledge-Based Design of Ferritic Superalloys Strengthened by NiAl-Type B2 Precipitates," Proceedings of International Symposium on Computer Modelling and Simulation for Materials Design, NRIM, Tsukuba, Japan, January 31-February 2, 1996.

[6] M. E. Fine (1996), "Phase Transformations in Condensed Systems Revisited: Industrial Applications," Metallurgical and Materials Transactions A, 27, pp. 2397-2418, Institute of Metals Lecture, TMS Metal Gold Medal.

[7] M. S. Gagliano and M. E. Fine (2001), "Precipitation Kinetics of Niobium Carbide and Copper in a Low Carbon, Chromium-Free Steel," Calphad, 25(2), pp. 207-216.

[8] S. Vaynman, D. Isheim, R. P. Kolli, S. P. Bhat, D. N. Seidman, and M. E. Fine (2008), "High-Strength Low-Carbon Ferritic Steel Containing Cu-Fe-Ni-Al-Mn Precipitates," Metallurgical and Materials Transactions A - Physical Metallurgy and Materials Science, 39A(2), pp. 363-373.

[9] Z. K. Teng, M. K. Miller, G. Ghosh, C. T. Liu, S. Huang, K. F. Russell, M. E. Fine, and P. K. Liaw (2010), "Characterization of Nanoscale NiAl-Type Precipitates in a Ferritic Steel by Electron Microscopy and Atom Probe Tomography," Scripta Materialia, 63(1), pp. 61-64.

[10] Z. K. Teng, C. T. Liu, G. Ghosh, P. K. Liaw, and M. E. Fine (2010), "Effects of Al on the Microstructure and Ductility of NiAl-Strengthened Ferritic Steels at Room Temperature," Intermetallics, 18(8), pp. 1443-1437.

Synergistic Activities

- Member of National Academy of Engineering.
- Member of American Physical Society, American Society for Metals, The Minerals, Metals, and Materials Society (TMS), The American Ceramic Society (ACS), and American Association for the Advancement of Science.

Awards and Honors

2010 University of Minnesota Alumni Outstanding Achievement Award.
2003 AIME Honorary Member.
2003 American Academy of Arts and Sciences.
1996 TMS Institute of Metals/Mehl Lecture and Gold Medal.
1993 TMS Educator Award.
1992 Gilbert R. Speich Award [Iron and Steel Society of The American Institute of Mining, Metallurgical, and Petroleum Engineers (AIME)].
1990 Charles P. Barrett Award (Rocky Mountain Denver Chapter of ASM).
1990 Morris E. Fine Symposium Series (Sponsored by 3 TMS-ASM Committees) in Conjunction with TMS Fall Meeting, Detroit, Michigan.
1987 Honorary Member, Japan Institute of Metals.
1986 ASM Gold Medal.
1982 AIME James Douglas Gold Medal.
1981 AIME Mathewson Gold Medal.
1979 ASM Edward DeMille Campbell Memorial Lecturer.
1972 Member of National Academy of Engineering.
1970 Keynote Lecture, Electronics Division of The American Ceramic Society.
1961 Chicagoan of the Year in Science.

Collaborators and Other Affiliations

Collaborators

M. D. Asta - University of California, Berkeley; G. Ghosh Y. W. Chung, and S. Vaynman - Northwestern University; P. K. Liaw - University of Tennessee; and C. T. Liu - Auburn University and Hong Kong Polytechnic University.

Graduate Advisees

B. Fiedler and A. Zinck.

MARK D. ASTA

Department of Materials Science and Engineering
University of California, Berkeley, CA 94720, USA
Phone: (510) 643-9631, Fax: (510) 643-5792, Email: mdasta@berkeley.edu

Education and Training

University of California, Berkeley	Engineering Physics	B.S., 1988
University of California, Berkeley	Physics	M.A., 1990
University of California, Berkeley	Materials Physics	Ph.D., 1993
Sandia National Laboratories	Computational Materials Science	Postdoctoral Fellow, 1993-1995

Research and Professional Experience

2010 - Present	Materials Sciences Faculty Scientist, Lawrence Berkeley National Laboratory, Berkeley, CA
2010 - Present	Professor, Department of Materials Science and Engineering, University of California, Berkeley, CA.
2005 - 2010	Professor, Department of Chemical Engineering and Materials Science, University of California, Davis, CA.
2000 - 2005	Associate Professor, Materials Science and Engineering, Northwestern University, Evanston, IL.
1995 - 2000	Senior Member of Technical Staff, Sandia National Laboratories, Livermore, CA.

Publications Closely Related To The Proposed Subject

[1] A. van de Walle and M. Asta (2005), "First-Principles Modeling of Phase Equilibria," Handbook of Materials Modeling, Ed., S. Yip, Article 1.16, Springer, New York.

[2] W. Cao, J. Zhu, F. Zhang, W. A. Oates, M. Asta, and Y. A. Chang (2006), "Application of the Cluster/Site Approximation to the Calculation of Coherent Interphase Boundary Energetics," Acta Materialia, 54, pp. 377-383.

[3] E. A. Marquis, M. Asta, D. N. Seidman, and C. Woodward (2006), "Composition Evolution of Nanoscale Al_3Sc Precipitates in an Al-Mg-Sc Alloy," Acta Materialia, 54, pp. 119-130.

[4] G. Ghosh, S. Delsante, G. Borzone, M. Asta, and R. Ferro (2006), "Phase Stability and Cohesive Properties of Ti-Zn Intermetallics: First-Principles Calculations and Experimental Results," Acta Materialia, 54, pp. 4977-4997.

[5] G. Ghosh, S. Vaynman, M. Asta, and M. E. Fine (2007), "Stability and Elastic Properties of $L1_2$-$(Al,Cu)_3(Ti,Zr)$ Phases: Ab Initio Calculations and Experiments," Intermetallics, 15, pp. 44-54.

[6] M. E. Fine, J. Z. Liu, and M. D. Asta (2007), "An Unsolved Mystery: The Composition of BCC Cu Alloy Precipitates in BCC Fe and Steels," Materials Science and Engineering A, 463, pp. 271-274.

[7] G. Ghosh, A. van de Walle, and M. Asta (2007), "First-Principles Phase Stability Calculations of Pseudobinary Alloys of $(Al,Zn)_3Ti$ with $L1_2$, DO_{22} and DO_{23} Structures," J. Phase Equilibria and Diffusion, 28, pp. 9-22.

[8] J. Z. Liu, G. Ghosh, A. van de Walle, and M. Asta (2007), "Transferable Force-Constant Modeling of Vibrational Thermodynamic Properties in FCC-Based Al-TM (TM=Ti, Zr, Hf) Alloys," Physical Review B, 75, 104117.

[9] G. Ghosh, A. van de Walle, and M. Asta (2008), "First-Principles Calculations of Structural and Energetic Properties of BCC, FCC and HCP Solid Solutions in the Al-TM (TM=Ti,Zr,Hf) Systems: A Comparison of Cluster Expansion and Supercell Methods," Acta Materialia, 56, pp. 3202-3221.

[10] S. Huang, D. L. Worthington, M. Asta, V. Ozolins, G. Ghosh, and P. K. Liaw (2010), "Calculation of Impurity Diffusivities in α-Fe Using First-Principles Methods," Acta Materialia, 58, pp. 1982-1993.

Synergistic Activities

- Member of the National Resource Allocations Committee (NRAC) and the Partnership Resource Allocations Committee (PRAC) of the National Science Foundation's Partnership for Advanced Computational Infrastructure (PACI).
- Member of the "Physics and Chemistry of Materials" of the TMS; "Key Reader" Member of the Board of Review for Metallurgical and Materials Transactions.
- Member of Editorial Board for CALPHAD.
- Member of the Scientific Advisory Board, Max Planck Institute for Steel Research, Duesseldorf, Germany.
- Co-organizer of 16 International Workshops and Symposia on Topics in the Field of Computational Materials Science.

Awards and Honors

2004	Teacher of the Year, Department of Materials Science and Engineering, Northwestern University.
2002	ASM International's Materials Science Research Silver Medal.
2002	Lecturer at NATO-Advanced-Study-Institute on "Thermodynamics, Microstructure and Plasticity," held in Frejus, France

Collaborators and Other Affiliations

Collaborators

G. J. Ackland - University of Edinburgh; R. Benedek - Argonne National Laboratory; G. Ceder - Massachusetts Institute of Technology; Y. A. Chang - University of Wisconsin; R. W. Chantrell, T. Klemmer, and Oleg Mryasov - Seagate; D. E. Ellis, G. Ghosh, A. Karma, D. T. Keane, L. D. Marks, M. J. Miksis, G. B. Olson, K. R. Poeppelmeier, J. P. Qunitana, D. N. Seidman, Semyon Vaynman, P. W. Voorhees, and C. Wolverton - Northwestern University; N. Erdman - UOP; S. M. Foiles - Sandia National Laboratories; J. J. Hoyt - McMaster University; P. K. Liaw, C. T. Liu, and J. R. Morris - University of Tennessee; M. Manley and B. Sadigh - Lawrence Livermore National Laboratory; E. A. Marquis - Oxford; M. I. Mendelev - Ames National Laboratory; V. Ozolins - University of California, Los Angeles; D. J. Srolovitz - Yeshiva University; D. Y. Sun - East China Normal University, Shanghai, China; D. J. Thoma - Los Alamos National Laboratory; Katsuyo Thornton - University of Michigan; Dallas Trinkle - University of Illinois, Urbana-Champaign; O. Warschkow - University of Sydney; E. B. Webb - Sandia National Laboratories; and C. Woodward - Air Force Research Laboratory.

Graduate and Post Doctoral Advisors

Graduate Advisor: Prof. Didier de Fontaine, University of California, Berkeley.
Postdoctoral Advisor: Dr. S. M. Foiles, Sandia National Laboratories, Livermore, CA.

Graduate Advisees

M. Beck, C. Becker, B. Hanken, S. Jindal, B. Krack, Z. Liu, H. Ramalingam, K. Ray, K. Witkowski, and B. Yang.

Postdoctoral Advisees

V. Alexandrov, D. Buta, T. Haxhimali, C. M. Retford, B. Sadigh, D. Y. Sun, A. van de Walle, and B. Yang.

CHAIN T. LIU

Department of Materials Science and Engineering
The University of Tennessee, Knoxville, TN 37996-2200, USA
Phone: (865) 974-5567, Fax: (865) 974-4115, E-mail: liuct@ornl.gov

Education and Training

National Taiwan University, Taipei, Taiwan	Mechanical Engineering	B.S., 1960
Brown University	Materials Science and Engineering	M.S., 1964
Brown University	Materials Science and Engineering	Ph.D., 1967

Research and Professional Experience

2009 - Present	Professor, Hong Kong Polytechnic University
2009 - Present	Professor, Auburn University
2005 - 2009	Distinguished Research Professor, The University of Tennessee.
1985 - 2009	Corporate Fellow (named Senior Corporate Fellow in 1997), Oak Ridge National Laboratory.
1983 - 2005	Group Leader, Alloying Behavior and Design Group, Metals and Ceramics Division, Oak Ridge National Laboratory.
1967 - 1982	Staff Member, Alloying Behavior and Design Group, Metals and Ceramics Division, Oak Ridge National Laboratory.

Publication Closely Related To The Proposed Project

Editor or co-editor of 20 books and author or co-author of more than 350 papers.

[1] C. T. Liu, C. L. White, and J. A. Horton (1985), "Effect of Boron on Grain Boundaries in Ni_3Al," Acta Metallurgica, 33(2), pp. 213-229.

[2] C. T. Liu, J. H. Zhu, M. B. Brady, C. G. Mckamey, and L. M. Pike (2000), "Physical Metallurgy and Mechanical Properties of Transition-metal Laves Phase Alloys," Intermetallics, 8, pp. 1119-1129.

[3] Z. P. Lu, C. T. Liu, C. H. Kam, and Y. Li (2003), "Direct Observation of a Concealed Glass Transition in a Mg-Ni-Nd Metallic Glasses," Applied Physics Letters, 82, pp. 862-864.

[4] J. H. Zhu, C. T. Liu, and C. H. Chen (2004), "Effect of Iron Additions on Environmental Embrittlement," Intermetallics, 12, pp. 859-868.

[5] B. Yang, P. K. Liaw, G. Wang, M. Morrison, C. T. Liu, R. A. Buchanan, and Y. Yokoyama (2004), "In-situ Thermographic Observation of Mechanical Damage in Bulk-Metallic Glasses During Fatigue and Tensile Experiments," Intermetallics, 12, pp. 1265-1274.

[6] B. Yang, M. L. Morrison, P. K. Liaw, R. A. Buchanan, G. Y. Wang, C. T. Liu, and M. Denda (2005), "Dynamic Evolution of Nanoscale Shear Bands in a Bulk-Metallic Glass," Applied Physics Letters, 86(14), Article 141904, pp. 1-3.

[7] Y. Yamamoto, M. P. Brady, Z. P. Lu, P. J. Maziasz, C. T. Liu, B. A. Pint, K. L. More, H. M. Meyer, and E. A. Payzant (2007), "Creep-Resistant, Al_2O_3-Forming Austenitic Stainless Steels," Science 316(5823), pp. 433-436.

[8] Y. He, Y. Jiang, N. P. Xu, J. Zou, B. Y. Huang, C. T. Liu, and P. K. Liaw (2007), "Fabrication of Ti-Al Micro/Nanometer-Sized Porous Alloys through the Kirkendall Effect," Advanced Materials, 19(16), pp. 2102-2106.

[9] Z. K. Teng, M. K. Miller, G. Ghosh, C. T. Liu, S. Huang, K. F. Russell, M. E. Fine, and P. K. Liaw (2010), "Characterization of Nanoscale NiAl-Type Precipitates in a Ferritic Steel by Electron Microscopy and Atom Probe Tomography," Scripta Materialia, 63(1), pp. 61-64.

[10] Z. K. Teng, C. T. Liu, G. Ghosh, P. K. Liaw, and M. E. Fine (2010), "Effects of Al on the Microstructure and Ductility of NiAl-Strengthened Ferritic Steels at Room Temperature," Intermetallics, 18(8), pp. 1437-1443.

Synergistic Activities

- Member of National Academy of Engineering.
- Member of The Metallurgical Society, American Society for Metals, and the International Precious Metals Institute.
- Editor of Journal of Intermetallics, Materials Letters, and Journal of Materials Research.

Awards and Honors

2004 Elected as a Member of the National Academy of Engineering.
2003 Identified as a Highly Cited Researcher in Materials Science by ISI.
2001 Acta Metallurgica Gold Medal, "for His Leadership and Outstanding Achievements in Science and Technology of Ordered Intermetallic Alloys". Listed among the Accomplishments by DOE in "The Energy 100". Identified as an Author in the List of 1,000 Most Cited Physicists by ISI.
1994 Fellow, TMS.
1993 Associate Editor, Materials Letters.
1992 Golden Acorn Award, The Inventor's Forum of MMES (3 Awarded over Career).
1988 E. O. Lawrence Award (Established by the U.S. President), U.S. Department of Energy.
1984 Fellow, American Society for Metals.

Collaborators and Other Affiliations

Collaborators

M. D. Asta - University of California, Berkeley; Mustafa Bakkai - North Carolina State University; C. J. Brooks, P. K. Liaw, R. A. Buchanan, T. G. Nieh, and W. H. Peter - University of Tennessee; Y. A. Chang - University of Wisconsin-Madison; Y. T. Chou - University of California, Irvine; G. Ghosh and M. E. Fine - Northwestern University; D. R. Johnson - Purdue University; K. S. Kumar - Brown University; D. J. Larson - Seagate Company; Z. P. Lu, E. P. George, J. H. Schneibel, and C. L. Fu - Oak Ridge National Laboratory; C. J. McMahon - University of Pennsylvania; L. M. Pike - Haynes International; N. S. Stoloff - Rensselaer Polytechnic Institute; R. H. Zee - Auburn University; and J. H. Zhu - Tennessee Technological University.

Graduate Advisors

Professor J. Gurland, Brown University.

Postdoctoral Advisees

Z. P. Lu and B. Yang.